



POLITECNICO DI MILANO

Scuola di Ingegneria Industriale e dell'Informazione  
Corso di Laurea Magistrale in Ingegneria Fisica

**Temperature measurements at megabar pressures:  
direct comparison between reflective and refractive  
optics for the laser heated diamond anvil cell**

Relatore: Prof. Giacomo Claudio GHIRINGHELLI  
Correlatori: Dr. Olivier MATHON  
Dr. Raffaella TORCHIO

Tesi di Laurea di:  
Ruggero Giampaoli  
Matricola: 816900

Anno Accademico 2015/2016



# Contents

<b>Acknowledgements</b>	<b>II</b>
<b>Abstract</b>	<b>III</b>
<b>Sommario</b>	<b>IV</b>
<b>1 Introduction</b>	<b>2</b>
1.1 Motivation: melting curve discrepancies . . . . .	2
1.2 The laser heated diamond anvil cell . . . . .	4
1.3 Temperature measurements in the LHDAC . . . . .	8
1.3.1 Introduction to Pyrometry . . . . .	8
1.3.2 Two-Colour Sliding Pyrometry . . . . .	14
1.3.3 Thermal radiation collecting optics in the LHDAC: critical points . . . . .	16
1.3.4 Schwarzschild and achromatic doublets . . . . .	21
1.4 Laser heating setups at ESRF . . . . .	23
1.4.1 ID24 setup . . . . .	23
1.4.2 ID27 setup . . . . .	25
<b>2 Experimental setup</b>	<b>27</b>
2.1 General description . . . . .	27
2.2 Measurements . . . . .	29
2.2.1 Calibration and fitting . . . . .	29
2.2.2 Uncertainty analysis and temperature stability . . . . .	30
2.2.3 Measurement procedure . . . . .	33
2.2.4 Resolution measurements . . . . .	34
<b>3 Results and discussion</b>	<b>36</b>
3.1 Theoretical results . . . . .	36
3.2 Experimental results . . . . .	43
3.2.1 Preliminary results . . . . .	43
3.2.2 Fit analysis and discussion . . . . .	46
<b>4 A real experiment on a X-ray beamline</b>	<b>56</b>
<b>5 Conclusions</b>	<b>60</b>
<b>List of Figures</b>	<b>62</b>

# Acknowledgments

Firstly, I would like to thank my supervisor, Professor Giacomo Claudio Ghiringhelli, and Dr. Sakura Pascarelli for welcoming me to the ESRF and introducing me to the world of synchrotron.

My thanks also to my advisors, Dr. Raffaella Torchio and Dr. Olivier Mathon, for encouraging and supporting me throughout the whole period I have been at ESRF. Your guidance has been invaluable.

I would like to express my gratitude to Dr. Innokenty Kantor, Dr. Mohamed Mezouar and Dr. Gaston Garbarino for their help and their patience: whenever I deal with lenses or Schwarzschilds I will think of your lessons. My gratitude also to Dr. Angelika Rosa for her encouragement and assistance when working under high pressure conditions.

Un ringraziamento particolare a Silvia, per la sua presenza costante e per il suo entusiasmo, per il suo prezioso e immancabile aiuto, per aver reso lieti anche i momenti difficili al sincrotrone. Ringrazio inoltre i miei compagni di ufficio, Manuel e Richard, che mi hanno saputo accogliere e consigliare, e tutti quanti nella beamline, per la loro disponibilità e supporto: la semplicità e l'armonia del gruppo hanno reso gradevoli le lunghe giornate trascorse al lavoro.

La mia gratitudine va anche a coloro che, in momenti diversi, mi hanno accompagnato lungo il cammino:

Ai miei genitori, per la premura, il tempo e la tolleranza con le quali mi hanno cresciuto.

Al nonno Romolo, per l'affetto e la pazienza.

A chi mi è vicino tra l'Appennino e l'Adriatico: qui ho trovato una seconda casa, un'accoglienza gioiosa, un luogo dove fare piacevolmente ritorno.

Ai Maestri, che mi hanno reso un po' più libero.

Agli Amici, che hanno saputo rendermi un po' più felice.

A coloro con cui ho sognato e condiviso progetti e con i quali ho imparato a vivere il presente.

A chi mi ha teso una mano quando ne avevo bisogno.

A chi ha portato colori e un sorriso nelle livide giornate milanesi.

A quanti mi hanno spinto a riflettere, a non sedermi, a non poltrire; a chi ha saputo regalarmi preziosi momenti di confronto.

A chi ha atteso che capissi, senza forzare, senza pretendere. A chi ha cercato di capirmi.

Grazie.

# Abstract

During last decades, lots of efforts have been done to improve experimental setups aimed at studying matter at very high temperatures and pressures. Such a commitment has been most of all motivated by a growing interest in geophysical research and in possible applications in material science. Progresses in experimental methods and the increasing appeal of the topic have led many scientists to investigate different physical properties of materials at extreme conditions: phase transitions, magnetism, electronic structure and many more.

The only static technique that allows to reach very high pressures (up to 300 GPa) and temperatures (thousands of Kelvin) is the laser-heated diamond anvil cell (LHDAC): the sample is squeezed in between two diamonds to achieve the needed pressure and heated with powerful lasers ( $\approx 100$  W). Samples loaded in these kinds of cells are very small ( $< 1000 \mu\text{m}^2 \times 5 \mu\text{m}$ ) and, therefore, performing in situ measurements is very challenging: great care should be paid in sample preparation and the experimental apparatus should guarantee stable and reproducible measurements. So far, results of different experiments do not always coincide. This is the case, for example, of melting temperatures: hundreds of K deviations have been found in different investigations of the same materials. Many melting studies are carried out in synchrotrons, where a high brilliance x-ray beam can be used to probe the sample and detecting the melting (XRD, XAS). In particular, at the European Synchrotron Radiation Facility (ESRF) two different beamlines, ID24 and ID27 have obtained quite different results in studying phase transitions. Several reasons may lie behind these discrepancies: chemical contaminations of the sample, possible misalignments between laser and X-rays, differences in melting criteria, inaccuracies in temperature measurements. In particular, high-temperature metrology has often been the object of long-standing controversies and this has been the subject of this thesis. In the LHDAC, temperature is measured spectroradiometrically by fitting the thermal radiation with Planck's law using the grey body approximation. Since LHDAC temperature is not uniform and it could vary of about hundreds of degrees in few  $\mu\text{m}$ , the accuracy in this kind of measurement is ultimately limited by the resolution of the optics used to collect this radiation. The optics of the two beamlines are different: ID27 adopts reflective optics based on Schwarzschild objectives, while on ID24 temperature is detected using an infinity objective with two achromatic doublets. Both optics are used in many laboratories around the world which use laser heated diamond anvil cell to reach high temperatures and high pressures.

The aim of this work has been to directly investigate the effect of optics isolating them from the other possible sources of inaccuracy in melting temperature measurements. To do so, an ad hoc experimental setup has been assembled using the beamline objectives. Many laser heating test on real W samples loaded in diamond anvil cell have been performed obtaining systematic temperature differences up to 200 K at temperature above 2500 K.

The obtained spectra have been analysed using the two-colour technique and compared with the ones taken on the beamline. Furthermore, to understand the influence of optics resolution in temperature measurements, theoretical simulations have been carried out considering different point spread functions.

# Sommario

Negli ultimi decenni, motivate da interessi nel campo della geofisica e della scienza dei materiali, sono state sviluppate nuove tecnologie e tecniche nell'ambito dello studio di materiali ad alte pressioni e ad alte temperature. In particolare, la tecnica LHDAC (laser heated diamond anvil cell) è l'unica tecnica statica che permetta di raggiungere pressioni elevate ( $\approx 300$  GPa) e alte temperature (migliaia di Kelvin). L'utilizzo di questa tecnica per le alte pressioni sfrutta l'elevata durezza e l'elevato modulo di compressibilità del diamante. Il campione viene collocato in una cella composta da due sezioni in ognuna delle quali è incastonato un diamante; la cella è realizzata in modo tale che, una volta chiusa, i diamanti presentino due facce piane tra loro parallele. Il campione viene dunque posizionato tra le due gemme e una guarnizione (gasket) impedisce che questo possa muoversi liberamente. Quando la cella è posta in pressione, i diamanti si avvicinano e il gasket e il campione vengono compressi e deformati. Un fascio laser ad elevata potenza (circa 100 W), in una banda spettrale nella quale il diamante è trasparente, permette di raggiungere temperature elevate.

Una delle applicazioni più rilevanti dell'utilizzo di LHDAC in ambito geofisico è lo studio delle transizioni di fase, in particolare delle curve di fusione di quei materiali (come Fe e Ni) che si suppongono costituire il nucleo terrestre. Le curve di fusione rappresentano la transizione solido-liquido in un diagramma di fase pressione-temperatura. La luce di sincrotrone si è rivelata un valido strumento per determinare queste transizioni di fase; in particolare, all'European Synchrotron Radiation Facility (ESRF) sono stati condotti diversi esperimenti in due beamline: ID24 (XAS) e ID27 (XRD). In alcuni casi sono state trovate discrepanze tra le curve di fusione ottenute in queste beamline (e in diversi altri laboratori): le temperature osservate differiscono anche di centinaia di Kelvin e un consenso unanime sul reale comportamento di questi materiali a pressioni e temperature estreme non è ancora stato raggiunto. Una possibile spiegazione di queste discrepanze risiede nell'accuratezza delle misure di temperatura. Nelle LHDAC questa viene misurata con tecniche pirometriche, ossia analizzando l'emissione di corpo nero del campione. La radiazione termica viene focalizzata, tramite un sistema ottico, all'ingresso di uno spettrometro che permette di decomporre la radiazione nelle sue componenti spettrali. Lo spettro così acquisito viene successivamente fittato con la legge di Planck in approssimazione di corpo grigio: la temperatura è ottenuta direttamente da uno dei due parametri del fit (il secondo è l'emittanza del campione). A causa della ridotta dimensione del campione ( $< 1000 \mu\text{m}^2 \times 5 \mu\text{m}$ ), del suo non perfetto isolamento termico e della non uniformità del profilo spaziale del fascio laser, il campione è caratterizzato da un profilo di temperatura non uniforme (la temperatura può variare di centinaia di gradi in pochi  $\mu\text{m}$ ). Poiché i sistemi ottici hanno una risoluzione limitata (in genere dell'ordine di qualche  $\mu\text{m}$ ), il segnale in ingresso allo spettrometro sarà costituito da contributi spettrali relativi ad aree del campione con temperature differenti, introducendo pertanto errori sistematici nella misura di temperatura.

Lo scopo di questa tesi è quello di comparare due diverse tipologie di ottiche utilizzate nelle tecniche di pirometria applicate alle diamond anvil cell: una basata sull'utilizzo di elementi rifrattivi e l'altra sull'utilizzo di specchi. A ESRF sono presenti entrambe queste tipologie: ID27 utilizza un microscopio costituito da specchi sferici assemblato in una configurazione di tipo Schwarzschild mentre ID24 utilizza un obiettivo composto da una coppia di doppietti acromatici.

Il principale problema delle ottiche rifrattive è rappresentato dalle aberrazioni cromatiche: sebbene queste vengano parzialmente corrette tramite l'utilizzo di lenti "acromatiche", non possono essere totalmente soppresses. Nelle ottiche utilizzate nella beamline ID24, gli effetti di questo tipo di aberrazioni sono ulteriormente attenuati tramite l'utilizzo di una pupilla (iris) che, posta all'ingresso dell'obiettivo,

riduce l'apertura numerica delle lenti.

Le ottiche basate sugli specchi sono invece acromatiche per costruzione, ma presentano generalmente maggiori aberrazioni monocromatiche. Eventuali errori nell'accuratezza delle misure di temperatura possono, in questo caso, derivare dalla limitata risoluzione del sistema ottico. Durante questa esperienza di tesi è stato realizzato un apposito setup nel quale è possibile confrontare direttamente l'effetto prodotto dalle due tipologie di ottiche sulle misure di temperatura e, quindi, sulle curve di fusione. Gli obiettivi impiegati in questo setup sono quelli delle due beamline: il microscopio Schwarzschild di ID27 e i doppietti acromatici di ID24; le misure di temperatura sono state effettuate muovendo le ottiche in rapida successione grazie all'ausilio di attuatori pneumatici.

Il primo risultato ottenuto conferma la necessità dell'utilizzo degli iris nelle misure di temperatura; senza questi, infatti, la temperatura misurata è soggetta a forti errori sistematici. È stato invece trovato un buon accordo, sino a temperature prossime a 2500 K, tra le misure in temperatura effettuate con gli specchi Schwarzschild e con le lenti con una apertura numerica ridotta. Sopra 2600 K si osservano differenze sistematiche fino a 200 K. Gli spettri ottenuti sono stati esaminati effettuando una analisi dei "two-colour plot". Questa tecnica è basata sulla linearizzazione dell'equazione di Planck (approssimazione di Wien) e permette di studiare eventuali deviazioni dall'emissione di corpo nero in funzione della lunghezza d'onda. Sono state osservate distorsioni negli spettri ottenuti con entrambe le ottiche. Gli spettri acquisiti con le lenti sono stati confrontati con quelli ottenuti in un reale esperimento su ID24 allo scopo di determinare il range ottimale sul quale effettuare i fit.

Al fine di raggiungere una maggiore comprensione degli effetti delle ottiche sulle misure di temperatura, sono state effettuate diverse simulazioni utilizzando il software di calcolo Matlab. Alcune di queste simulazioni mostrano come, anche per un sistema ideale limitato dalla sola diffrazione, si possano osservare degli errori sistematici nell'acquisizione delle temperature dell'ordine di 100 K.

Questo elaborato è stato organizzato in cinque capitoli ai quali si accenna brevemente nel seguito. Nel primo capitolo vengono inizialmente presentate le motivazioni alla base di questo progetto di ricerca. Successivamente, vengono descritte le diamond anvill cell e la tecnica di laser heating. Grande spazio è dedicato alla pirometria, con particolare attenzione al ruolo dei diversi sistemi ottici nelle misure di temperatura nelle LHDAC. Infine, un'ultima sezione riporta la descrizione dei setup di laser heating di ID27 e di ID24.

La prima parte del secondo capitolo è riservata alla descrizione del setup sperimentale usato e del rumore presente nell'acquisizione degli spettri. In seguito viene introdotta la modalità con la quale sono state eseguite le misure di temperatura in relazione alla stabilità temporale della temperatura del campione.

Nel capitolo "experimental results and discussion" sono dapprima descritti i risultati teorici e sperimentali ottenuti. Una seconda sezione discute questi risultati e li rapporta alle curve di fusione del Fe ottenute sulle beamline ID27 e ID24.

Il quarto capitolo riguarda le misure di temperatura ottenute in un vero esperimento sulla beamline ID24 nel quale è stata indagata la curva di fusione del Ni. Gli spettri ottenuti sono confrontati con quelli acquisiti in laboratorio tramite i "two-colour plot". Infine, nell'ultimo capitolo, vengono riepilogati i principali risultati ottenuti e le conclusioni che ne sono state tratte.

*Je ne connais point d'autre vérité. Je ne  
connais que de structures qui plus ou moins  
me sont commodes pour dire le monde.*

ANTOINE DE SAINT-EXUPÉRY

# Chapter 1

## Introduction

### 1.1 Motivation: melting curve discrepancies

The work that I have carried out during my thesis experience at ESRF concerns temperature measurements in experimental setups that aim reaching extreme conditions of pressure and temperature. Scientific motivations at the origin of this work are presented in this section.

During last decades, a lot of effort has been devoted to investigate melting phenomena and in particular melting curves of metals using different techniques. A melting curve is the curve laid on the pressure-temperature plane that represents the boundary between solid and liquid states of matter. Despite many experiments at high temperature and pressure have been accomplished, long-standing controversies are still found in some cases, like in tantalum Figure 1.1.

Measuring melting curves at extreme conditions requires the capability to reach high pressure and high temperature, necessary for the melting, and, consequently, to properly measure these conditions. Furthermore, the sample should be chemically stable during heating processes and a reliable melting criterion, to distinguish the occurrence of the molten phase, is required. These requirements are not always all fulfilled at the same time, resulting in large errors; the way temperature measurements are performed, for example, is considered to be responsible for differences of about hundreds of Kelvin in melting curve temperatures [1].

Different methods and techniques have been used to detect the melting in metals under high pressure. Over the last decade the development of laser heating coupled to diamond anvil cell (DAC) experiments at large-scale facilities has lead to a substantial advance in the field of melting phenomena. In particular synchrotron x-ray diffraction (XRD) and x-ray absorption (XAS) have been used to detect the melting of metals in the laser heated (LH) DAC [2] [3] [4] [5] [6] [7].

However recently an important discrepancy in the melting curve of Fe was found between curves measured by XRD [8] and XAS [3] (Figure 1.2) at beamline ID27 [9] and ID24 [10] respectively at the European Synchrotron Radiation Facility (ESRF). Fe is believed to be the most abundant element of the Earth's core ([11] [12] [13]) and its high-pressure and temperature behaviour could be of great interest in determining the temperature profile in the Earth's interior. So far, the density of the inner (solid) and outer (liquid) core could be determined by seismological observations, and so are the pressures [2], however temperature profiles remains uncertain. Therefore the knowledge of the melting curve of the most abundant material in the Earth's core, as well as of other minor components (Ni and Co), would constrain the temperature at least at the border between the Inner (solid) and Outer (liquid) core (ICB: Inner Core Boundary at 330 GPa).

The possible origins of the discrepancy found in the Fe curve are multiple, ranging from sample effects (i.e. chemical reactions) to systematic errors in the temperature determination. This second aspect deserves an accurate investigation - which is the main aim of this Thesis - especially because the optical systems for temperature determination used at beamlines ID27 and ID24 are different.

The optical systems used on ID27 is based on mirrors, in a configuration called "Schwarzschild", whereas the optics on ID24 is based on lenses. These two kinds of optics are used not only at ESRF,

but also at extreme conditions laboratories all over the world to perform spectroradiometric temperature measurements. The accuracy of the two optical systems is still object of debate [14].

The goal of this work is then to directly measure any possible temperature difference given by the reflective and refractive optical systems. Also, some simulations and spectra analysis have been performed to give better significance to the results obtained.

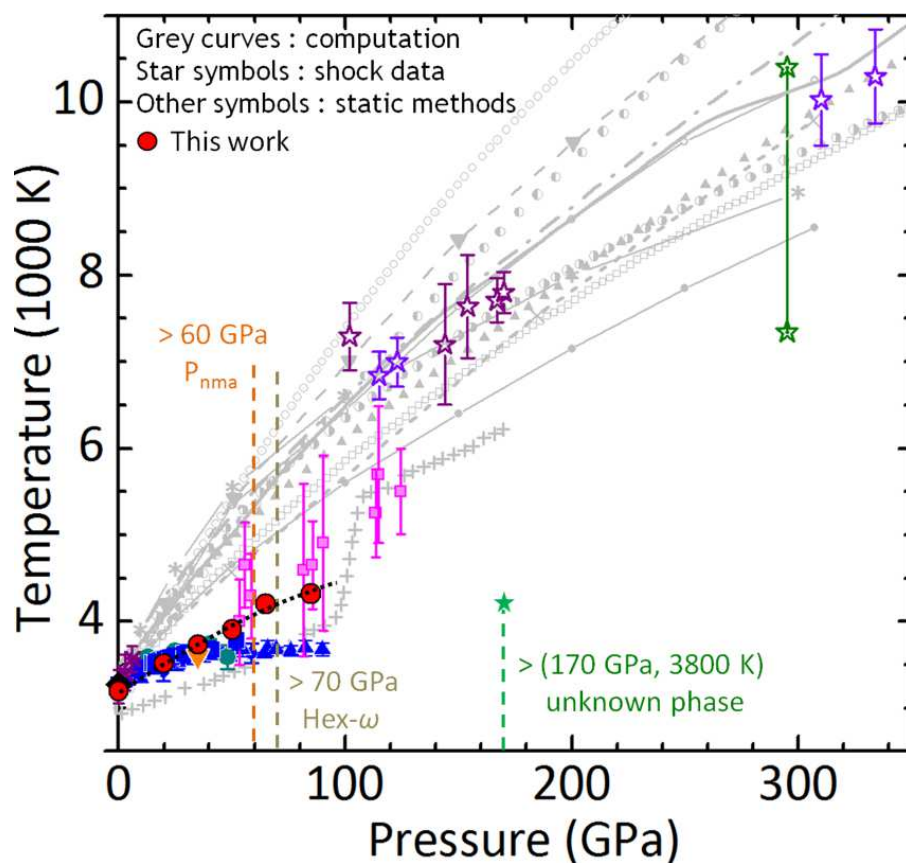


Figure 1.1: Tantalum melting curves from theoretical simulations, static and laser shock data [15]. The great amount of different melting curves published on different papers shows that an unanimous consensus about melting temperatures at high pressure is still lacking.

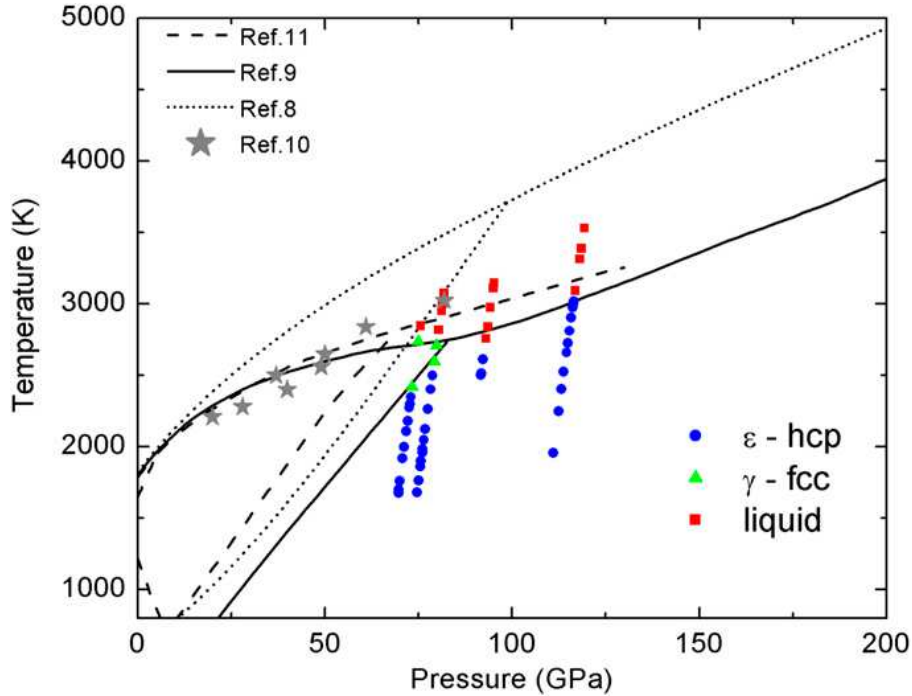


Figure 1.2: Iron melting curves [3]. Circles represent temperature runs performed on the XAS beamline ID24 using refractive optics. Blue circles refer to solid hcp iron; ; green ones correspond to the solid fcc phase and red ones to the liquid. Dotted line is the phase transition curve proposed by Anzellini et al. [2], measuring temperature with Schwarzschild mirrors and using x-rays diffraction melting criterion (the melting is detected by the appearance of diffusion halo when sample is in a disordered liquid state). The temperature difference between the two curves is larger than 500 K.

## 1.2 The laser heated diamond anvil cell

To reach the extreme pressures and temperatures required, for example, to study the physical and chemical properties of the earth's core, several techniques have been developed. These methods span different temperature and pressure ranges and can sometimes be used in a complementary way depending on the specific material property studied; Figure 1.3 illustrates the different ranges reachable by some methods: static compression in the DAC coupled to resistive heating or laser heating, and dynamic compression. Dynamic techniques, like shock compression, can reach a wider range of conditions, but they are limited by the short propagation time scale [16]. Static techniques allow to reach extreme conditions for longer times but they span smaller range and, in some cases, they require small samples. This is the case of the high pressure technique based on diamond anvil cells: in this technique, the sample is pressurized between diamonds and has dimensions  $\leq 1000 \mu\text{m}^2 \times 5 \mu\text{m}$ . This technique is the one which is used both on ID24 and ID27 coupled with a laser heating system to reach high temperatures; this section is dedicated to illustrate in detail how experiments are performed with laser heating diamond anvil cells.

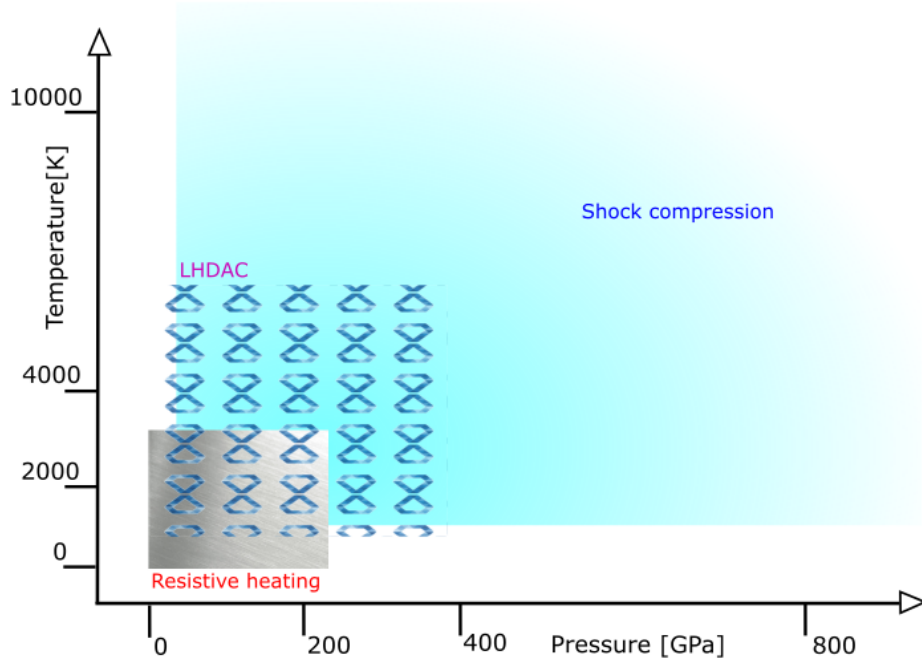


Figure 1.3: P-T domain reachable with three different techniques: resistive heating (grey), laser heating diamond anvil cell (diamond patterned) and shock compression (dynamic technique) [8] [17] [18] [19].

The LHDAC is an ideal tool to couple high  $P$  ( $\approx 300$  GPa) and  $T$  (up to 6000 K) to synchrotron techniques because, apart from being the strongest materials, diamonds are transparent for all the frequencies in the visible spectrum, in the near infrared and the hard x-ray range.

A diamond anvil cell (DAC) is composed essentially of two diamond anvils having flat faces at the head (large face) and at the bottom (small face, or culet) [20] [21]. The two diamonds are fixed in a holder (the cell) that can be opened to load the sample and squeeze it between the two anvil heads. The size of these diamond anvils, as well as sample dimensions, varies depending on the target pressure. In Figure 1.4 a picture of a Letoullec DAC is shown [22]. High pressure can be reached by exerting a force onto the large faces of diamonds; the pressure obtained at the diamond culet is then  $P \approx F/A$ . The force can be applied in different ways. We have used a membrane DAC in which pressure is transmitted in a hydraulic way by means of a gas progressively filling the membrane. This technique allows to reach adequate homogeneous conditions and a precise and remote control of the pressure exerted onto the cell [22]. This is carried out by using a pressure driver controlling the gas filling in the membrane.

Considering the extreme conditions that both diamonds and the sample undergo, it is straightforward that a careful alignment of the diamonds is essential to preserve the integrity of the system. A very tiny misalignment of the anvils could, in fact, generate high pressure gradients inside the cell and could damage diamonds and cell.

When loaded in the cell, the sample is not directly in contact with diamonds, but is surrounded by a pressure medium, which contributes to reach more hydrostatic conditions [see Figure 1.6]. Both the pressure medium and the sample are encapsulated within a metallic gasket that should be hard enough to tolerate high pressures. The typical gasket material used for  $P > 30$  GPa is rhenium. The gasket is pre-indented squeezing it between the two diamonds and, thereafter, a circular hole is cut with a Q-switching laser at the very centre of the indentation to create a sample chamber for the sample and the pressure medium. Gasket indented thickness is about 35  $\mu\text{m}$  for a culet of 300  $\mu\text{m}$  and the sample thickness was typically 4  $\mu\text{m}$  in our experiments.

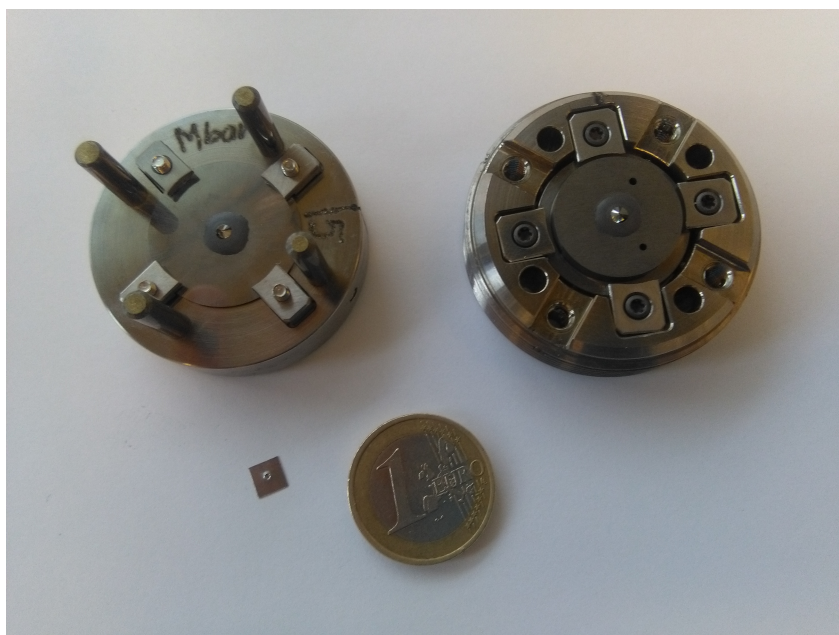


Figure 1.4: Example of a Letoullec DAC. the diamonds are in the proper centre of the cell holders and are carefully aligned to show parallel surfaces when the cell is closed.

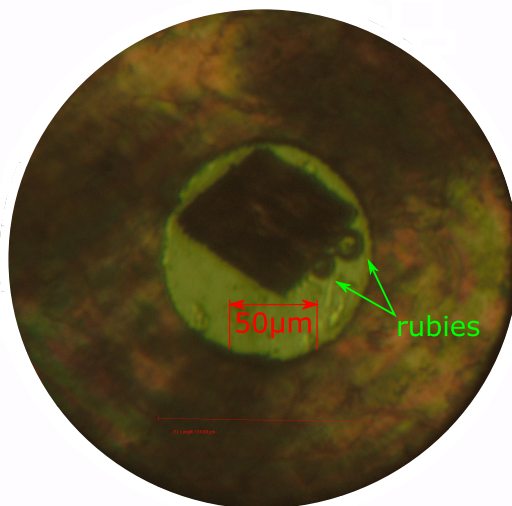


Figure 1.5: Picture of a Ni sample in a pressurized loaded DAC. The outer dark ring is the gasket. In the centre it is possible to see the sample (dark rectangle) and two rubies (used for pressure measurements) on the side. The sample is surrounded by the pressure medium (KCL) and squeezed between the two diamonds.

A large variety of pressure media can be used: solid, liquid and even gas. Fluid media present almost no shear stress providing therefore more uniform pressure conditions. When the DAC is coupled to laser heating systems other properties that a pressure medium should have need to be taken in consideration.

The chosen material should be chemically inert in all the temperature range of the experiment. Also, the pressure medium should be transparent, to let the laser heat the sample, and it should present a low

thermal conductivity: diamonds have very high thermal conductivity and this could cause very large thermal gradients if a proper insulation is lacking. At very high pressures ( $P > 100$  GPa), the pressure medium becomes thinner and thinner, causing problems in the accuracy of temperature measurements [14] [23]. The high compressibility of gases could be a disadvantage in terms of thermal insulation and, therefore, could cause more problems in temperature measurements [16]. The medium chosen in our experiments is KCl.

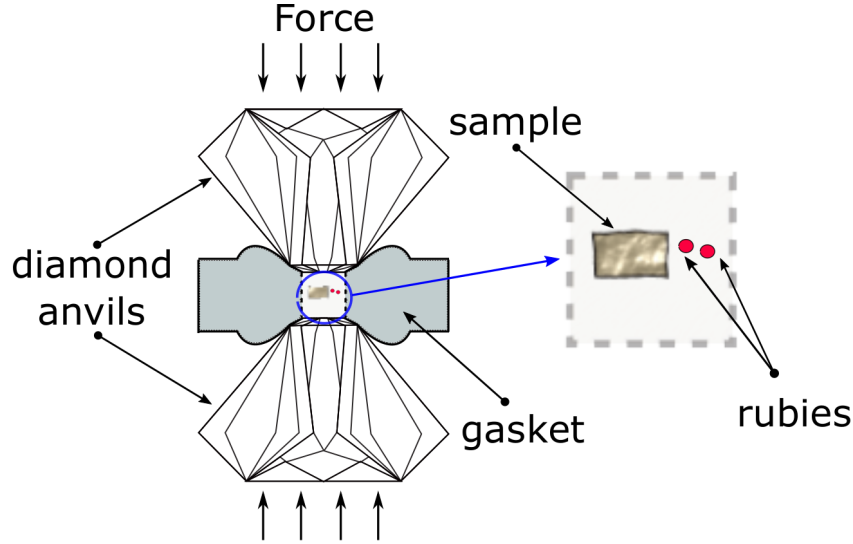


Figure 1.6: Drawing (not to scale) showing the principle of the DAC. The sample is kept in a pressure medium and is squeezed by the diamond heads. One or more rubies are placed near the sample to perform pressure measurements. When the force is exerted on diamonds, the gasket gets distorted: indeed, it is the friction between the gasket and the diamonds that allows the pressure medium and the sample not to come out from the DAC.

The laser used in LHDAC experiments should fulfill some requirements. It should have beam power and point stability, high power (about 100W) and suitable wavelengths [16]. Luckily, the progress on solid state near infrared lasers has created a large span of possibilities [19] [5]: it is then likely to find the kind of laser that matches both general LHDAC requirements and the particular setup specifications.

Since in diamond anvil cells pressure can be kept for a long time, when investigating melting curves, experiments are carried out keeping the same cell pressure and probing the sample at different temperatures (temperature runs). To determine reliable phase diagrams, pressure and temperature should be measured. In particular, when it comes to temperature measurements, reaching an adequate accuracy could be particularly problematic; section 1.3 is then dedicated to a more detailed analysis of spectroradiometric temperature measurements in laser heating setups.

The pressure in the DAC can be measured quite accurately using different methods: monitoring the wavelength position of ruby fluorescence, by observing the Raman spectrum of single crystal diamond or by analysing the diffraction pattern of the pressure medium. In the ruby fluorescence method [24], one or more rubies ( $\approx 5 \mu\text{m}$ ) are placed close to the sample during the loading and the pressure is measured by measuring the peak fluorescence shift of the ruby when excited either with x-rays or a green laser. This method is based on the strong pressure dependence of the wavelength position of ruby fluorescence on the pressure and permits accurate pressure measurements [25].

When XRD is used, it is possible to retrieve the pressure of a material whose equation of state is known: from XRD the material volume is directly obtained, and if the temperature is known, it is possible to evaluate the pressure provided the equation of state  $P = P(V,T)$  is also known [8]. In a laser heating run the pressure is measured before and after the laser heating, since it is not possible to measure it during heating. During the temperature run the pressure doesn't remain constant. This is due to the fact that, since the volume of the cell is constant, when temperature increases, so does the pressure. This

phenomenon is called thermal pressure [16] and its calculation is uncertain, but approximations can be made; thermal pressure corrections are generally small (few GPa).

## 1.3 Temperature measurements in the LHDAC

In section 1.2 the LHDAC, as a method of reaching extreme conditions, has been introduced. Issues regarding pressure and temperature measurements have been presented; pressure methods have been described. A deeper analysis of temperature measurements in diamond anvil cells follows.

### 1.3.1 Introduction to Pyrometry

In situ temperature measurements in the LHDAC are mainly performed by optical micro-pyrometry techniques. These techniques consist essentially in analysing the thermal radiation spectrum emitted from an hot sample. A specific optical setup is used to collect the sample electromagnetic radiation and to bring it to a spectrometer.

Thermal radiation originates from the kinetic energy of the particles which constitute matter. This kind of radiation is associated with the thermal motion of ions and electrons in matter and, therefore, every object emits it. In fact, when charged particles (electrons, ions) undergo an acceleration they emit electromagnetic radiation; in this way, kinetic energy due to the particle temperature is transformed into electromagnetic energy in a wide spectral range. In matter, each particle feels the auto-consistent electromagnetic field of the other particles and therefore they continuously experience accelerations due to Colombian collision, to dipole oscillations and so on.

What Kirchhoff found out in the second half of the nineteenth century is that, in thermodynamically equilibrium conditions, the thermal radiation follows a universal law independent of the material and of all the experimental configuration details. To understand what this “universal law” is about let us define two important quantities. We call “emissive power”  $e(\nu, T)$  the derivative of the emitted thermal power with respect to frequency, that is:  $e(\nu, T) = \frac{dW}{d\nu}$ .

We then define “absorptivity”  $a(\nu, T)$  the fraction of radiation power which is absorbed from the surrounding by a body and is not reflected nor transmitted. Absorptivity is a dimensionless quantity and it obeys the relation  $a+r+t=1$ , which implies that absorptivity is always smaller than one. What Kirchhoff found out was that the ratio between emissive power and the absorptivity is the same for all the bodies:

$$\frac{e(\nu, T)}{a(\nu, T)} = f(\nu, T) \quad \text{Kirchhoff's law}$$

where  $f$  is the universal function [26]. This equation states that a body emits only those frequencies that it can absorb: whenever the absorptivity is small, so has to be the emissive power in order to keep their ratio constant [27]. The key to find  $f(\nu, T)$  is to consider a body with  $a(\nu, T) = 1 \forall \nu$ : this is called Black Body. A Black Body is then an opaque body that absorbs all the radiation that impinge on its surface. This can be thought of as a cavity with a tiny hole: all the radiation coming from outside is experiencing lots of reflections and, in each of these reflections, it is partially absorbed (see Figure 1.7). If the hole is small enough the electromagnetic radiation is completely absorbed before it can escape from the cavity. So, in a quantum mechanical picture, almost all the photons are trapped inside and they are continuously emitted and reabsorbed by the cavity internal surfaces. If temperature is constant in the cavity and all over the surface, then the whole system is considered to be in thermal equilibrium. In these conditions is then clear that the emissive power corresponds exactly to the universal function proposed by Kirchhoff.

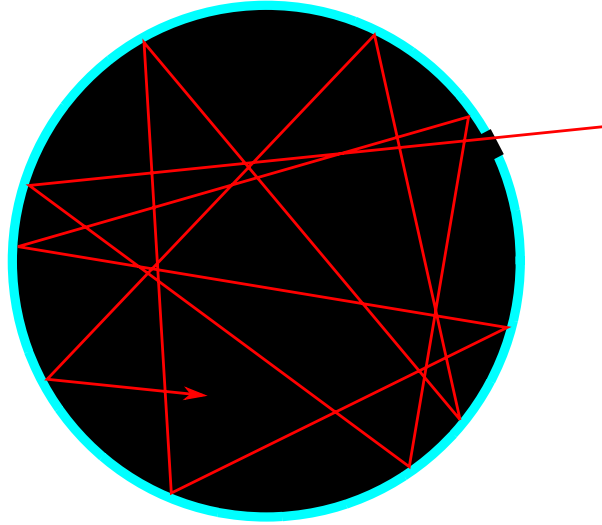


Figure 1.7: Drawing illustrating Black Body principle. Whichever the material, a cavity with a small hole is always a good approximation of a Black Body [26]: the small light intensity that turns out to enter the cavity undergoes many reflections and, at each reflection, it is partially absorbed. In the end, the light coming from outside the cavity will be entirely absorbed and the emission of the cavity is essentially related to the thermal emission of the inner surfaces.

Thermal radiation emitted from a Black Body in thermal equilibrium is called “Black Body radiation”; this radiation is unpolarised and spatially and temporally incoherent [28]. Moreover, since the absorptivity of a Black Body is equal to one for all frequencies, the Black Body radiation is emitted uniquely from the surface: as a matter of fact, even if light were emitted from the bulk, it would be absorbed. For a real perfectly flat body the absorptivity is less than one, depending on the material, and it is usually wavelength dependent. Then, it is useful to define a new adimensional parameter  $\epsilon$ , called “emissivity”, which considers emission differences from the Black Body one. This new parameter is defined as the ratio between the radiant flux density of the real body over the Black Body one, where the radiant flux density is the energy emitted per time and area unit. Kirchhoff’s law can then be written in terms of emissivity:  $\epsilon(\nu, T) = a(\nu, T) \forall \nu$ , where  $\epsilon(\nu, T) = \frac{e(\nu, T)}{f(\nu, T)}$ . Emissivity can take on values between zero and one; if the emissivity is constant over all the wavelengths and it is smaller than one, than the body is generally referred to as “Grey Body”.

In real bodies, surfaces are never perfect and they could present different levels of roughness, curvature or oxide coatings; such flaws of the surfaces modify the emissivity and absorptivity values of materials. In these cases the concepts of emissivity and absorptivity are replaced by emittance and absorbance. Moreover, surface properties could also modify the angle and the polarization with which light is emitted [29]. Yet, Kirchhoff’s law is still valid as long as absorbance and emittance are used [29].

Since for a Black Body  $a(\nu, T) = 1$ , the universal function is exactly equal to the emissive power of the Black Body. Considering the Black Body as a cavity with a tiny hole in thermal equilibrium with the radiation inside, the power emitted through the cavity, and, therefore, the emissive power, are directly related to the Black Body energy spectral density (or, as it is usually referred to, “Black Body spectrum”  $u(\nu, T)$ ) [27]:  $f(\nu, T) = e_{BB}(\nu, T) = \frac{c}{4}u(\nu, T)$ , where  $c$  is the light speed. It is then possible to understand the great importance of the Black Body spectrum: knowing its frequency behaviour allows to know all the properties of thermal emission; moreover, since the Kirchhoff’s universal function depends uniquely on the temperature, it is possible to measure a Black Body temperature just by collecting the radiation emitted by the body. This technique is known as pyrometry and it is the one that used to measure temperature in the LHDAC. The Black Body spectrum is given by the famous Planck’s formula [27]:

$$u(\nu, T) = \frac{8\pi}{c^3} \frac{h\nu^3}{e^{\beta h\nu} - 1} \quad \text{Planck's law}$$

Where  $\beta = \frac{1}{K_b T}$ ,  $K_b$  is the Boltzmann constant and  $h$  is the Planck constant. This formula is the expected number of particles in each energy state according to the Bose-Einstein distribution for a boson gas with a null chemical potential. In fact, a photon gas differs from an ideal boson gas because the number of photons is not conserved (photons can be created and destroyed) and, since photons are massless particles, the dispersion relation is linear in energy instead of being quadratic. These two characteristics make the photon chemical potential identically null [30]. Historically, Planck's law has been found in a rather different way and its interpretation has paved the way to quantum mechanics. Briefly,  $u(\nu, T)$  can be found by counting all the electromagnetic normal modes of the cavity included in  $(\nu, \nu + d\nu)$  and multiplying the number obtained by the mean energy for each normal mode [27]:

$$u(\nu, T) = \frac{1}{V}(\text{wave number in } (\nu, \nu + d\nu))(\text{wave mean energy})$$

In reality, it is the calculation of the normal mode mean energy performed using the equipartition theorem or by using a discrete sum that have led respectively to Rayleigh-Jeans' formula [27] and to Planck's formula and, consequently, to the divergent results of classical mechanics and quantum mechanics.

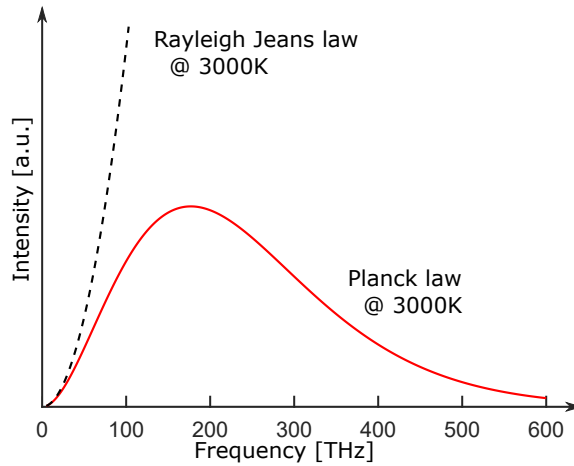


Figure 1.8: Planck's law and Rayleigh-Jeans' law at 3000K. At low frequencies, the two curves agree with each other, but at higher frequencies the Rayleigh-Jeans one diverges; this phenomenon is known as "ultraviolet catastrophe" and it is solved only in a quantum mechanical model of thermal emission (Planck's law).

A typical behaviour of Planck spectrum is illustrated in Figure 1.8. From Planck's formula it is possible to obtain the temporal coherence properties of the radiation emitted from a Black Body. The theorem of Wiener-Khinchin states that the spectral density of a signal coincides with the Fourier transform of its autocorrelation function:  $u(\nu, T) = F\{R(\tau)\}$  [31]. Thus, broad energy density spectra such the Black Body one, correspond to a very small coherence time; for Planck emission, this time can be calculated as  $\tau \simeq \frac{h}{4K_B T}$  [32]. Moreover, through an electromagnetic fluctuation model of thermal radiation [28], spatial incoherence is related to the locality (absence of spatial dispersion) of the optical response of the body to thermal fluctuations [31]. Thus, the theorem of Wiener-Khinchin tells us to expect a broad angle emission for the Black Body radiation. The coherence length can be calculated too and, again, for Black Body radiation  $l = c\tau \simeq \frac{hc}{4K_B T}$ ; for a Black Body at 3000 K, the coherence length is about 1.2  $\mu\text{m}$ . It is worth mentioning that Black Body radiation in the near field (distances smaller than  $\frac{\lambda}{2\pi}$ ) can have great time and space coherence and, therefore show a narrow spectrum and high directionality [31] [28]. In any case, Kirchhoff's law validity has been always found to be respected. Integrating over the frequencies, the Planck's formula lead to the Stefan-Boltzmann's formula which states the dependence of the overall thermal radiation power on the temperature and gives therefore the

power that the body should absorb or generate to maintain thermal equilibrium:

$$W = \sigma ST^4$$

where  $\sigma$  is the Stefan-Boltzmann constant,  $\sigma \simeq 5.7 \times 10^{-8} \frac{W}{m^2 K^4}$  and  $S$  is the body surface. This formula does not tell anything about the frequencies at which radiation is emitted and was discovered experimentally by Stefan and, later, thermodynamically justified by Boltzmann, long before Planck exposed his formula. The frequency dependence is instead the core of the Wien displacement law [27] which links Black Body temperature with the wavelength of the emission peak:  $\lambda_{peak} T \simeq 3000 \mu m \times K$ . Therefore, as  $T$  increases the emitted power increases with the fourth power of temperature, whereas the peak wavelength decreases (Figure 1.9).

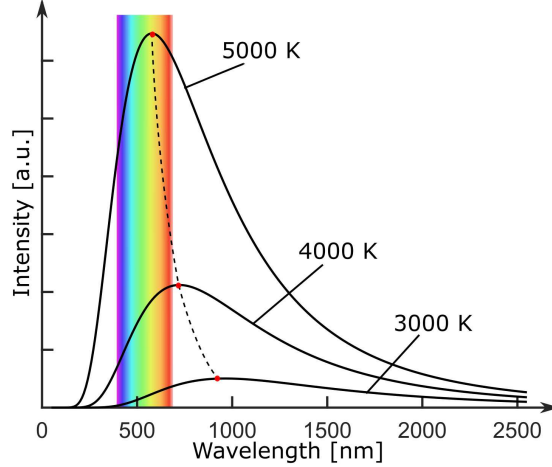


Figure 1.9: Planck spectra at different temperatures as a function of wavelengths. Comparing these spectra, it is possible to observe both the Wien displacement law and the Stephan-Boltzmann one: as the temperature increases, the peak shift towards lower wavelengths and the emitted power (area below the Planck's curve) increases.

For temperature measurements it is useful to introduce two radiometric quantities: the radiance  $L(A, \Omega, t)$  and radiant intensity  $I(A, \Omega, t)$ . The first one is defined as  $L(A, \Omega, t) = \frac{\partial^2 \Phi}{\partial A \partial \Omega \cos \theta}$ , where  $\Phi$  is the radiant energy flux,  $A$  is the body surface and  $\theta$  is the angle between the vector normal to the surface and the considered direction (see Figure 1.10). The importance of radiance lies in the fact that this physical quantity is conserved along ray trajectories in a non-diffusive lossless optical system. In fact, radiance can also be interpreted as the derivative of the radiant energy flux with respect to the étendue<sup>1</sup>; since in a lossless optical system the energy is conserved and since if there are no diffusive elements the étendue is conserved too, then it comes out that radiance is constant through the ray propagation [33] [34]. It is possible to define also the frequency dependent quantity which is called spectral radiance:

$$L_\nu(A, \Omega, \nu, t) = \frac{\partial^3 \Phi}{\partial \nu \partial A \partial \Omega \cos \theta}$$

The quantity which is measured by a pyrometer is the spectral radiant intensity:  $I_\nu(A, \Omega, \nu, t) = \frac{\partial^3 \Phi}{\partial \nu \partial A \partial \Omega}$ . This quantity is the one integrated by the CCD used to collect the emitted radiation and, therefore, the energy on each pixel of the CCD is:

$$E_{pixel} = \int_S \int_\alpha \int_{\Delta \nu} \int_\tau I_\nu(A, \Omega, \nu, t) dt d\nu d\Omega dA$$

<sup>1</sup> $\delta(\text{étendue}) \equiv n^2 \delta S \delta \Omega \cos(\theta)$ , where  $\delta S \cos(\theta)$  is the area projected along the line of sight [33].

Where  $\Delta\nu$  is the overall frequency resolution,  $\alpha$  is the half width of the cone of light collected by the optical system,  $\tau$  is the integration time and  $S$  is the body surface.

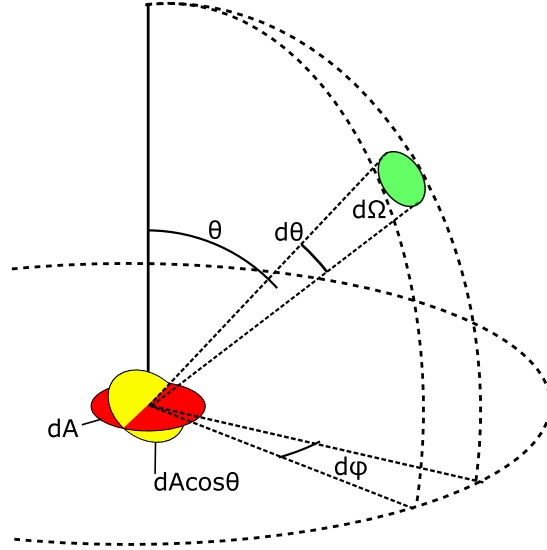


Figure 1.10: Schematic illustrating the geometry of radiant emission. Radiance is defined as the radiant flux divided by the solid angle ( $d\Omega$ ) at which the radiation is emitted and by the emitting surface ( $dA\cos\theta$ ) perpendicular to the considered direction.

The Black Body is, in good approximation, a Lambertian source [29] which means that the radiant intensity has a cosine distribution:  $I_\nu(\theta) = I_\nu(0)\cos(\theta)$  (see Figure 1.11). It is then straightforward to realise that this means that radiance is uniform:  $L_\nu(\theta) = L_\nu(0)$ . In case of a Lambertian source we can therefore write the spectral radiant intensity as  $I_\nu(\theta) = L_\nu\cos(\theta)$  and the energy collected by the CCD becomes:

$$E_{pixel} = \int_S \int_\alpha \int_{\Delta\nu} \int_\tau I_\nu(A, \Omega, \nu, t) dt d\nu d\Omega dA \simeq \int_S \int_\alpha \int_{\Delta\nu} \int_\tau L_\nu(A, \nu, t) \cos(\theta) dt d\nu d\Omega dA \simeq \tau S \Delta\nu \int_\alpha L_\nu \cos(\theta) \sin(\theta) d\theta d\phi = \tau S \Delta\nu L_\nu \int_\alpha \frac{\sin(2\theta)}{2} d\theta d\phi = L_\nu \tau S \Delta\nu \pi \sin^2(\alpha) \sim L_\nu (NA)^2$$

Where NA is the numerical aperture of the optical system used to collect light coming from the body. We can now write Planck's law in terms of radiance:

$$L_\nu = \epsilon \frac{2h\nu^3}{c^2} \frac{1}{e^{\beta h\nu} - 1}$$

In this version of Planck's formula we have also inserted the emissivity coefficient (or, better, the emittance) to remember that when temperature is measured spectroradiometrically in real cases, Planck's law is valid as long as we use an empirical emittance coefficient that accounts for the particular choice of the material and its surface properties. Although when deriving Planck's formula it is usually convenient to work with frequencies, during experiments the Black Body is usually analysed in terms of wavelengths. It is possible to obtain the wavelength dependent Planck's law by remembering that:

$$L_\nu d\nu = L_\lambda d\lambda \Rightarrow L_\lambda = L_\nu \frac{\nu}{d\lambda} \Rightarrow L_\lambda = L_\nu \frac{d\left(\frac{c}{\lambda}\right)}{\lambda} \Rightarrow L_\lambda = -L_\nu \left(\frac{c}{\lambda^2}\right)$$

Therefore:

$$L_\lambda = \epsilon \frac{2hc^2}{\lambda^5} \frac{1}{e^{\beta h \frac{\epsilon}{\lambda}} - 1}$$

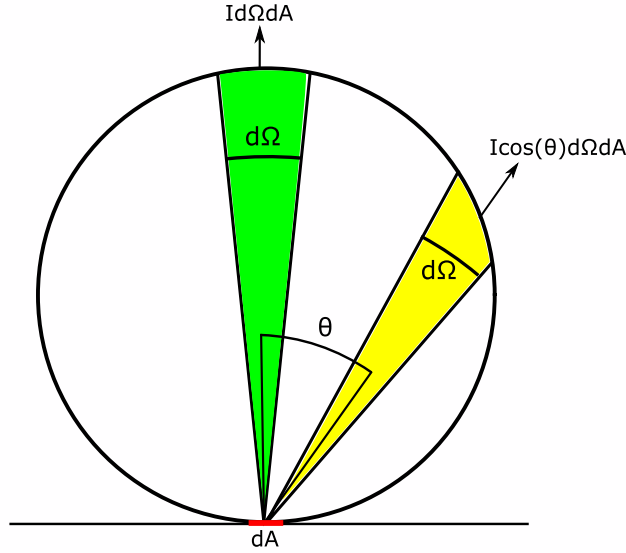


Figure 1.11: Lambertian source drawing. The intensity of thermal emission depends with a cosine law on the angle ( $\theta$ ) formed with the perpendicular to the emitting surface.

When thermal radiation is collected the temperature of the Black Body which has been analysed can be obtained in different ways. The procedure usually applied in LHDAC systems is to fit the Black Body spectrum using Planck's law in the grey body approximation. With this method, temperature can be measured with high precision as long as the spectrum collected has not been distorted by the optical system. The fit parameters are then the temperature itself and the emittance coefficient, which is being considered wavelength independent. The grey body approximation could lead to errors in spectroradiometric temperatures of about 10% which means about one hundred K [35] [36] [37].

The main characteristic that make pyrometry an useful technique in LHDAC temperature measurements is the possibility to measure high temperatures with no contact with the sample, which means no sample conditioning. Moreover, temperature measurements can be performed using the same optical system and spectrometer used, for example, for pressure measurements without needing to add further equipment. Another property of the radiometric analysis of Black Body spectra is that the accuracy depends, once the wavelength range has been chosen, on the body temperature [1]. Furthermore, precision depends on temperature since, for Stefan-Boltzmann's law, the number of photons rises with the fourth power of temperature and the emission peak moves towards lower wavelengths according to Wien displacement law. Sometimes a linear approximation of Planck's law, known as Wien approximation, is made. This approximation can be sometimes useful to evaluate the accuracy of temperature measurements and will be extensively explained in the next section. Moreover, as claimed by Walter and Koga [1] the precision of the Wien fit is not affected by linear dependent variations of the emittance coefficient whereas the Planck fit is. Anyway, Kantor [5] recommends to always use the Planck fit, because the emittance does not always vary linearly and, when it does, the Wien plot can conceal serious accuracy errors in temperature measurements [38]. In any case, the Wien approximation always introduces temperature dependent errors in accuracy which increase at higher temperature reaching 1% at 5000 K [1]. The Wien formula is derived below:

$$L_\nu = \epsilon \frac{2hc^2}{\lambda^5} \frac{1}{e^{\beta h \frac{\epsilon}{\lambda}} - 1}$$

$$if \quad e^{\beta h \frac{c}{\lambda}} \gg 1 \Rightarrow L_{Wien} = \epsilon \frac{2hc^2}{\lambda^5} e^{-\beta h \frac{c}{\lambda}}$$

We can then define as "Wien" the following quantity:

$$Wien = \frac{K_B}{hc} \ln(L_{Wien} \frac{\lambda^5}{2hc^2})$$

Therefore:

$$Wien = \frac{K_B}{hc} \ln \epsilon - \frac{1}{\lambda T}$$

From this formula clearly emerges the dependence of the Wien with  $1/T$ .

### 1.3.2 Two-Colour Sliding Pyrometry

Although Planck and Wien fits can provide precise temperature measurements, these techniques are not able to determine the accuracy of the measurements and they could hide substantial temperature errors in the emissivity coefficient. Therefore, even if the temperature standard deviation obtained in Planck fit (about few degrees) is usually provided to account for the lack of accuracy in temperature measurements, it is believed that the actual error is significantly larger, about hundreds of Kelvin [39]. The "sliding two-colour" technique is a method, often reported in literature, to investigate potential wavelength dependent irregularities with respect to the grey body radiation which could arise from emissivity variations, optical misalignments, miscalibrations, spherical or chromatic aberrations and so on [38]. It is therefore a useful complementary method that could be applied to estimate the fit accuracy. The principle of this technique relies on the Wien linear approximation of the Planck formula; in fact, considering  $\omega_i = -\frac{hc}{K_B \lambda_i}$ , the temperature of the body can be obtained from [8]:

$$T_{two-colour} = \frac{\omega_2 - \omega_1}{Wien(\omega_2) - Wien(\omega_1)}$$

which can also be written as function of wavelengths [39] [38]:

$$T_{two-colour}(\lambda) = \frac{(\frac{1}{\lambda}) - (\frac{1}{\lambda+\delta})}{Wien(\lambda) - Wien(\lambda + \delta)}$$

The next step is to choose a proper frequency window  $\Delta\omega = \omega_2 - \omega_1$  or, since from the spectrometer we obtain the Planck spectrum as a function of wavelength,  $\delta$ . The wavelength window is then shifted over the entire spectrum and for each  $\lambda_i$  the  $T_{two-colour}$  is calculated. Doing so, it is possible to get plots like the ones shows in 1.12(a) and 1.13(a). Only temperatures constant over the spectral range can be accepted [38]. Some information could be extracted from the histogram of the occurrence number of two-colour temperatures; according to Benedetti et al. the two-colour temperature distribution should be Gaussian [39]. The application of both criteria is illustrated in Figure 1.12 and Figure 1.13.

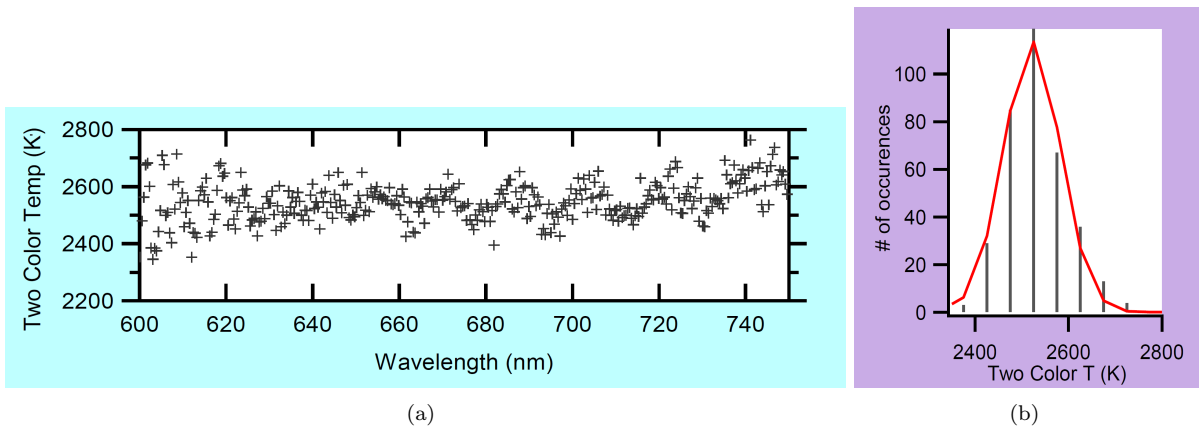


Figure 1.12: Two-colour fit on the left, histogram on the right. Example of an acceptable measurement: the two-colour is flat and the histogram is Gaussian. From [8].

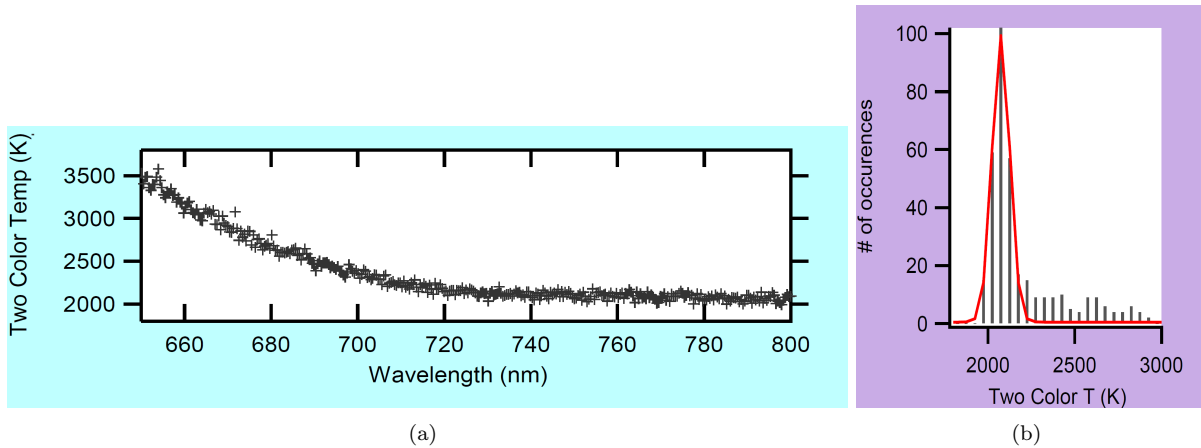


Figure 1.13: Two-colour fit on the left, histogram on the right. The two-colour fit is not flat, indicating that the temperature measurement is not reliable. These conclusions can also be inferred by looking at the histogram: the two-colour distribution is far from being Gaussian. From [8].

The two-colour method is useful for its wavelength sensitivity but, on the other hand, since two-colour temperatures are not the result of a fit but obtained as angular coefficient of a straight line, the two-colour technique is strongly affected by noise. These two features have to be taken into consideration when choosing the wavelength window: if  $\delta$  is too small then the two-colour plot will have a very high wavelength sensitivity but it will be highly affected by the noise. On the contrary, if the the wavelength window is too large, the noise will be under control but it won't be possible to observe any wavelength variation. In Figure 1.14 the average of two-colour temperatures and its standard deviation have been plotted by Benedetti et al. as a function of  $\delta$ (in pixel); the appropriate window should be chosen as the smallest window at which the center of the histogram is flat and the standard deviation is as low as possible.

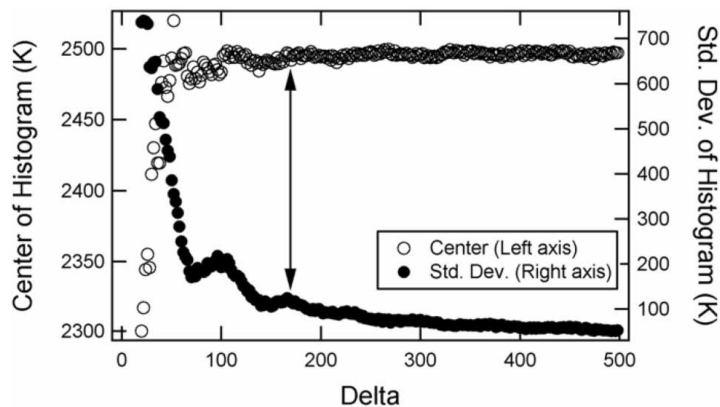


Figure 1.14: Plot of the central value (centre) and standard deviations of two-colour histograms as a function of wavelength windows  $\delta$ (in pixel). This plot is made to choose the best wavelength difference with which drawing two-colours graphs. From [39].

In summary, in order to consider a temperature as acceptable the following three conditions have to be satisfied:

1. The spectrum collected is well fitted by Planck's law in grey body approximation.
2. The two-colour temperature is constant over the full wavelength range.
3. The histogram is Gaussian.

The problem of choosing an appropriate error for spectroradiometric measurements is still open; Benedetti et al. suggested to consider the histogram standard deviation [39]. This choice provide an error which is certainly larger than the one obtained from the fit of the Planck's curve, thus giving a more realistic description of the order of magnitude of the error. However, since problems in temperature measurements arise from systematic errors and not from the setup precision and, therefore, stochastic errors (which are given by the Planck fit and are about few K)(see subsection 2.2.2), it is undeniable that a further investigation of spectroradiometric temperature measurement accuracy is needed.

Indeed, numerical simulations of each kind of systematic error contribution have been made more than once [39] [38] [1], but, due to the large variety of experimental parameters and conditions, it is impossible to compare temperature measurements acquired with different setups. An experimental estimation of the bias introduced by different setups is still lacking and it has been the subject of this work.

### 1.3.3 Thermal radiation collecting optics in the LHDAC: critical points

Collecting photons from the sample and taking them to the entrance of the spectrometer, where they will be spectrally analysed, requires a proper optical system. Since the optical path which is crossed by the light rays is not a free space propagation, some image distortions could occur. In the LHDAC, the thermal radiation is usually collected in an extended visible range (500 – 1000 nm) and two kinds of optics are used: refractive (lenses) and reflective (mirrors). The aim of this section is to introduce the principal properties of these systems including a comparison between the optics which have been used in our experiments: mirrors on ID27 and lenses on ID24. In Figure 1.15 an outline showing the principle of spectroradiometric measurements in the LHDAC is illustrated. The sample thermal emission goes through the optics and some filters before reaching the pinhole at the spectrometer entrance. Both optics (lenses and mirrors) and filters can introduce image distortions; however, whereas filter effects can be calibrated out, those due to the imaging optics cannot. In fact, the effect of the filters is merely a distortion in the spectrum frequency: the original signal can be recovered knowing the filters spectral response:

$$Signal_{orig.}(\lambda) = \frac{Signal_{measured}(\lambda)}{Filter(\lambda)}$$

On the other hand, as will be explained, the effect of lenses and imaging mirrors is strongly related to the shape of the hot spot on the sample and, therefore, the original signal cannot be easily recovered.

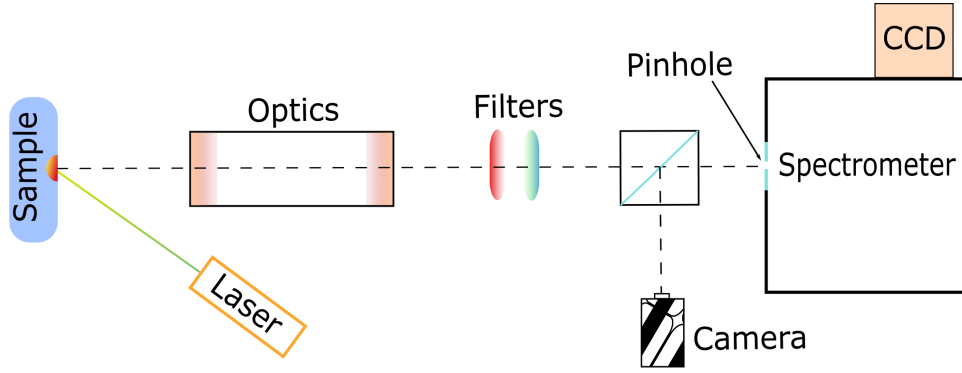


Figure 1.15: A simplified outline of spectroradiometric temperature measurements in the LHDAC. The sample is kept in a diamond anvil cell and heated with a laser. The optical system is used to collect light and to take it to the spectrometer entrance (pinhole). Around the pinhole, there is usually a mirror which reflects the image of the sample; this image is collected by a camera allowing to align the optics on the desired spot.

In LHDAC experiments the sample is held in a diamond anvil cell and it is heated with a high power laser (about 100 W) usually Gaussian shaped and operating in continuous mode. In order to reach high pressures, the sample surface is typically very small (less than  $1000 \mu\text{m}^2$ ); moreover, to reach high temperatures, the laser should be focused onto the sample and the resulting spot is quite small too: about  $10\text{-}20 \mu\text{m}$  determined with  $1/e^2$  criterion (i.e. at 13.5% of the maximum intensity). The resulting hot spot is usually not uniform and it is about  $20\text{-}30 \mu\text{m}$  of FWHM which is, in any case, much larger than the x-ray probe (few  $\mu\text{m}$ ). Since the hot spot is typically smaller than the sample, many temperature runs can usually be performed in different sample position with the same sample loading in the DAC.

The pinhole diameter is about several tens of  $\mu\text{m}$ ; so, if the sample was imaged on the spectrometer entrance with the same scale, the entire hot spot would be analysed in the spectrometer. Since the temperature which would be desirable to measure is the peak temperature, approximately in the spot centre, the image on the spectrometer has to be enlarged. For this reason, the optics are also used to magnify the image to let the spectrometer sample the very top of the hot peak. Of course, the magnifying factor should not be too large: the drawback of a better temperature resolution is the loss of photons entering the spectrometer.

The simplest way to describe the imaging formation process is by using the so-called point spread function (PSF), which is the image of a point source formed by an optical system (see section 3.1 for more details). The point spread function is the equivalent of the linear system impulse response for an optical system: every image is then simply described by the convolution between the point spread function and the intensity on the object plane (sample). The PSF of a cylindrical symmetric optical system with no aberrations is an Airy disk which is described by the following formula [40]:

$$I(r) = I_0 \left( \frac{2J_1(kr \frac{D}{2f})}{kr \frac{D}{2f}} \right)^2$$

where  $J_1$  is the first order Bessel Function,  $D$  is the optics aperture diameter,  $k$  is the wavelength vector,  $f$  is the distance between the aperture and the image plane, and  $r$  is the radial displacement on the image plane.

The Airy disk represent the ultimate limit to spatial resolution, i.e. the smallest detail that can be observed and, therefore, imaged by the considered optics. One of the most used criteria is Rayleigh's: two points can be resolved if the contrast between the maximum intensity of the two peaks and the

minimum intensity in between is more than 26% of the peak intensity, which means:  $\frac{I_{max}-I_{min}}{I_{max}} < 26\%$ . When approximating the Airy disk with a Gaussian, the Rayleigh criterion implies that the two points should be at a distance larger than their FWHM. Diffraction limited optical systems show a wavelength dependent resolution given by the formula:  $\delta = 0.61 \frac{\lambda}{NA}$ , where NA is the numerical aperture of the optical system. The point spread function description could be applied both to lenses and mirrors.

Mirrors used to take the image to the spectrometer and to magnify it are usually combined in the so called Schwarzschild configuration (see Figure 1.16); mirrors are free from chromatic aberrations, but they can have some monochromatic aberrations due to their fabrication and to difficulties in the alignment. Conversely, lenses are easier to align but they suffer from chromatic aberrations; particularly critical in temperature measurements are the axial chromatic aberrations which could lead to hundreds of Kelvin errors [1]. More details on these two configurations are provided in subsection 1.3.4.

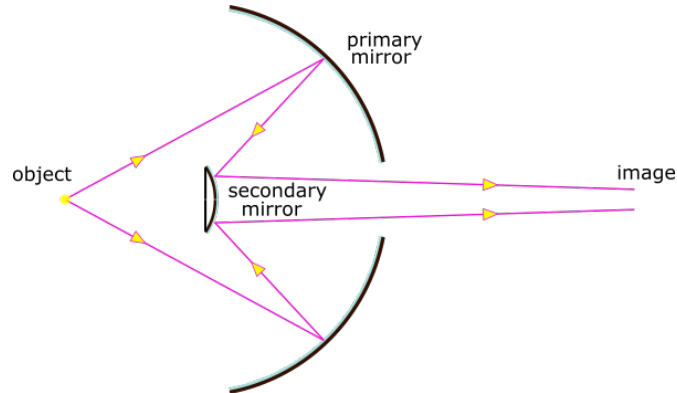


Figure 1.16: Schwarzschild scheme: light is collected by the primary mirror (concave) and then reflected to the secondary mirror. The image is usually formed at greater distances compared to those between the object and the mirrors: this results in a high magnification of the system.

It is possible to have an insight into what chromatic aberrations are by remembering the principles of ray refraction in geometric optics. As illustrated in Figure 1.17 when light enters in a different medium it is refracted accordingly to Snell's law:  $n_1 \sin\theta_1 = n_2 \sin\theta_2$  where  $n_1, n_2$  are the refraction indexes of the two materials and  $\theta_1, \theta_2$  are respectively the angle of incidence and the angle of refraction. The refraction index is wavelength dependent; this means that if two rays at different wavelengths have the same angle of incidence, this will result, in general, in two different angles of refraction. This is exactly what happens in lenses: parallel rays with different frequencies are focused in slightly different positions along the optical axis (Figure 1.18).

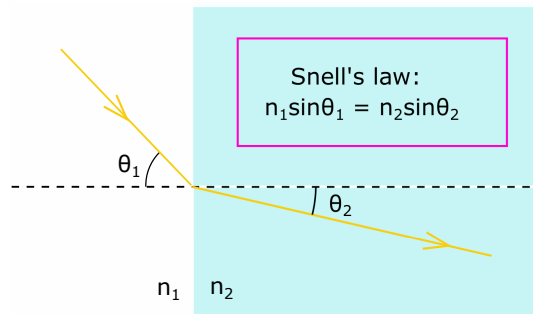


Figure 1.17: Drawing illustrating Snell's law.

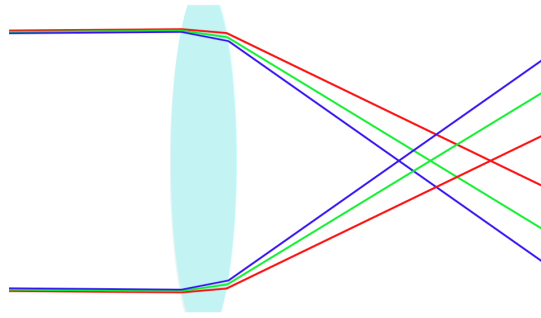


Figure 1.18: Axial Chromatic aberrations: parallel rays at different frequencies are focuses in different position along the optical axis.

For temperature measurements, it is convenient to depict chromatic aberrations in a slightly different way. In 1.19(a) it is possible to see the effect of having different focal distances for different wavelengths: if the image plane corresponds, for example, to the green focal distance, then the red light will be unfocused and, consequently, will draw a broader spot on the image plane. Hence, on the image plane, lens chromatism results in a wavelength dependent resolution and, therefore, in a wavelength dependent PSF. The wavelength behaviour of axial chromatic aberrations can be very complicated and, furthermore, depends on the position of the image plane with respect to the lens (which means which wavelength is focused).

One method to reduce the effect of chromatic aberrations is to put a pupil (also called iris) in front of lenses [41]. As can be seen from 1.19(b), the iris cuts marginal rays hence giving a shorter depth of focus and, therefore, a smaller spot on the chosen image plane. The drawback consists in the reduction of the numerical aperture: as it has been shown, this turns out in photon flux reduction and in a resolution deterioration. Then, the numerical aperture (NA) should be chosen considering a balance: the NA should guarantee the diffraction limit in the frequency range chosen for the Planck fit; at the same time, resolution and measurement time should respect the experimental constraints required.

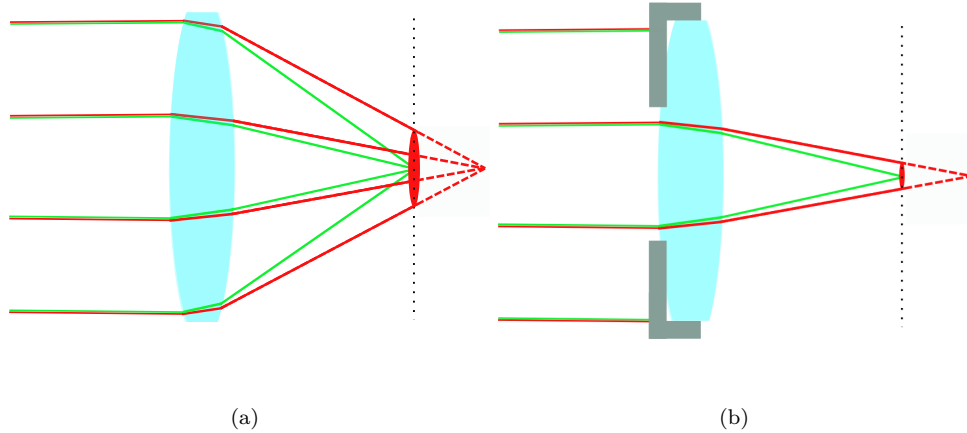


Figure 1.19: (a) shows the resolution effect of chromatic aberrations. (b) illustrates the effect of Iris in reducing the chromatic aberration broadening by cutting marginal rays. Dashed black line represent the image plane considered.

The chromatic aberration effect on the resolution is fundamental to understand the effect of chromatism on temperature measurements. Intuitively, if the thermal radiation source whose temperature is analysed is large and uniform, the Planck fit of the Black Body gives quite accurate temperature values. Errors in temperature measurements in the LHDAC arise when the hot spot on the sample is not uniform and they increase as temperature gradients get steeper [1]. These gradients are mainly due to the limited thermal insulation of the pressure medium [14] and, although they can be reduced by, for example, defocusing the laser to have larger spots, they can't be totally avoided. An inhomogeneous temperature profile generates wavelength emission profiles as shown in Figure 1.20. These profiles are then convoluted with the wavelength dependent PSF of the chromatic aberrated optics resulting in a distorted spectrum. Moreover, the profile obtained on the spectrometer entrance is then averaged by a pinhole, introducing further variations in the original spectrum. Usually, the effect of the pinhole is negligible and its dimension is kept as tiny as possible providing the photon flux is sufficient for temperature measurements.

Since also a diffraction limit system shows a wavelength dependent behaviour, these systems distort the measured spectrum as well; usually, chromatic aberrations are more relevant, but the diffraction limited contribution should not be completely ignored. Anyway, even if the PSF does not depend on wavelength, the wavelength profiles of the emitted radiation would be all convoluted with the same PSF, resulting in enlarged wavelength profiles on the spectrometer. This would cause, once again, a loss in measurement accuracy. In the end, as illustrated in Figure 1.21, the only way optics resolution could be ignored is by providing a large uniform hot spot.

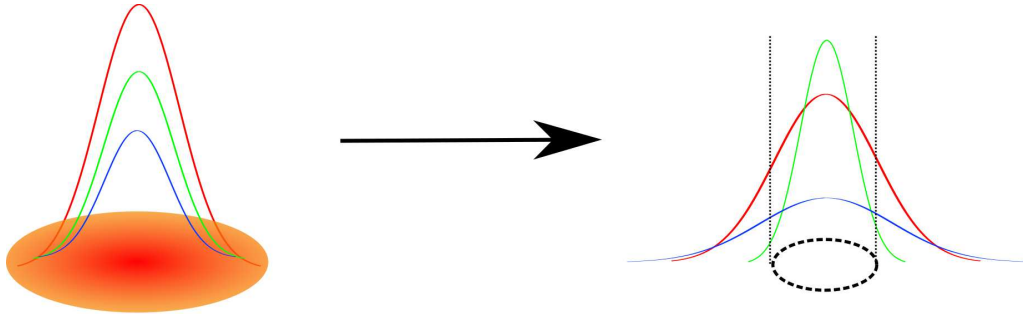


Figure 1.20: Effect of chromatic aberrations on temperature profiles. On the left the profiles of three different wavelengths are shown; on the right the profiles once they reach the spectrometer entrance. Wavelength dependent point spread function can strongly distort spectra causing extensive errors in temperature measurements. Dashed black circle on the right side: pinhole.

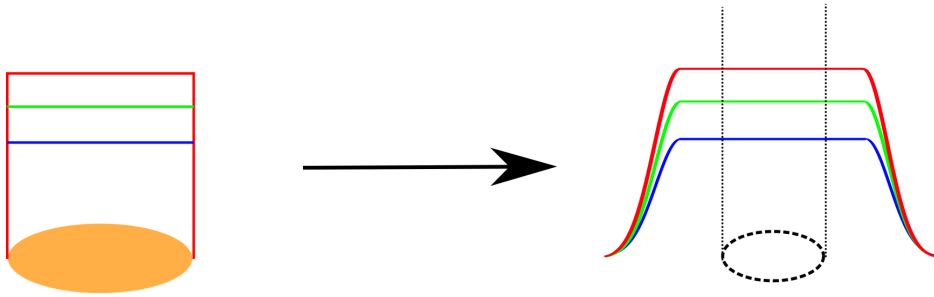


Figure 1.21: With a uniform hot spot the pinhole is sampling the same spectrum emitted by the sample. Measurements are not affected by chromatic aberrations.

### 1.3.4 Schwarzschild and achromatic doublets

The aim of this paragraph is to introduce the two optics, one reflective and one refractive, that have been used and compared throughout this work. These two optics have been taken directly from two different beamlines and are the ones used normally for laser heating experiments. Optics based on mirrors have been taken from ID27 whereas the refractive one comes from ID24. These two optical systems are shown in Figure 1.22 whereas a brief outline of the laser heating setups of the two beamlines is presented in the next section.

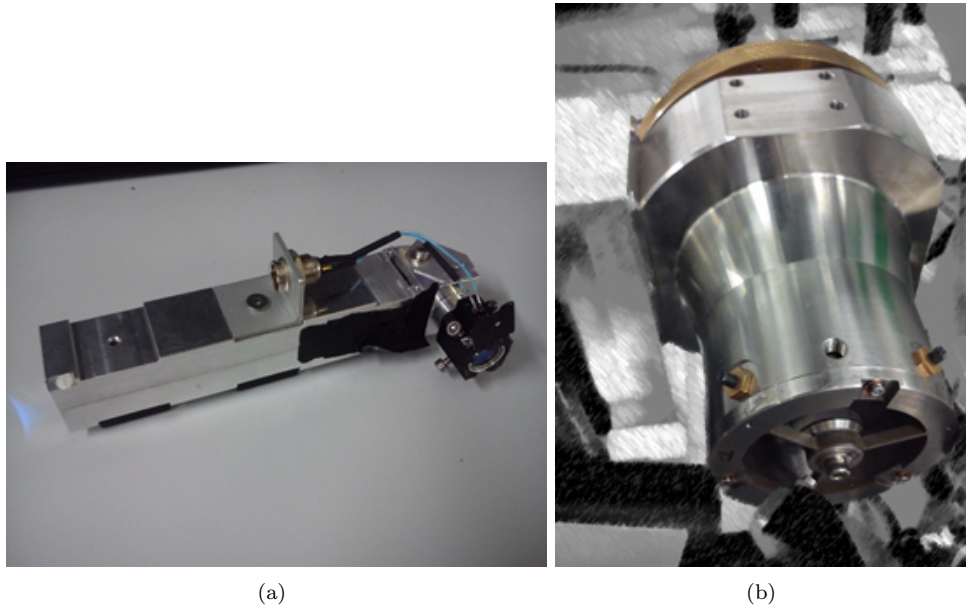


Figure 1.22: On the right: mirror based optics (Schwarzschild) from ID27. On the left: achromatic doublets inserted in custom-built microscope units from ID24.

ID27 mirrors are assembled in the Schwarzschild configuration ( Figure 1.23); this kind of objective consist in two mirrors: one ( $M_p$ : primary mirror) is planar-concave, the other one is planar-convex ( $M_s$ : secondary mirror). Thermal radiation is collected from the object by the primary mirror and brought to the image plane by the secondary mirror. Mirrors guarantee the Schwarzschild to be chromatic aberrations free; on the other hand, fabricating such small mirrors with the necessary quality is challenging. Moreover, the Schwarzschild configuration cuts naturally most of the paraxial rays, exposing the system to stronger monochromatic aberrations (e.g. spherical aberrations), and it is very sensitive to mirror alignment. It is therefore unlikely that the Schwarzschild can reach the diffraction limit; however, the absence of chromatism represent a relevant advantage over lens based systems.

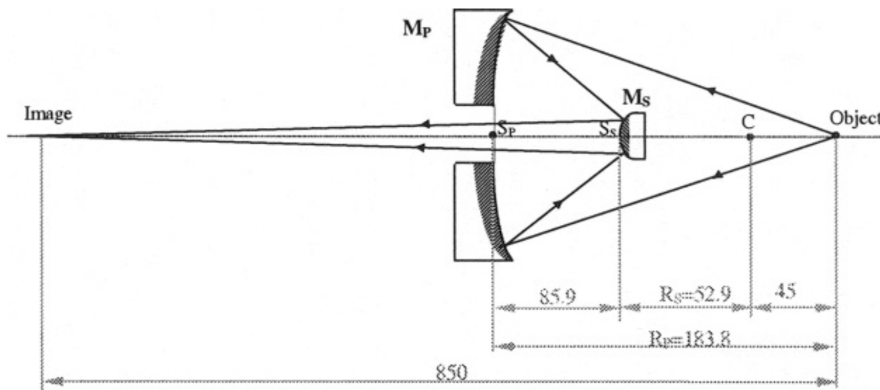


Figure 1.23: ID27 Schwarzschild scheme [42].  $M_p$  is the primary mirror,  $M_s$  is the secondary one. The distance between the image and the object is 859mm and the one between the primary mirror and the object is about 184mm; this configuration leads to a numerical aperture of 0.18.

On ID24 a refractive optical system is used (Figure 1.24). In this system two achromatic doublets are mounted in an infinity-optical configuration, which means that between the two lenses rays are

parallel. These achromats guarantee that two different wavelengths are brought at a common focus to reduce chromatic aberrations. In any case, aberrations are not completely suppressed and, therefore, a pupil is placed in front of the objective during temperature measurements (the numerical aperture with and without iris is 0.065 and 0.2 respectively). Lens alignment is performed with the iris open using a laser to simulate the optical path that should pass in the very centre of both lenses, in order to reduce non-paraxial rays.

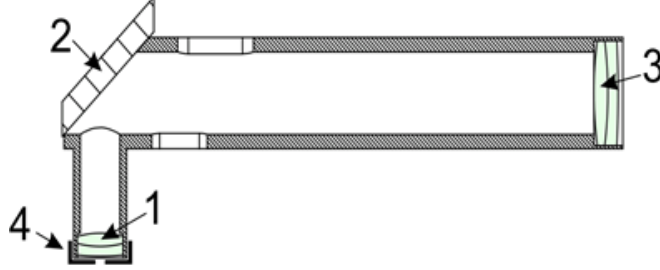


Figure 1.24: ID24 microscope schematic [5]. The objective focal length(1) is 30mm, the field lens(3) one is 500mm. A mirror (2) is placed at 45° between the two lenses and an iris (4) can be put in front of the objective during temperature measurements. The numerical aperture without iris is 0.2, with iris is around 0.065.

The different numerical apertures between ID27 Schwarzschild and ID24 reduced aperture lenses (lenses with an iris in front of the objective) set a difference in the photon flux collected by the two optics. As it has been shown in subsection 1.3.1 the energy integrated by the CCD increases with the square power of NA; being the ratio between the two numerical aperture around 3, to have the same counts on the CCD, the integration time of reduced aperture lenses has to be 9 times bigger than the Schwarzschild one. This has been also observed experimentally.

## 1.4 Laser heating setups at ESRF

This section is dedicated to introduce the laser heating setups used on ID27 and ID24 for extreme condition experiments. These two beamlines have adopted slightly different procedures and solutions based on their peculiarities; an overview of how measurements are performed on the beamlines helps to get an insight into the criteria that have motivated the choices of the two optics and allows to consider the framework in which they operate.

### 1.4.1 ID24 setup

The ID24 laser heating setup is flexible and compact: the same optics are used to acquire ruby signal (for pressure measurements) and for Raman spectroscopy. This setup can be moved out as a block without dismounting it, in order to perform other measurements. Figure 1.25 is a picture of this setup: the sample, held in a diamond anvil cell, is heated on both sides and the sample thermal emission is collected from both sides too. The light collected is then brought to the spectrometer where two different pinholes allow acquiring both signals (front + back sides of the sample) at the same time; the output temperature in a laser heating experiment is the average of the two temperatures. Sample imaging is performed using the same lenses and a confocal illumination; the spectrometer entrance is made of a mirror tilted by  $\approx 5$  degrees to allow an optical visualisation through a camera without introducing beam splitters and, consequently, without adding more distortions and reducing the system throughput. This camera is equipped with a zoom that allows different levels of sample magnification.

The lasers (120 W, Nd:YAG fiber coupled, 1064 nm) are brought on the sample with dedicated optics which forms an angle of about 30 degrees with the optical axis of the objectives. This configuration allows an independent focus of the laser, avoids laser back reflections and possible lens heating that could distort

temperature measurements. The laser beam is focused with a 50 mm lens on the sample to heat it up to high temperatures. The laser is usually a bit defocused to have a hot spot as uniform as possible and with a reasonable dimension: the actual dimension (around 20-30  $\mu\text{m}$  of FWHM) should be larger than the x-ray beam. ID24 uses x-rays for dispersive EXAFS spectroscopy: the beam is chromatically dispersed to obtain a complete spectrum almost instantaneously (few milliseconds) and it is focused at the sample position. Usually, beam sizes range from 3  $\mu\text{m}$  to 7  $\mu\text{m}$  (for  $E < 9 \text{ KeV}$ ). To reach the adequate accuracy during the measurements, the alignment procedure has to be followed carefully: x-rays, laser, and optics should all be aligned on the same spot of the sample. When performing measurements to obtain melting curves, samples are kept at a fixed pressure and temperature is increased step by step by ramping up the lasers' power. Each measurement at a fixed laser power (i.e. at a fixed temperature) lasts about one second and everything is synchronized by means of an analog trigger. The measurement protocol is described in chapter 4

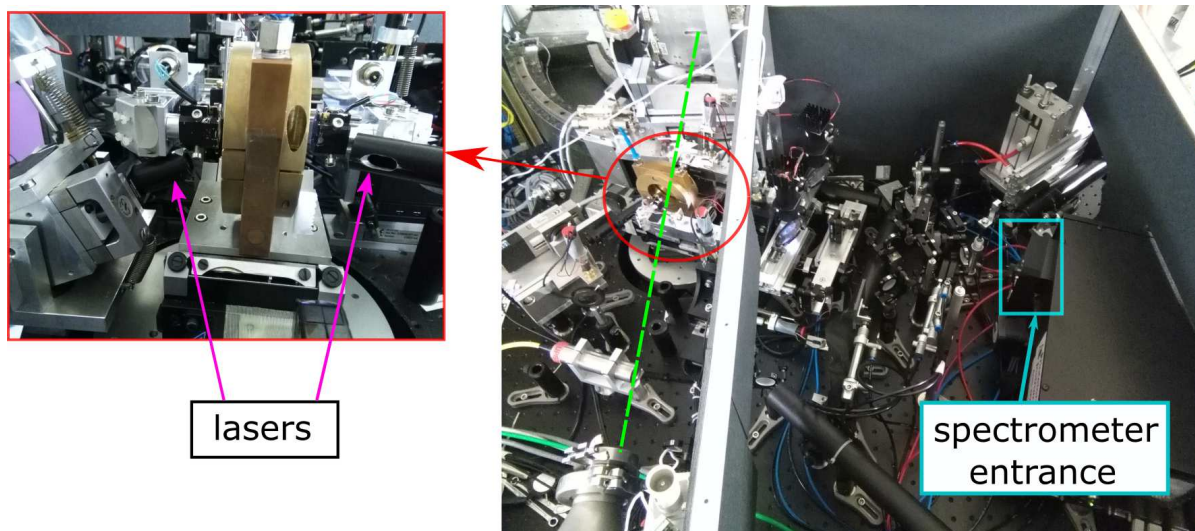


Figure 1.25: Right picture: view of the ID24 overall setup. The DAC is kept in the bronze-colour holder marked with a red circle. X-rays (green dashed lines), laser and optics should be all aligned in the same position on the sample. The spectra (Planck, Ruby, Raman) are collected by the optics and brought at the spectrometer entrance (Light-blue rectangle). On the left a detail: the two custom-made objectives are clearly recognizable on both sides of the sample holder. The sample is heated from both sides: the lenses used for the laser focus are positioned at  $\approx 30$  degrees with respect to the objectives.

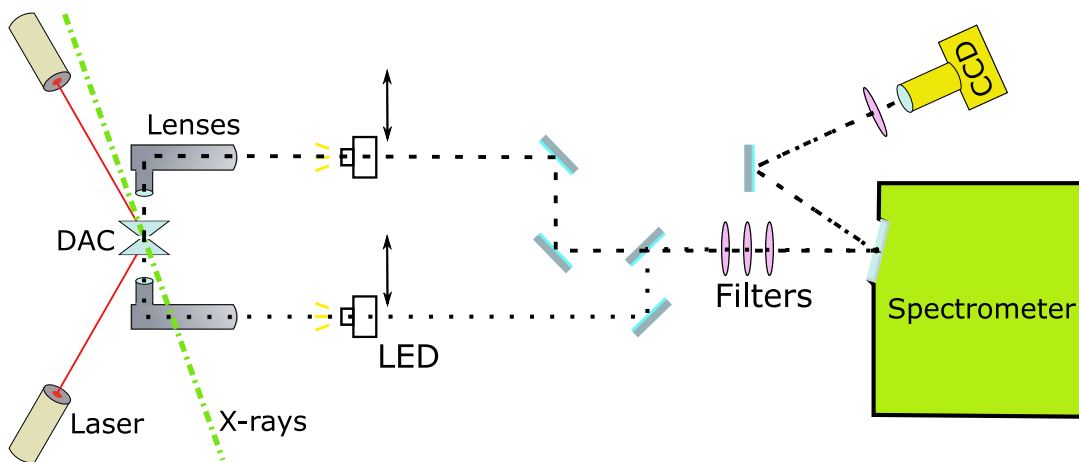


Figure 1.26: ID24 laser heating setup schematic. LED illumination is used for the optics alignment. During measurements lights are off and the LEDs are moved out from the optical path.

### 1.4.2 ID27 setup

ID27 is a beamline dedicated to diffraction measurements and, as ID24, it has a proper laser heating setup used for extreme conditions measurements. Samples are pressurized in a diamond anvil cell and two Nd:YAG lasers (120 W) are focused on the sample to achieve high temperatures (1.27(a)). Schwarzschild type microscope objectives are used to collect Black Body radiation and for sample imaging. A beam splitter in front of the spectrometer is used to visualize (with a CCD) sample images reflected at the spectrometer entrance (1.27(b)). The pinhole size imaged on the sample is about  $5\ \mu\text{m}$ .

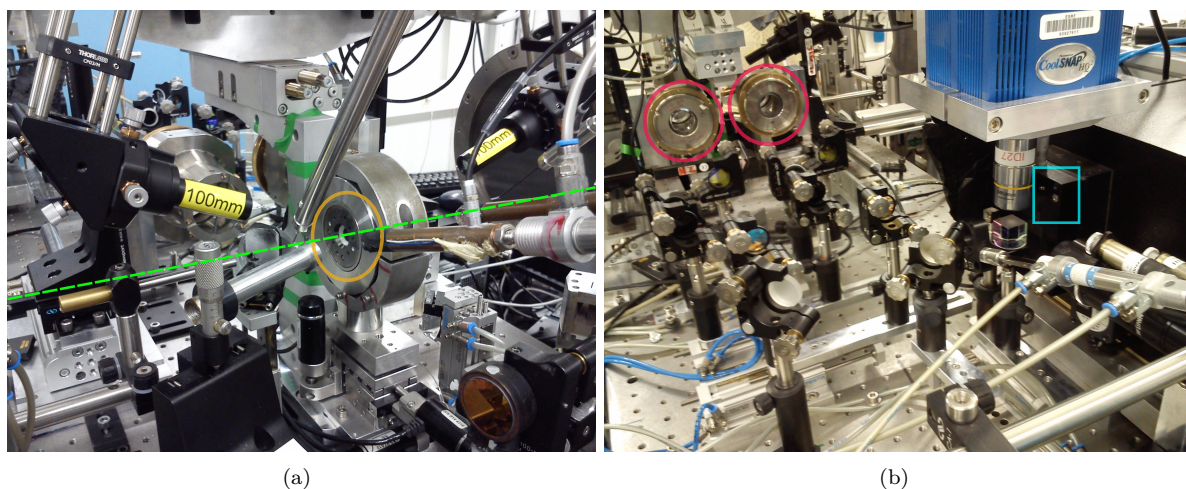


Figure 1.27: Panel (a): detail of ID27 laser heating setup; laser focus lenses are clearly visible (100 mm focal lenses). The diamond anvil cell is kept in the holder marked with an orange circle. The X-ray path is sketched with a green dashed line. Panel (b): back part of the ID27 setup. Light is collected by Schwarzschild optics (red circles) and brought to the spectrometer entrance (light blue rectangle). Measurements from the two sides of the cell are not done simultaneously, but mirror filters are rapidly flipped to look at both sample sides of the diamond anvil cell.

In Figure 1.28 is shown a simplified schematic of the ID27 laser heating setup. The sample crystalline structure can be obtained from diffraction spectra. The X-ray beam is less than  $3\ \mu\text{m}$  in size and each

diffraction pattern acquisition lasts from 5 s to 2 minutes. Measurements can be carried out in many ways and the sample can be continuously heated up to six hours. To perform these kind of measurements, great care should be paid in sample preparation: samples should be well insulated and unwanted thermal induced chemical contamination should be avoided; X-ray diffraction is sensitive to possible sample contamination, allowing to discard corrupted measurements. Pressure can be measured by X-rays using diffraction peaks from the sample or from the pressure medium if the equation of state of the sample is not known. It is also possible to measure pressure with a ruby [43] using X-ray excitation if necessary. This laser heating setup allows to measure with diffraction either powder and single crystal samples by rotating the cell with a precise goniometer with respect to the X-ray direction. When using powder samples, temperature can be measured simultaneously with the acquisition of diffraction spectra. For single crystals, simultaneous measurements are not possible and temperature is measured repeatedly many times between two diffraction spectra. In these kinds of measurements lasers are kept at the same power; if the temperature varies significantly between different measurement sequences and/or the hot spot is visually wobbling, then the acquired diffraction pattern is discarded and lasers are repositioned on the sample. Temperature cannot be measured simultaneously on both sides; anyway the temperature balance on the two sides is checked before the measurements by two mirrors that can be rapidly moved (5 sec) to bring the Black Body signal from both sides of the sample to the spectrometer pinhole. Once the sample is positioned into the cell holder in the experimental hutch, the experiments can be carried out remotely; the measurement accuracy is based on the stability and reproducibility of all the motors; in any case, the camera observing the sample allows a visual feedback and X-rays, optics and lasers can be realigned if necessary.

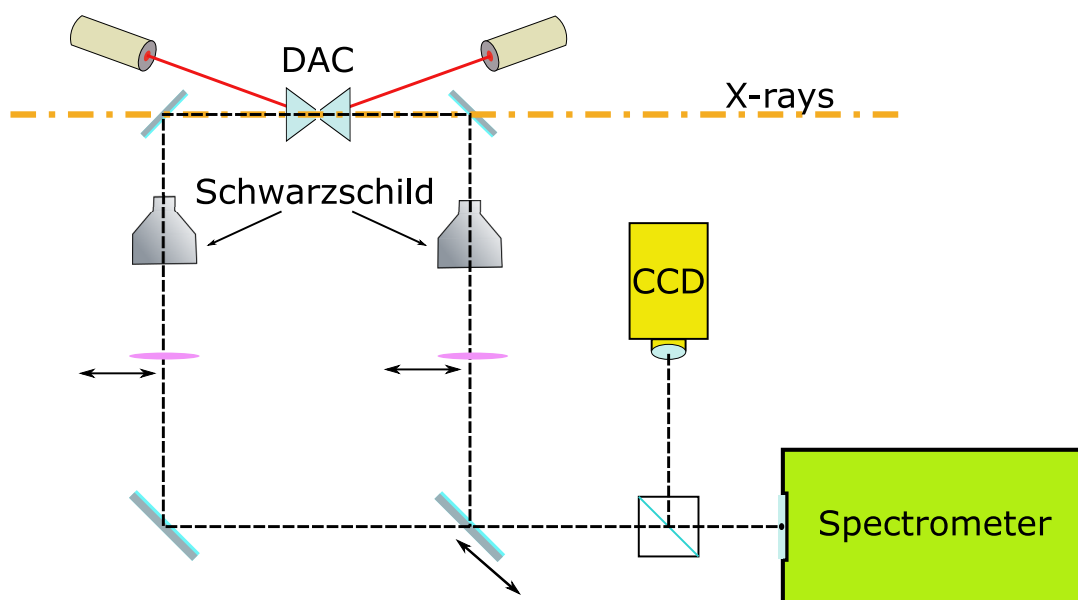


Figure 1.28: ID27 laser heating setup schematic.

## Chapter 2

# Experimental setup

### 2.1 General description

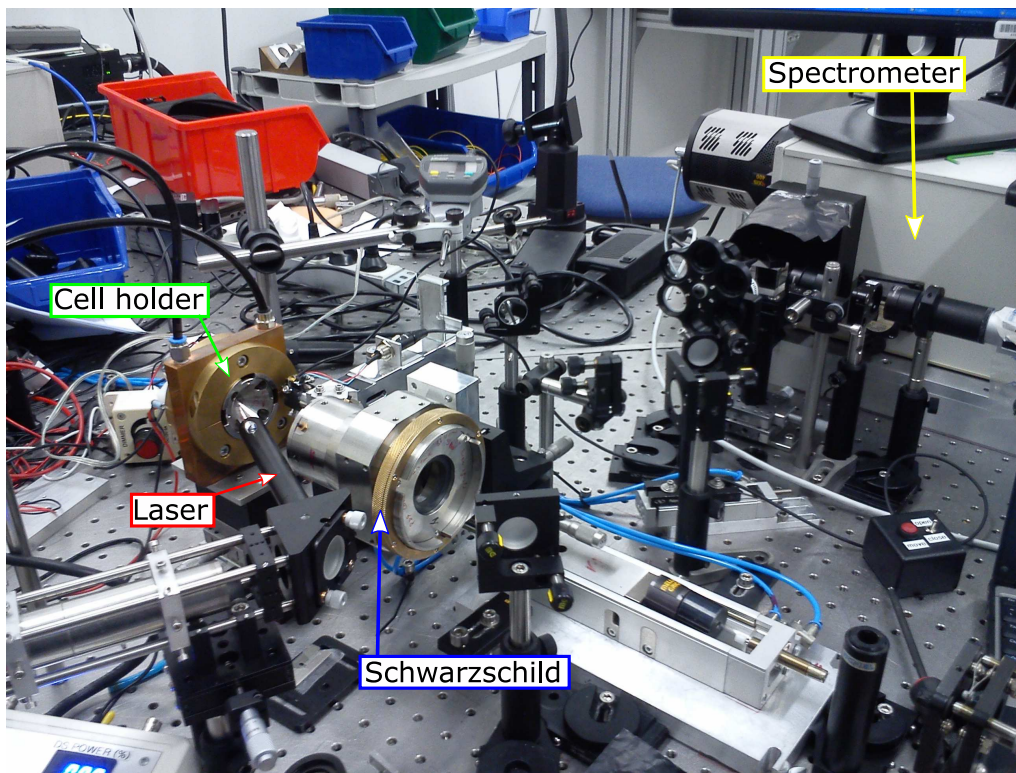
A dedicated setup has been mounted to directly compare the temperature measurements using lenses (with and without iris) and Schwarzschild optics (see Figure 2.1 Figure 2.2). This setup allows measuring the same hot spot with both optics: particular care has been taken for the alignment and measurement procedures to be sure not to introduce systematic errors in temperature measurements. The sample, held in a diamond anvil cell (DAC), is heated on one side and the temperature is measured either with Schwarzschild mirrors or lenses on the same side: this can be carried out by fast switching the two optics by means of pneumatic motors.

In Figure 2.2 the optical scheme is shown. Close to the cell location, each optics follows its own optical path to respect the specific focal distances. The two paths have been realized just by adding plane mirrors, so that there are no relevant distortions in the images. All the filters have been placed close to the spectrometer, when the two optical paths merge in one. Moreover each optics has its own intensity calibration on the spectrometer.

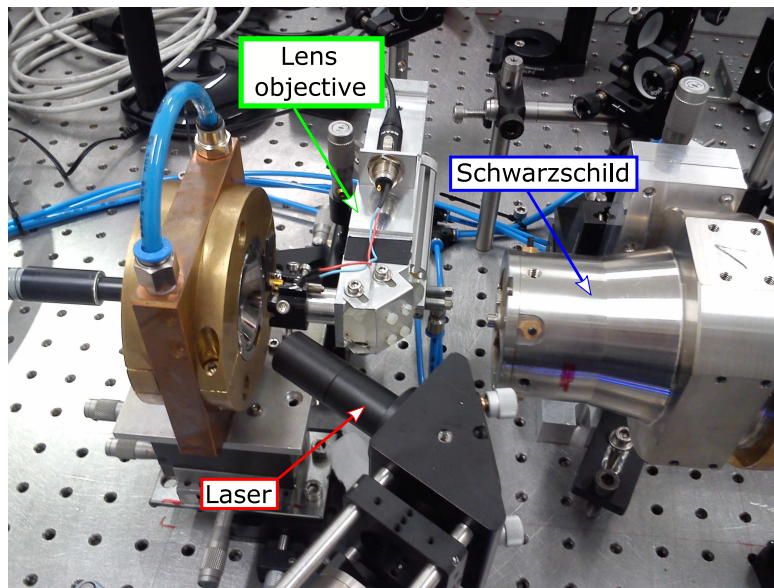
Before the spectrometer, in the setup there are three kind of filters: a long-pass filter to avoid unwanted harmonics generated by the spectrometer, a notch to filter the laser intensity that may reach the spectrometer entrance, and some neutral density filters with different optical density to lower the intensity integrated by the spectrometer in case of very high temperatures which can lead to saturation.

After the filters, the light collected by the optics goes directly into the spectrometer. The slit at the entrance of the spectrometer is replaced with a metallic mirror with one small (35  $\mu\text{m}$ ) hole so that the light is reflected back to a CCD camera through a beam splitter, to produce a image of the sample in DAC. An infrared filter is positioned just before the camera to get rid of all the infrared light that saturates the CCD.

The spectrometer we use is a Czerny-Turner type imaging spectrometer coupled with a PIXIS camera: 400B-EX, which is a back illuminated CCD specifically designed to have a low etaloning. The overall spectral resolution of the system, that is the smallest wavelength length that should separate two infinitely sharp peaks to be recognised, is about 1.2 nm. A shutter has been positioned directly in front of the spectrometer to reduce the read-out noise. The IR laser used for the heating is a fiber coupled Ytterbium laser which operates in the continuous mode. This laser generates a maximum power of 120 W at 1064 nm and has a purely Gaussian transverse mode  $\text{TEM}_{00}$  with beam quality factor  $M^2$  of 1.05. The laser beam hits the sample with an angle of about 30 degrees with respect to the optical axis of lenses and Schwarzschild, and it is focalized on the sample with a  $f = 750$  mm lens (treated with a proper antireflection coating) to have an hot spot of about 20-25  $\mu\text{m}$  FWHM (Full Width at Half Maximum). The whole system is very flexible since the laser spot, the optics and the cell can be moved independently. In this way, once the optics are aligned, it is possible to move the laser spot on the sample without further realignments of the optics. The cell is water-cooled to avoid instabilities due to the heating of the cell holder while measuring.



(a)



(b)

Figure 2.1: Top panel: picture of the setup. Bottom panel: zoom over the cell area.

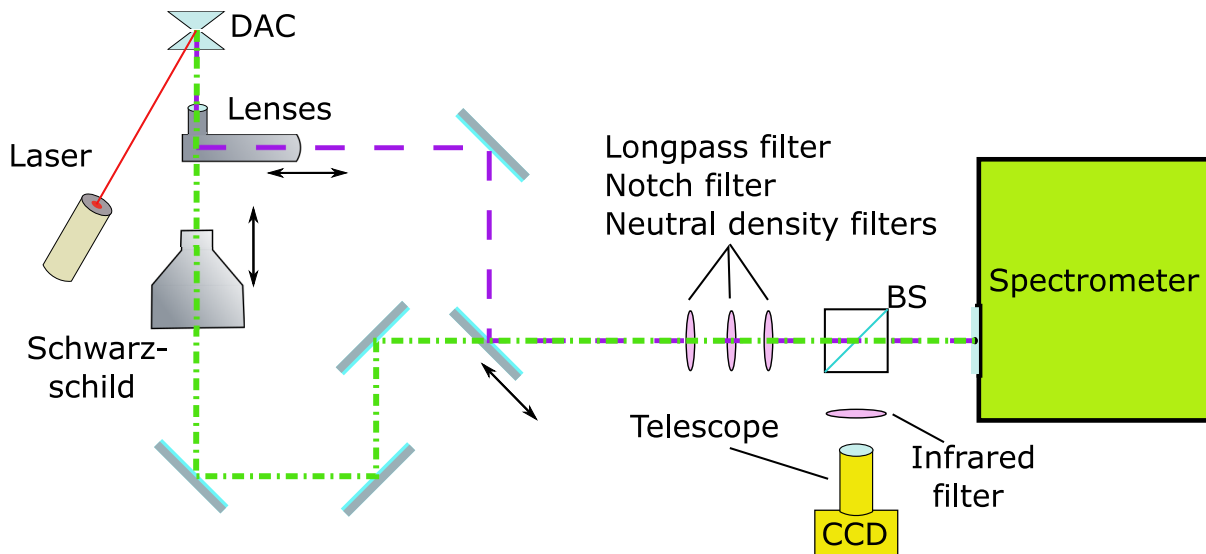


Figure 2.2: Schematic drawing of the setup. Schwarzschild microscope and lenses can be moved by means of pneumatic actuators to allow a fast switch between the two optics. DAC is the diamond anvil cell and BS is beamsplitter.

## 2.2 Measurements

### 2.2.1 Calibration and fitting

The pyrometer calibration takes place in two different steps. In the first one each wavelength is associated to the correct horizontal position on the CCD; this is carried out using a Neon Lamp which has very sharp emission peaks in the spectral region of interest (570-900 nm). The latter is to calibrate the intensities: for this, we have used a tungsten calibration lamp with a big and flat surface whose temperature functional dependence on the applied current is known. This lamp was put in the sample position (Figure 2.3) and a spectrum for each possible combination of optics (lenses, reduced aperture lenses, and Schwarzschild) and filters (low pass, notch, grey filters), was acquired. We have also compared a common coil tungsten lamp pre-calibrated with the flat one: no differences were found in the measured temperatures. When measurements are performed, the acquired Black Body spectra are divided by the proper calibration spectrum and then they are fitted with the Planck Law for radiant intensity [1]:

$$I_{Planck}(\lambda) = \frac{I(\lambda)}{S(\lambda)} = \epsilon \frac{2\pi hc^2}{\lambda^5} \frac{1}{e^{\frac{hc}{\lambda kT}} - 1}$$

where  $S(\lambda)$  is the system response of the optical setup. The emissivity is assumed to be wavelength independent, however "as  $\epsilon$  is a multiplicative constant, it also encompasses any factor that modulates intensity such as contributing sample volume and exposure time" [39]. Only the  $\epsilon$  and  $T$  parameters are free to vary in the fit procedure. The sample emissivity is a wavelength dependent quantity, but in LHDAC experiments this dependence is generally considered to be negligible [8] and, therefore, we have assumed a grey body approximation. The calibration is finally double checked by switching the calibration lamp's current and checking measured temperatures with the different optics.

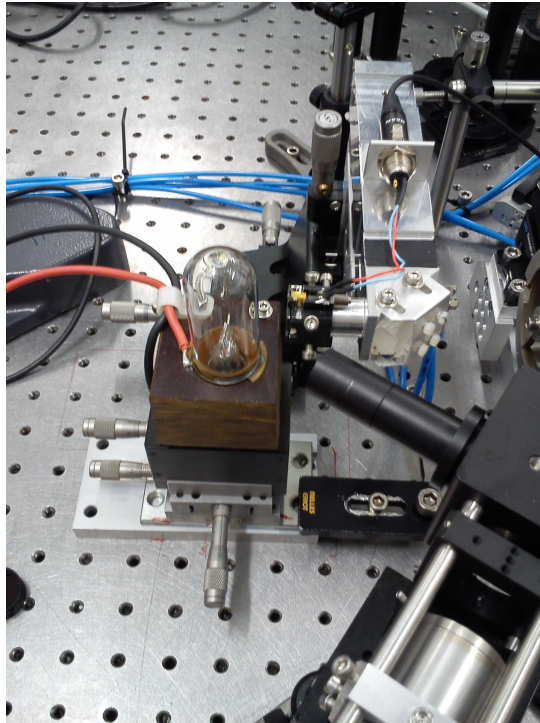


Figure 2.3: Temperature calibration using a tungsten lamp placed at the sample position.

## 2.2.2 Uncertainty analysis and temperature stability

The aim of this setup is to determine the relative accuracy of three different optics: full aperture lenses, lenses with iris, and Schwarzschild mirror. This has been carried out by comparing measured temperatures of the same hot spot with the different optics and by analysing the fit quality. Bad quality fits could be ascribed not only to the bias introduced by the optics, but also to the noise that is affecting the measurements. In other words, not only accuracy but also precision could be responsible for deviations from the Planck curve of the recorded spectra. Walter and Koga [1] have demonstrated that accuracy and precision are directly related when radial displacements (i.e. chromatic aberrations) are considered; however, this property can be applied only when the signal to noise ratio is constant and the same for all optics, which is not the case in these experiments. To get a deeper understanding of the magnitude of the precision influence on spectroradiometric temperature measurements, a brief noise analysis follows.

In fact, as it is shown in section 3.1, systematic errors in temperature measurements introduce some features in the Black Body spectra that could be analysed and interpreted. However, noise could conceal some of these features; therefore, a knowledge of the system precision is required. In Figure 2.4 typical Black Body spectra from which Planck's fit has been subtracted are shown.

The acquired Black Body spectra can be affected by systematic errors, stochastic errors, and other effects which are completely unrelated to Black Body emission but which could contribute to distort the measured spectrum, as it will be discussed in the following paragraph. Precision of temperature measurements is determined by either wavelength or intensity uncertainties. Wavelength uncertainty could be estimated considering a uniform probability density function over the single CCD pixel:  $\sigma_w = \delta/\sqrt{12}$ , where  $\delta$  (about 0.3 nm) is calculated as the ratio between the range of the spectrometer and the pixel number, which gives  $\sigma_w \approx 0.025$  nm. This error can be propagated to the intensities using the formula:

$$\sigma_{I_w} \simeq \left| \frac{dI}{dw} \right| \sigma_w$$

and a rough estimation of the error can be obtained by taking the maximum value of the first derivative be found in the Planck spectra: approximatively:  $\left| \frac{dI}{dw} \right| \approx 65 \text{ e}^-/\text{nm}$ . Therefore, an error of  $\sigma_{I_w} \approx 1.6 \text{ e}^-/\text{px}$  is found.

The most relevant intensity stochastic noises which are considered in a CCD are dark current noise, read out noise, and photon shot noise. Dark noise originates from the statistical fluctuation of thermally generated electrons within the pixel constituting the CCD; since we are cooling the CCD down to  $-75 \text{ }^\circ\text{C}$  this contribution is negligible. The read-out term includes all possible electronic noise sources related to the signal measurement on the CCD; considering the operating mode in which we are using our camera, the noise rms (root mean squared) is about  $10 \text{ e}^-$  per pixel.

Finally, the photon shot term arises when photons are detected: since in quantum mechanics the photons are absorbed with a certain probability, the number of actual photons absorbed fluctuates. Considering each photon absorption as an instantaneous and independent process, the process could be therefore represented by a Poisson distribution with a square root relationship between signal and noise. The mean value of intensities detected on each pixel is of the order of  $10^4 \text{ e}^-$ , so the standard deviation of the process is about  $10^2 \text{ e}^-/\text{px}$ .

Comparing the square of the standard deviation of all the above-mentioned noises, we see that the CCD is then really photon noise limited. Hence, we can roughly estimate that the signal to noise ratio (SNR) is around 100, which is compatible with the observed spectra. Moreover, a quasi-periodic signal, not related to Black Body emission, was observed superimposed to the Planck spectrum (Figure 2.4). This could be an interferometric signal due to the confinement of the sample within the pressure medium; this pressure medium (KCl in our case) is transparent at high pressure and, therefore, could be responsible for interferometric fringes. The wavelength distance between two peaks is not constant along the spectrum and is given by the following formula:

$$\Delta\lambda = \frac{\lambda_0^2}{2nd}$$

where  $\lambda_0$  is a given wavelength,  $n$  and  $d$  are respectively the refractive index and the thickness of the salt. To see if this quasi-periodic signal could really be an interferometric effect, the fit residuals have been fitted with the transmission equation of a Fabry-Pérot interferometer [44]:

$$T = \frac{1}{1 + F \sin^2\left(\frac{\delta}{2}\right)}, \quad \delta = \left(\frac{2\pi}{\lambda}\right) 2nd$$

Where  $F$  is the Finesse coefficient. The fit, shown in Figure 2.5, produced a value of  $n*d$  of few  $\mu\text{m}$  which, considering the strong approximations, is compatible with pressure medium thickness in a diamond anvil cell. The Finesse coefficient obtained is about 0.1.

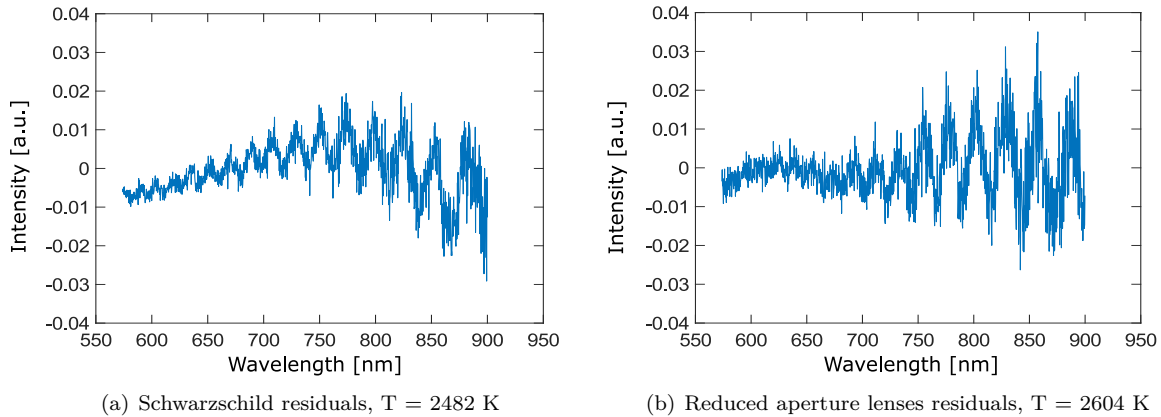


Figure 2.4: Raw spectra from which the fit has been subtracted either for Schwarzschild (2.4(a)) and for reduce aperture lenses (2.4(b)).

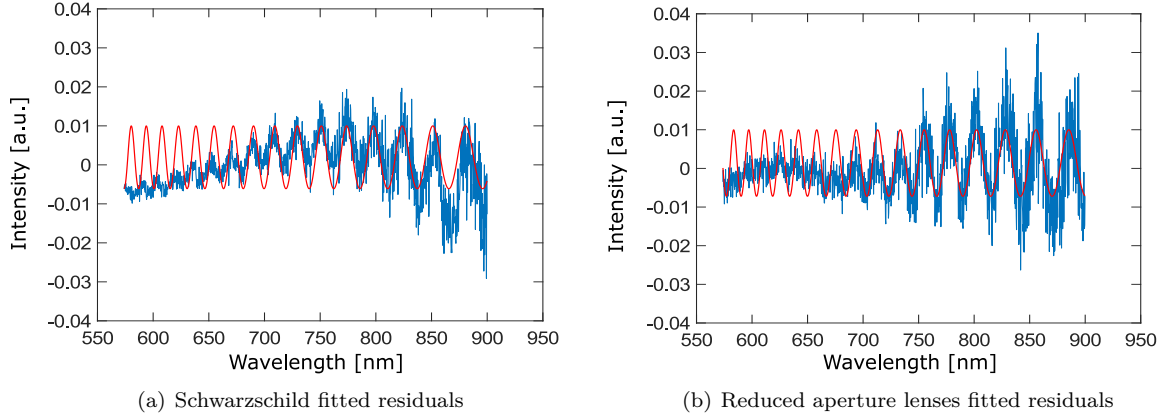


Figure 2.5: Schwarzschild (2.5(a)) and reduced aperture lenses (2.5(b)) noises fits to a Fabry-Pérot interferometer model.

In the end, all the uncertainties mentioned before contribute to give a temperature fit error (in a confidence interval of 95%) are within  $\pm 5$  K both with reduced aperture lenses and Schwarzschild objective. Hence, the systematic temperature differences that can be distinguished are larger.

To measure systematic errors properly it's necessary to be sure that the hot spot has not changed when switching the different optics. In our setup we can switch lenses and Schwarzschild rapidly (less than 5 s considering the waiting time to avoid optics drifts) but sometimes extra time (5-10 s) is required to correct the position of the optics. Several time stability measurements have been performed to observe the dynamic of sample temperature. The sample has been heated and its temperature has been measured continuously. Some examples of these measurements are shown in Figure 2.6 and Figure 2.7. Over time, the temperature decreases for several minutes until an equilibrium is reached. This behaviour has been observed both with Schwarzschild and with lenses. The temperature difference and the time required to reach the equilibrium depend on the sample and cell conditions but the magnitude of the phenomenon is always about a hundred Kelvin over hundreds seconds.

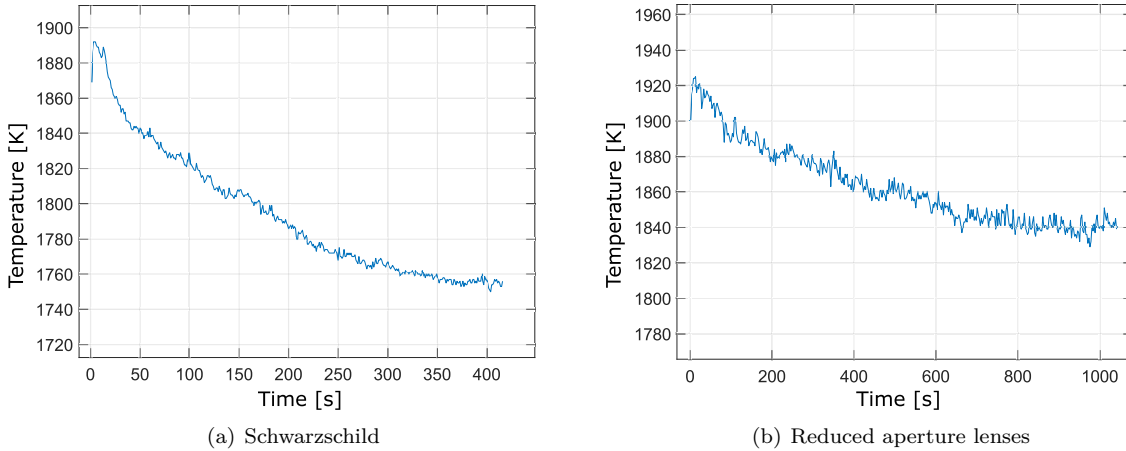


Figure 2.6: Time stability measurement for Schwarzschild (1 s exposure time, panel a) and reduced aperture lenses (2.5 s exposure time, panel b). The measurements have been performed by heating continuously a W sample in a DAC, embedded in KCl as pressure, with the Ytterbium laser. The temperature acquisition is synchronized to the laser switching on.

When the temperature is stabilized, the remaining temperature fluctuations have a zero mean and a standard deviation of a few Kelvin (Figure 2.7).

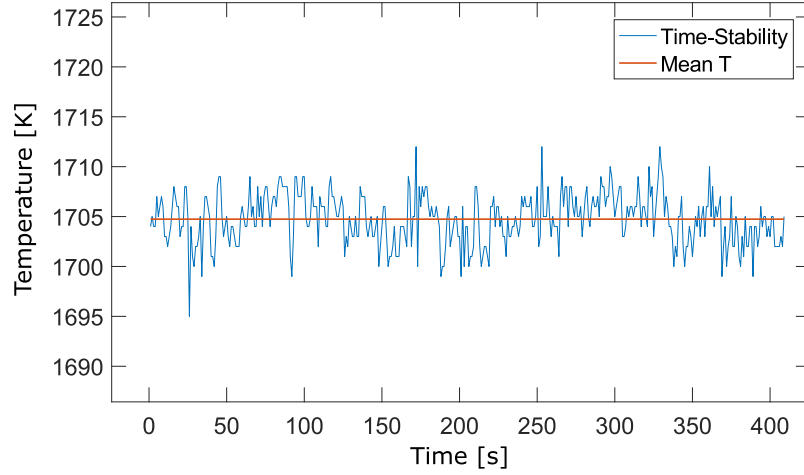


Figure 2.7: Time stability measurement performed with reduced aperture lenses (2.5 s exposure time) after letting the sample stabilize several minutes. When temperature is stable, the standard deviation has a value of few Kelvin.

### 2.2.3 Measurement procedure

In this section the procedure followed to collect data is presented. The first step, after performing the calibration, is to put the sample in the Schwarzschild and lenses focal point; this could be performed using the camera that, through the beam splitter, looks directly at the pinhole on the spectrometer. A bright light behind the sample has been used to see the sample on the camera. The pneumatic motors allow switching the optics in and back to almost in the same position, making the focal adjustment quite fast.

At the outset, the laser is turned on (at low power), positioned and focused on the sample; the centre of the hot spot is then hence aligned with the spectrometer pinhole with both optics. By moving the sample along the focal plane, it is possible to take the hot spot in different sample positions without moving the optics or the laser which remain therefore aligned and focused. As explained in the previous section, having a stable hot spot is of a great importance for the measurements we have performed. After everything is aligned and focused we start heating the sample with laser at low power to let the hot spot stabilize and, thus, avoiding great temperature drifts. The hot spot should look stable and homogeneous. In Figure 2.8 different hot spots observed with reduced aperture lenses and with Schwarzschild are shown. Using the CCD is possible to see by eye micrometric features in the visible part of the spectrum and in the near infrared one and appreciate thermal dynamics up to 20 Hz. Sometimes the hot spot showed a deformed and inhomogeneous shape (2.8(c), 2.8(d)) likely because of imperfections of the sample surface or of the optics. In this case the optics was checked or a different sample position was chosen. Most importantly the hot spot should be reasonably big in order to reduce temperature gradients that could degrade temperature measurements (2.8(a), 2.8(b)).

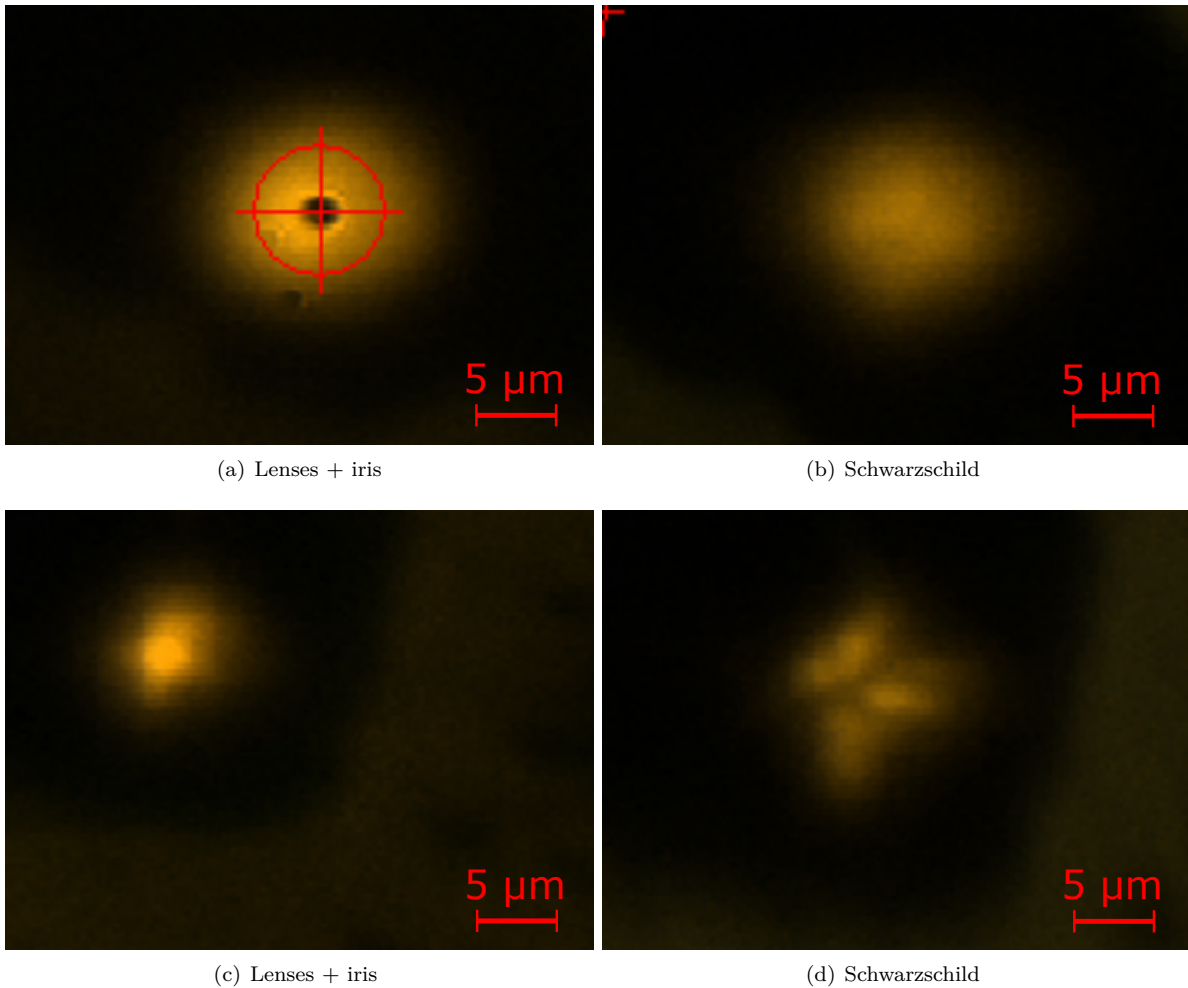


Figure 2.8: Spot images. (a),(b): hot spot of measured temperatures. (c),(d): not acceptable. The red viewfinder in picture (a) has been used during experiments for an accurate alignment of the pinhole with the hot spot.

Using the CCD it is possible to see by eye micrometric features in the visible part of the spectrum and in the near infrared one and appreciate thermal dynamics up to 20 Hz. Data have been collected only when the spot is rounded shaped and stable (2.8(a), 2.8(b)). The temperature stability has been then double checked measuring the hot spot at the same laser power many times with the same optic.

## 2.2.4 Resolution measurements

In this section, some resolution measurements of reduced aperture lenses and Schwarzschild are presented ( Figure 2.9 and Figure 2.10 respectively). These measurements have been carried out directly on the beamlines by I. Kantor on ID24 and by I. Kantor and G. Garbarino on ID27. Resolutions are obtained by scanning the edge of a large optical fiber along the focal plane with sub-micron step, thus collecting a spectrum in each position. For each wavelength, the profile obtained is then derived: the resulting signal is Gaussian like and its FWHM is indicative of the resolution of the system. The obtained FWHM has then been plotted as a function of wavelength. Further details will be given in an article in preparation [5]. From Figure 2.9 it is possible to observe that from 650nm the reduced aperture lenses system is diffraction limited and the chromatic aberrations are negligible. Schwarzschild resolution is shown in Figure 2.10. From the figure it is possible to appreciate that Schwarzschild resolution is flat in a wide range but quite sensitive to the focal distance.

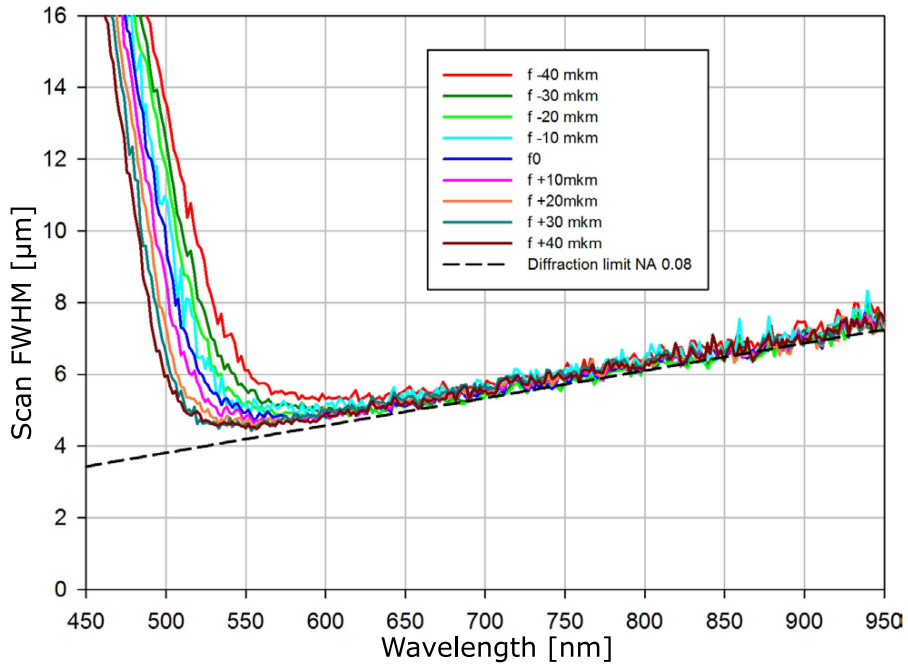


Figure 2.9: Reduced aperture lenses resolution measured on ID24 for different focal distances. From [5].

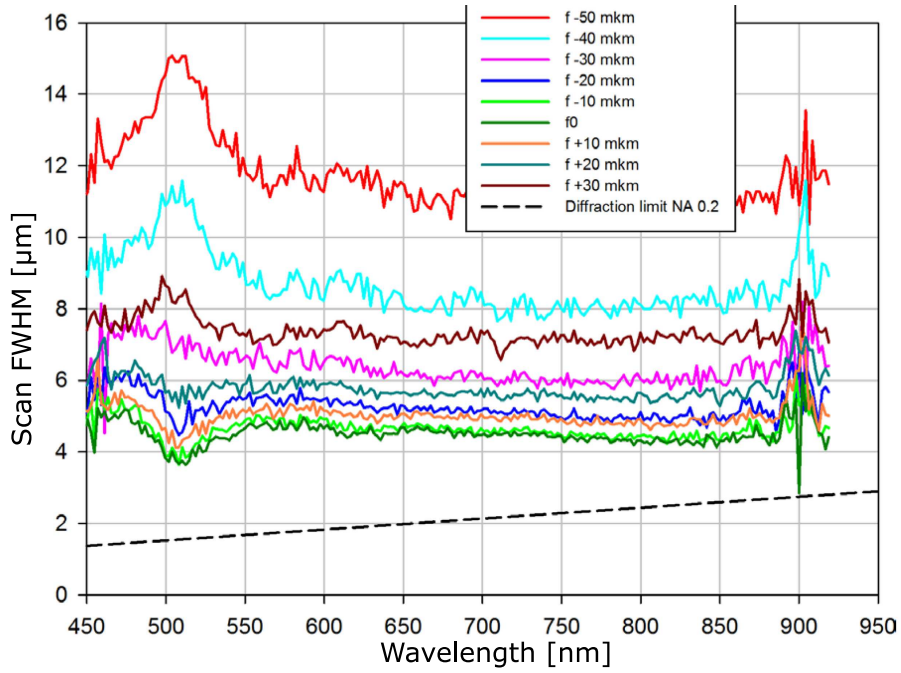


Figure 2.10: Schwarzschild resolution measurements taken on ID27 [I. Kantor, G. Garbarino].

# Chapter 3

## Results and discussion

### 3.1 Theoretical results

This chapter is going to present theoretical calculations done to achieve a wider comprehension of the phenomena which have been investigated in the laboratory. Many numerical simulations regarding the effect of chromatic dispersion on temperature measurements have been carried out by several authors [39] [1]. Here, to understand how limited resolution affects temperature measurements and how these effects can be revealed in Planck fit and two-colour plots, simple simulations concerning achromatic lossless optical systems are proposed.

As explain in chapter 1, in spectroradiometric temperature measurements the sample hot spot is imaged and magnified by an optical system (based either on mirrors or lenses) on the spectrometer entrance. Then, a small portion of the hot spot (usually the area at the highest temperature) is sampled by the spectrometer pinhole. Both optics imaging and pinhole sampling can be source of errors in temperature measurements since they allow not only the light coming from the very top of the hot spot but also light from the surrounding area to enter in the spectrometer. In these simulations, both effects have been considered.

The imaging process has been modelled considering the point spread function (PSF) of the optical system. The PSF concept is based on the picture of light propagation within linear system theory. When considering a linear, homogeneous, isotropic non-dispersive medium, the propagation of the electromagnetic field follows the simplified D'Alembert's equation [45]:

$$\nabla^2 E - \frac{1}{c^2} \frac{\partial^2 E}{\partial t^2} = 0$$

where  $c$  is the light speed and  $E$  is the modulus of the electric field (the same equation describes the propagation of the magnetic field).

In this case the scalar diffraction theory can be used [45]: electric and magnetic fields propagate independently and there is no cross talk between their components. It is important, however, to point out that even in a homogeneous medium, boundary conditions could couple electric and magnetic fields as well as their scalar components, entailing some degrees of error. However, in case of diffraction by an aperture, errors are negligible if the aperture is larger than the wavelength. This occurs in most of the microscopes in the visible range, so it is possible to consider the propagation phenomenon as a linear spatial filter: the linearity in the field amplitude directly comes from the linearity of the wave equation and the optical system can therefore be described with a space-invariant transfer function [45] [46]. "Thus, in this general case, for a diffraction limited system we can regard the image as being the convolution of the image predicted by geometrical optics with an impulse response that is the Fraunhofer diffraction pattern of the exit pupil" [45].

The impulse response of an optical system is called point spread function; the electric field on the image plane  $E(x,y,z)$  can then be obtained from the electric field on the object plane  $E(x,y,0)$  as:

$$E(x, y, z, \lambda) = PSF(x, y, z, \lambda) * E(x, y, 0, \lambda)$$

or, equivalently, in the spatial frequency domain:

$$\tilde{E}(k_x, k_y, z, \lambda) = OTF(k_x, k_y, z, \lambda)\tilde{E}(k_x, k_y, 0, \lambda)$$

where OTF (optical transfer function) is the 2D Fourier transform of the point spread function. The PSF (and the OTF as well) are generally wavelength dependent: as it will be shown later in this chapter, this is one of the causes of distortions in the measured Black Body spectra. Within the paraxial approximation, the intensity PSF of a cylindrically symmetric optical system is an Airy disk (see subsection 1.3.3).

D'Alembert's equation shows that, when light sources are coherent, light propagation is linear in the electromagnetic field; this means that the image intensity (squared absolute value of the field) is not linearly propagating. However, when the source is incoherent, the phase relation among the plane waves constituting the light Fourier spectrum is lost: the PSF is not a perfect Airy disk anymore, but the intensity propagation can be studied within the linear system theory. This is the case for the Black Body source, which, as explained in the introduction, can be treated as incoherent in the far-field [28] [47].

We have performed our simulations considering a 2D Gaussian intensity PSF: within this approximation, the Rayleigh resolution criterion gives directly the full width at half maximum of the Gaussian PSF (see subsection 1.3.3). The top intensity is calculated assuming a constant transmission coefficient over all the wavelengths: being the area below the intensity profile the energy per unit time emitted by the source, if the energy is conserved then the integral of intensity profiles on the image plane and the one on the object plane have to be the same. Since there is no cross talk among different frequencies, this has to be true for each wavelength. The area of the image intensity profile is related with the one on the object plane by the well know relation [48]:

$$\begin{aligned} \int \int_{-\infty}^{+\infty} E(x, y, z, \lambda) dx dy &= \int \int_{-\infty}^{+\infty} PSF(x, y, z, \lambda) * E(x, y, 0, \lambda) dx dy = \\ &= \int \int_{-\infty}^{+\infty} PSF(x, y, z, \lambda) dx dy \int \int_{-\infty}^{+\infty} E(x, y, 0, \lambda) dx dy \end{aligned}$$

Since the PSF can have, in principle, whatever FWHM, this means that the integral of the point spread function should be normalized for all the wavelengths. This gives easily the height of the Gaussian bell representing the PSF in this model.

Several resolutions have been assumed and the wavelength dependent PSF have been thus calculated using the software Matlab. Here four cases are presented: two constant resolution PSF and two diffraction limited resolutions with different numerical aperture: these have been chosen as the theoretical numerical apertures of Schwarzschild (0.18), which is also close to the one of full aperture lenses (0.2), and reduced aperture ones (0.065).

The simulations have been carried out by firstly generating a temperature profile on the object plane (sample position). The temperature profile shown here has been taken as Gaussian with peak temperature of 3300 K and a full width at half maximum of 20  $\mu\text{m}$ : these values agree with common experimental ones. In each position, radiation is emitted in a way proportional to the temperature according to the Black Body Planck's law: therefore, each wavelength has its own profile on the sample. Hence, each profile is convoluted with the respective PSF obtaining the wavelength dependent intensity profiles on the image plane (Figure 3.1).

The importance of these simulations lies in the fact that, since no noise has been added, these could really give the possibility to get an insight into the inaccuracy effects of an ideal optical system and, therefore, help to compare different real optics temperature measurements. So, considering all the approximations that have been made, these simulations are meant mainly as qualitative guide to interpret experimental results rather than a quantitative analysis of them. Once the convoluted intensity profiles have been obtained, the top of this curve is sampled with a pinhole: finally, the resulting spectrum is fitted to the Planck's law using the Grey Body approximation and considering a wavelength independent empirical emittance coefficient.

The first result that has been obtained is that the current pinhole used for the experiments carried out in this work (about 2  $\mu\text{m}$  when demagnified on the object plane) does not introduce significant distortions in temperature measurements (about few degrees in the worst case).

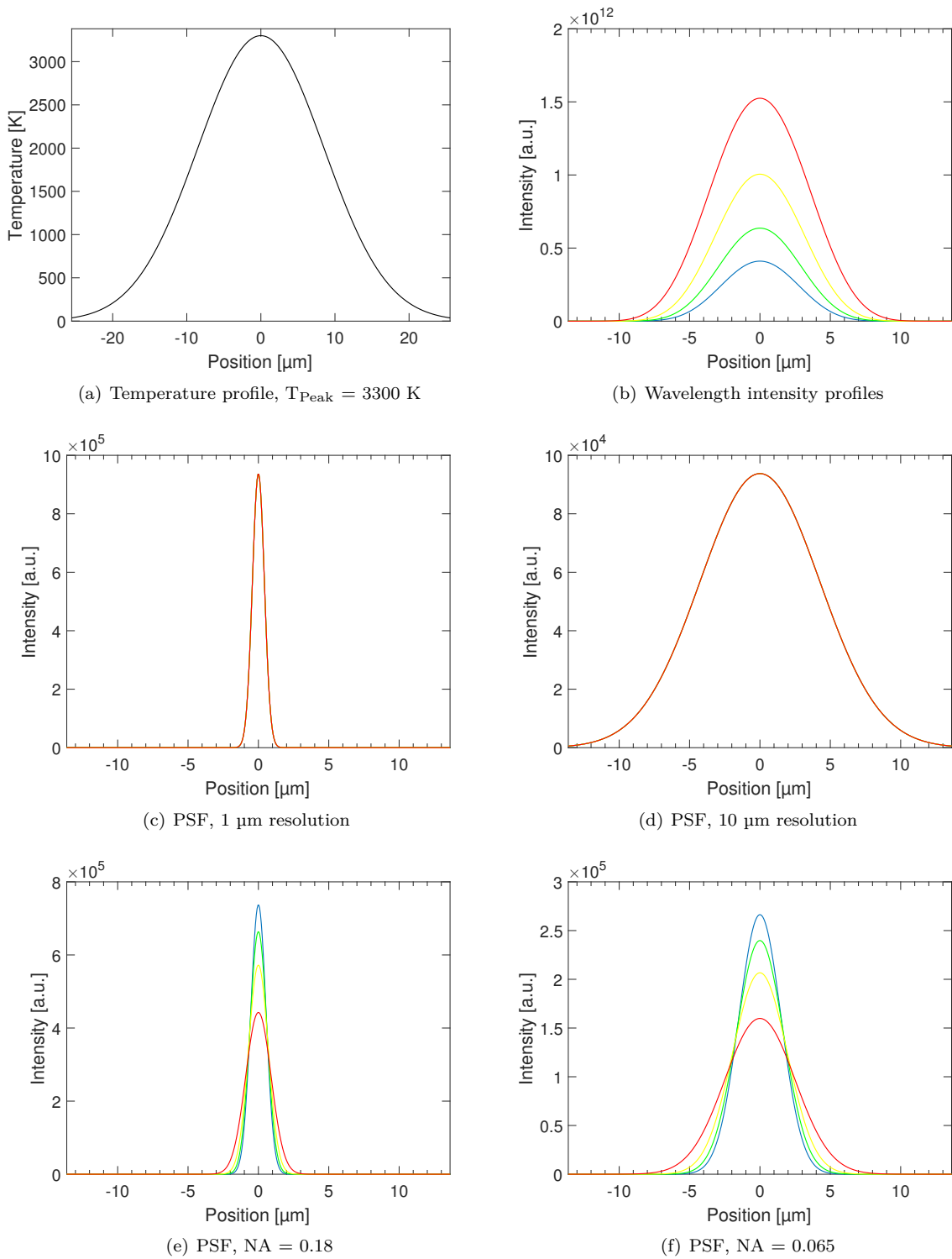


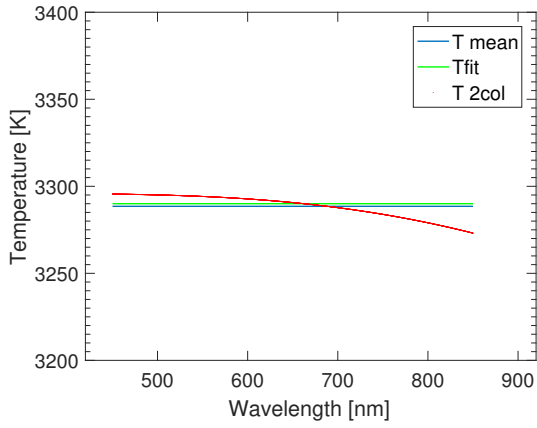
Figure 3.1: a) Gaussian Temperature profile; b) Black Body profiles at four different wavelengths. c), d) PSF respectively of  $1 \mu\text{m}$  and  $10 \mu\text{m}$ . e), f) PSF at four different wavelengths for a diffraction limited optical system with numerical aperture of 0.18 and 0.065.

In Figure 3.2 and Figure 3.3 Planck and two-colour fits of the different resolutions are presented.

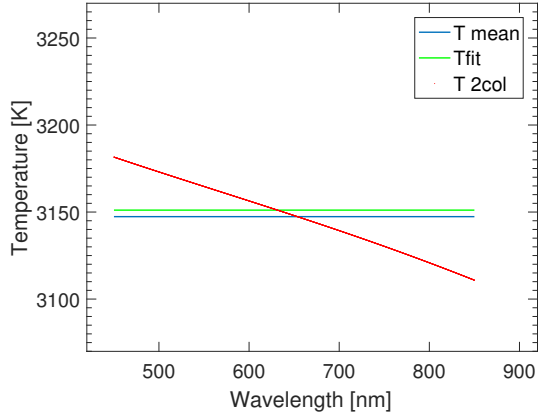
While Planck fit matches the convoluted spectrum, the two-colour fit shows wavelength deviations and the temperature measured is not the real one: 3150 K instead of 3300 K with a resolution of 10  $\mu\text{m}$ . When looking at the simulated two-colour fits of the constant finite resolution optical systems, an important feature emerges: even with a constant resolution the two-colour fit shows a wavelength dependent behaviour and, in particular, a negative slope. This feature can be ascribed to the fact that, since the temperature profile is Gaussian and not flat, the temperature profiles of each wavelength differ from each other; hence, even if the PSF is the same, each wavelength intensity is imaged, by the optical system, in a different way. Many temperature profiles have been generated with different peak temperatures and FWHM: constant resolution gives always lower temperatures and implies a negative slope in the two-colour fit.

The other factor that could contribute to a distorted two-colour plot and, therefore, to a less reliable temperature measurement is wavelength dependent resolution. This effect could be due either to the diffraction limit or to chromatic aberrations (or both). In 3.3(b) it is possible to appreciate the effect of a diffraction limited resolution system on temperature measurements: the two-colour fit is bent upwards and the calculated temperature is 91 K higher than the real one.

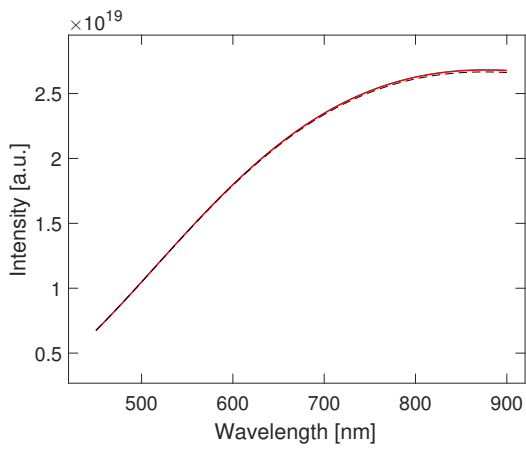
With a higher numerical aperture (3.3(a)) the slope of the resolution curve is smaller and, therefore, the effect of a wavelength dependent resolution on temperature measurement is less important. In Figure 3.4 the two-colour of the diffraction limited system with  $\text{NA} = 0.18$  is shown in a different scale: the peculiar shape of this plot can be interpreted as a compensation between the two effects mentioned before: the finite resolution imaging a temperature profile tends to bend the two-colour downward whereas the effect of the diffraction limited resolution is to move it upwards; these “forces” are rather balanced and the curve is almost straight. The calculated temperature is very close to the real one: 3310 K.



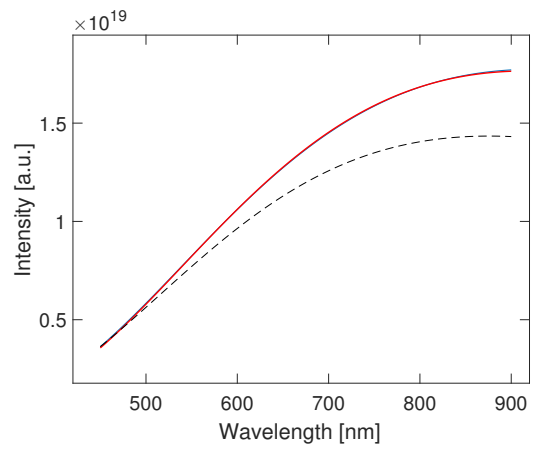
(a) Two-colour plot, 1  $\mu\text{m}$  constant resolution



(b) Two-colour plot, 10  $\mu\text{m}$  constant resolution

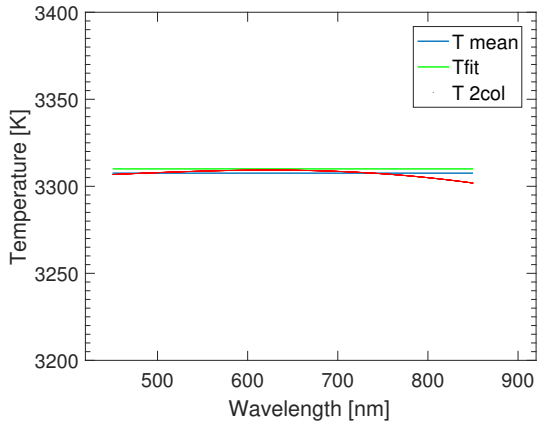


(c) Planck fit, 1  $\mu\text{m}$  resolution

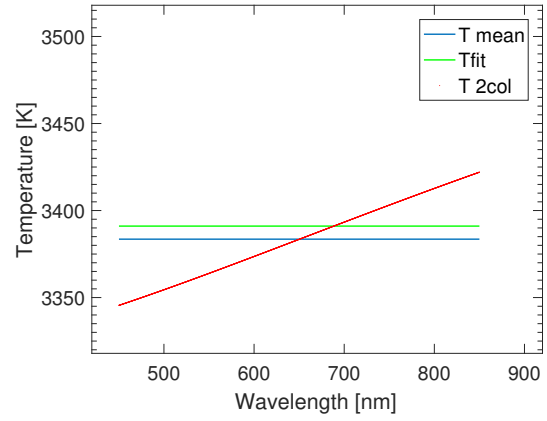


(d) Planck fit, 10  $\mu\text{m}$  resolution

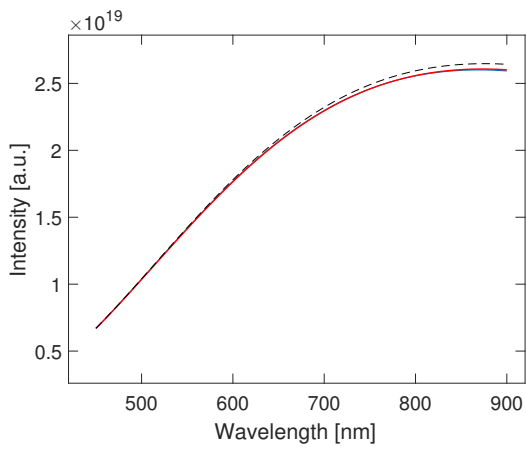
Figure 3.2: Two-colour and Planck fits of the spectra obtained with two different resolutions: a), c) are the plots related to 1  $\mu\text{m}$  resolution whereas b), d) are related to 10  $\mu\text{m}$  resolution. The temperature measured with the two different resolutions are respectively: 3296 K and 3150 K. The dashed line in the Planck fit is the ideal spectrum obtained with an infinite resolution optical system ( $T = 3300$  K). In the two-colour fit the red line represents the temperature of the fit. T mean (blue line) is the average of the two-colour fit temperatures. The green line in the same plots is the temperature obtained from the Planck fit.



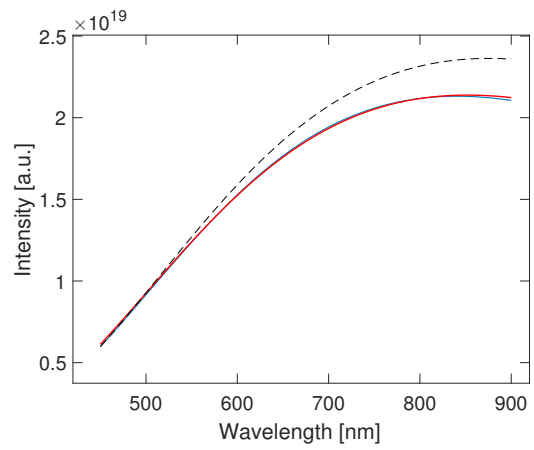
(a) Two-colour plot, NA = 0.18



(b) Two-colour plot, NA = 0.065



(c) Planck fit, NA = 0.18



(d) Planck fit, NA = 0.065

Figure 3.3: Two-colour and Planck fits of a diffraction limited resolution system are here presented; a), c) are related to an optical system with numerical aperture of 0.18 whereas b) and d) are those obtained with a numerical aperture of 0.065. The temperature obtained are, respectively, 3310 K and 3391 K.

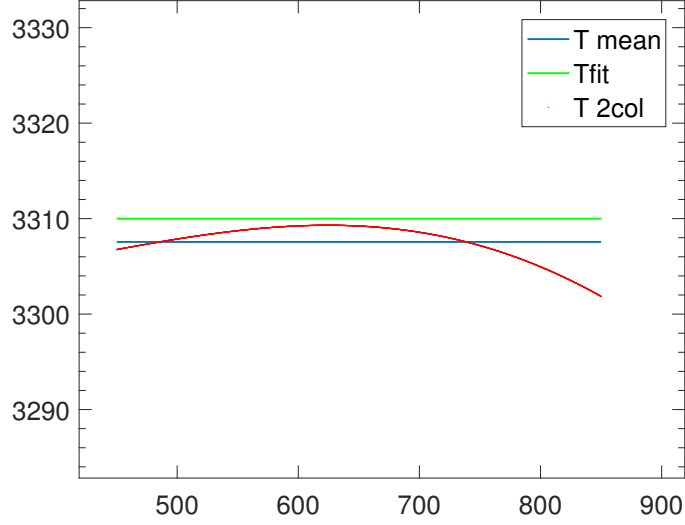


Figure 3.4: Two-colour plot for  $NA = 0.18$

Similar results have been obtained by adding Gaussian white noise to the Planck curve. As an example, two-colour plot and Planck fits of the  $10\ \mu\text{m}$  resolution system are shown in the Figure 3.5; as mentioned in the experimental setup, the precision of the experimental setup is such that it does not entail any relevant errors in the measurement: temperature measured with and without noise are close to each other (one degree difference). Noise partially hides the trend of the two-colour plot, making difficult recognizing the wavelength behaviour. It is therefore likely that, in real temperature measurements, errors of about one hundred degrees (at  $T \approx 3000\ \text{K}$ ) can be hidden. These errors could also happen in a perfectly achromatic optical system. In 3.5(c) the two-colour histogram is shown: as mentioned in the introduction, the Gaussian distribution of the noise in the Planck spectrum is propagated to the two-colour histogram. In this case the histogram does not show any aberration that could be interpreted as an error in temperature measurement: even if the histogram is Gaussian shaped and the Planck temperature and the average two-colour temperatures coincide, there is a  $150\ \text{K}$  accuracy error, which is far larger than the two-colour standard deviation ( $\approx 40\ \text{K}$ ). Therefore, considering the two-colour standard deviation as error bar [39] would, in this case, underestimate the error of temperature measurements.

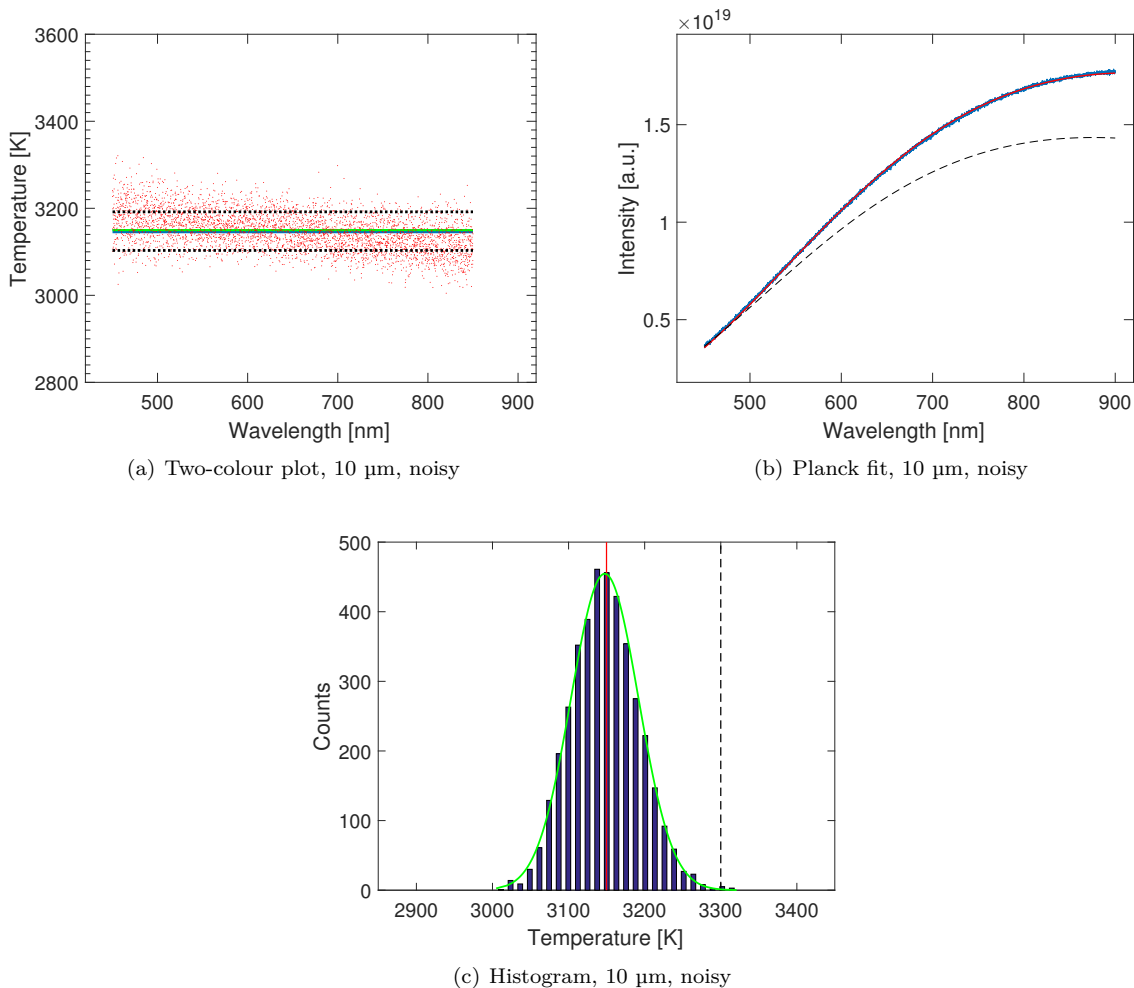


Figure 3.5: Two-colour plot, Planck fit, and two-colour histogram related to the 10  $\mu\text{m}$  constant resolution optical system. Simulations have been performed like in the previous examples, but gaussian white noise has been added in the Black Body spectrum before fitting it. The measured temperature is 3150 K. Dashed lines in the two-colour plot represent the 68% confidence interval of the two-colour temperature distribution. The blue line is the average of the two-colour temperatures while the green line is the temperature obtained from the Planck fit. The dashed vertical line in the histogram shows the real temperature on the hot spot; the red one is the average of the two-colour temperatures.

## 3.2 Experimental results

### 3.2.1 Preliminary results

Many temperature runs have been carried out on tungsten samples using KCl as pressure medium; the choice of tungsten is motivated by its very high melting point [49] [50] so that the sample can be kept in a stable condition while measuring temperatures with both optics. KCl is often used in LHDAC experiments because it's transparent and it has a very steep melting curve [51]. Temperature runs have been performed at 30, 60, 80 GPa with the methodology described in subsection 2.2.3.

It's important to state once again that the setup used can tell the difference between the temperatures measured with the two optics because both optics are looking at the same side of the sample, therefore they are not affected by any difference in the KCl layer thickness. Figure 3.6 shows normalized

Black Body spectra fits acquired at low temperatures with the Schwarzschild objective (3.6(a)), reduced aperture lenses (3.6(b)), lenses (3.6(c)) and lenses with a smaller wavelength window (3.6(d)). The errors shown in the figure are purely fit errors. The fit quality clearly shows that the temperature measured with lenses without iris is unreliable: as it has been shown in subsection 1.3.3, this could be ascribed to chromatic aberrations. Similar runs have been performed using different lenses (of the same type) obtaining qualitatively the same result; so the poor fit quality does not depend on lens quality.

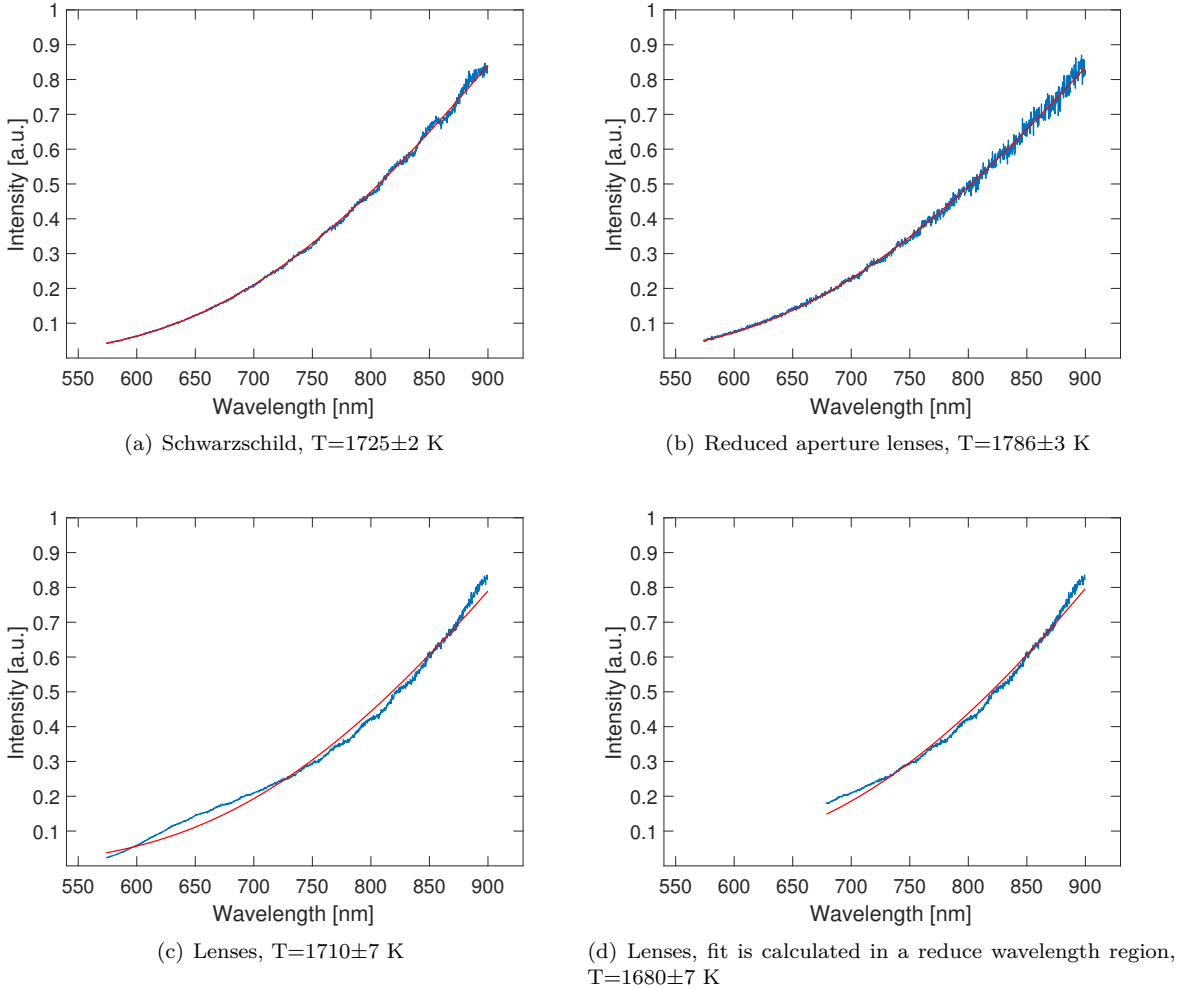


Figure 3.6: Normalized Planck spectra and fits of the same hot spot collected with different optical systems. The errors shown in the figure are purely fit errors.

In Figure 3.7 a direct comparison between temperatures measured with Schwarzschild and the ones measured with reduced aperture lenses is shown. Full aperture lens temperatures are not reported here because, as it has been shown above, those temperatures are not reliable. Moreover, on ID24 temperatures are always measured using iris.

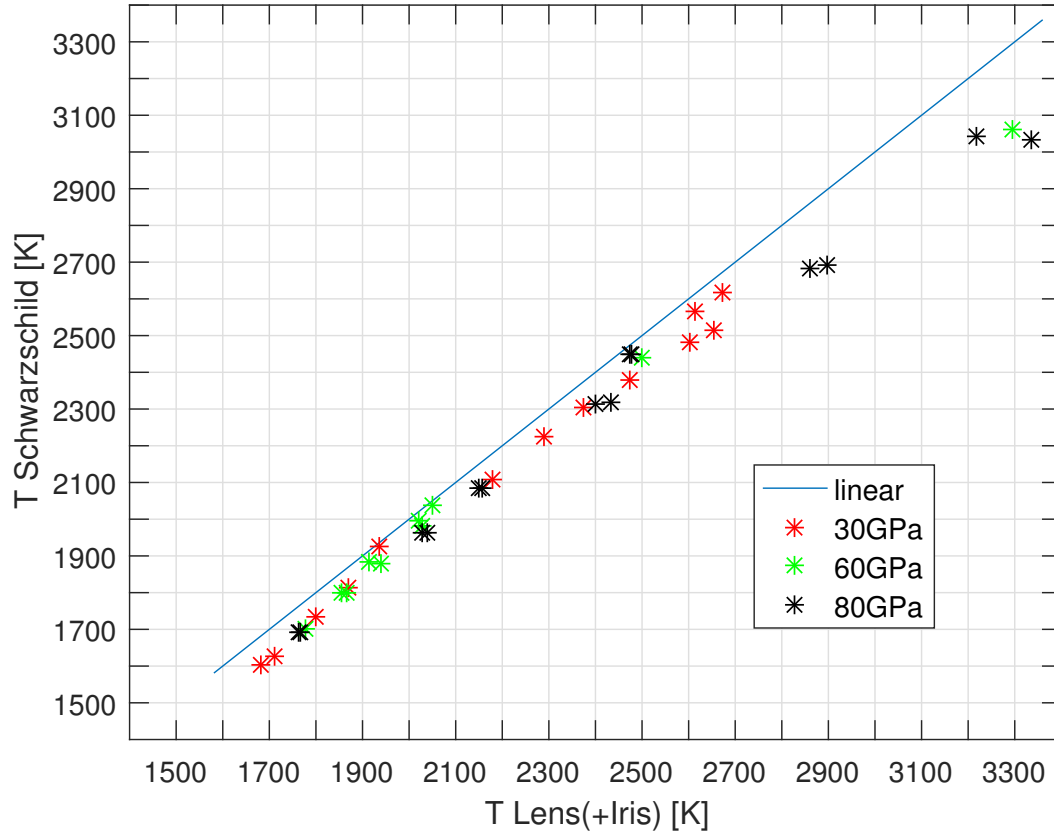


Figure 3.7: Measurements of the same temperatures with Schwarzschild and with reduce aperture lenses (iris); the blue line indicates a linear trend. Measurements have been carried out as shown in chapter 2. Data at three different pressure are shown.

The plot shows that the pressure does not affect the temperature measurements since consistent results are found at 30, 60 and 80 GPa.

At low temperatures, there is a steady temperature difference between the two optics of about 50K: Schwarzschild optics always measures a lower temperature while lenses measure a higher temperature. At high temperatures (above 2700K) the temperature difference grows monotonically up to above 200K. Indeed there are systematic and reproducible errors in the temperature measurements.

In Figure 3.8 the same results are represented in a more convenient way, clearly showing an increasing temperature difference trend as a function of temperature.

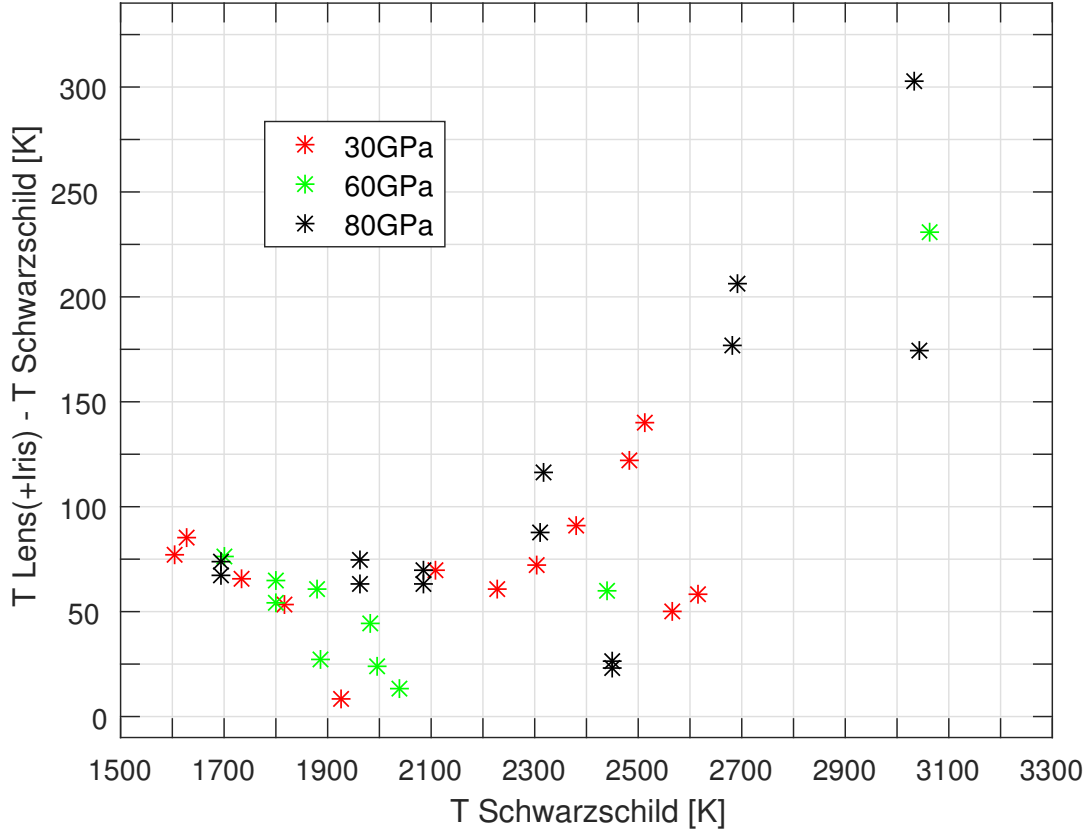


Figure 3.8: Temperature difference plotted vs measured temperature with Schwarzschild optics at three different pressures.

### 3.2.2 Fit analysis and discussion

The aim of this session is to evaluate the fit quality obtained using the two systems, in order to compare their accuracy. It is important to point out that this evaluation could not simply be handled just by using a quality fit parameter like the Chi Squared for instance. This because the noise and therefore the signal to noise ratio is not the same for the two optics (Schwarzschild and lenses), thus affecting the fit quality.

As explained in subsection 1.3.2, an efficient way to monitor the temperature measurements accuracy is the sliding two-colour pyrometry [39] [8]. This technique helps recognizing wavelength deviations from the ideal Planck distribution. Sliding two-colour pyrometry consist essentially in calculating the temperature using the Wien approximation: since a linear relation can be found, only two wavelengths are needed. Once the window width  $\delta$  between the two different wavelengths has been chosen, the temperature is calculated many times sliding the window over the entire spectrum.

For each possible window, mean and standard deviation of the sliding two-colour temperature are calculated. The window width should be taken small enough to observe a wavelength variation in two-colour temperature but large enough to avoid the strong effect of noise (Figure 3.9). A 50 nm window has been chosen for all spectra.

Figure 3.9 shows an example of mean and standard deviation trend of two-colour fit respectively of Schwarzschild (panel a), reduced aperture lenses (c) and full aperture ones (e). Panels b), d), f) are histograms representing the number of occurrences for the three cases in the selected window of 200 pixel = 50 nm. The effect of noise is to broaden the histogram. Once again this analysis shows that

temperature measurements with full aperture lenses are unreliable.

For the Planck and Wien fits (two-colour fits), all the data acquired have been divided into three sets corresponding to different temperature ranges: low temperatures (1600 K – 2100 K), intermediate temperatures (2100 K – 2600 K) and high temperatures (more than 2600 K). Exemplifying results are shown for each of these sets.

Figure 3.10 illustrates the measurement at  $T \approx 1800$  K with Schwarzschild, full aperture lenses and reduced aperture ones. For full aperture lenses, the two-colour fit is very effective in showing wavelength dependent deviations. It is evident how acquiring a small portion of the spectrum could lead to relevant temperature errors. For instance, as shown in 3.10(f), if the fit is made in a small window (about 50 nm) around 670 nm, the two-colour fit could seem almost flat (especially on a large scale) and the temperature could be erroneously considered as reliable. This would produce a systematic error of about 20 %. Therefore, if the two-colour plot is strongly distorted, even fitting in a small flat region the Black Body spectrum leads to inaccurate temperatures.

Reduced aperture lenses and Schwarzschild don't show any wavelength deviations: the two measurements are hence consistent with similar fit  $T$  and mean  $T$  within a dispersion (standard deviation) of  $\pm 90$  K for lenses objectives and  $\pm 60$  K for Schwarzschild microscope.

At intermediate temperatures (Figure 3.11), temperature gradients are steeper which means, in a limited resolution system, a larger chromatism. By the way, Schwarzschild and reduced aperture lenses still give consistent temperature measurements and the Wien approximation shows a negligible deviation from the ideal fit. In Figure 3.12, Figure 3.13, and Figure 3.14 temperature fits at high temperatures are presented. It has been already shown that, in this region, temperature measurements diverge significantly (hundreds of Kelvin). Wavelength deviations from the Wien fit could be seen either with Schwarzschild and with reduced aperture lenses in the fit shown in Figure 3.13 and in Figure 3.14 while they are smaller for the Schwarzschild for the fit shown in Figure 3.12. Unfortunately, while at lower temperature many measurements could be acquired, at high temperature this has been more difficult because of higher temperature instability. So only the three measurements and fit shown here could be performed. For the Schwarzschild a slight increasing trend is shown followed by a sharp decrease from 800 nm in all the three fits. A comparison to the theoretical results suggest that the upward trend could be the effect of the diffraction limit; however this is in contradiction with the resolution measurements (Figure 2.10) where the resolution of the Schwarzschild looks flat. For the lenses an upward trend is found up to 650 nm followed by a decrease in Figure 3.12 and Figure 3.13 and an increase similar to Schwarzschild in Figure 3.14. The trend that is most commonly observed on the beamline (Figure 4.1) is the one of fits Figure 3.12 and Figure 3.13, but this is not always reproducible. Therefore, the interpretation of the trends at high temperature for both Schwarzschild and lenses is not straightforward: approximations made both for the simulated PSF and for the data fit could be too strong; in particular, a parameter that has been neglected is the sample emittance wavelength dependence.

At high temperature, the above mentioned slopes for both optics are anyway not too large, so that a fit of the Planck curve can be performed in a range as large as 300 nm, considering a temperature error of about 150-200 K. Since for lenses chromatism has a little influence on the right part of the spectrum, the fit of the Black Body curve should be performed from 650-700 nm. This fit is not leading to large accuracy errors because the effect of chromatic aberrations is known (from resolution measurements) to be have an effect only at lower wavelengths. Conversely, full aperture lenses are concerned by chromatism in the whole spectrum which is deformed [I. Kantor in prep.]. Moreover, the reduced fit range chosen for lenses with iris is quite large (about 250-300 nm, as can be see in Figure 4.1).

Another useful tool that can help finding spectrum distortions, complementary to the ones shown before, has been suggested by Benedetti et al [39]: according to their results, the two-colour histogram should be as much as possible gaussian like. Intermediate and high temperatures two-colour histograms have been therefore fitted with a gaussian curve. As can be seen in the panels (e) and (f) of figures 3.11,3.12,3.13,3.14, the obtained results do confirm the Planck and two-colour ones. As absolute references are missing, fit quality, two-colour plots and histograms remain the only means to correct and improve spectroradiometric temperature measurements. So, even if Schwarzschild objectives show better quality fits, thus providing more reliable measurements, is still unclear how to evaluate the accuracy in these kind of measurements.

In the end of this chapter, temperature measurement implications for the Fe melting curve are investigated.

In Figure 3.15 many iron melting curves obtained by different groups are shown [3]. In this case the temperature difference between the ID24 melting curve and the one acquired on ID27 is huge (over 500 Kelvin and almost 1000 K at 200 GPa). Moreover, higher melting temperatures have been measured on ID27: this difference therefore cannot be attributed to systematic differences in temperature measurements which show lower temperature for the Schwarzschild microscope (ID27) with respect to the lens optics (ID24). Therefore, discrepancies in the Fe melting curve cannot be explained by systematic errors when collecting Black Body radiation. A possible explanation to these variations could be attributed to sample contamination, as it is being investigated by Morard et al. [7]; the effect of using different optics to collect Black Body radiation remains, in this case, a second order phenomenon.

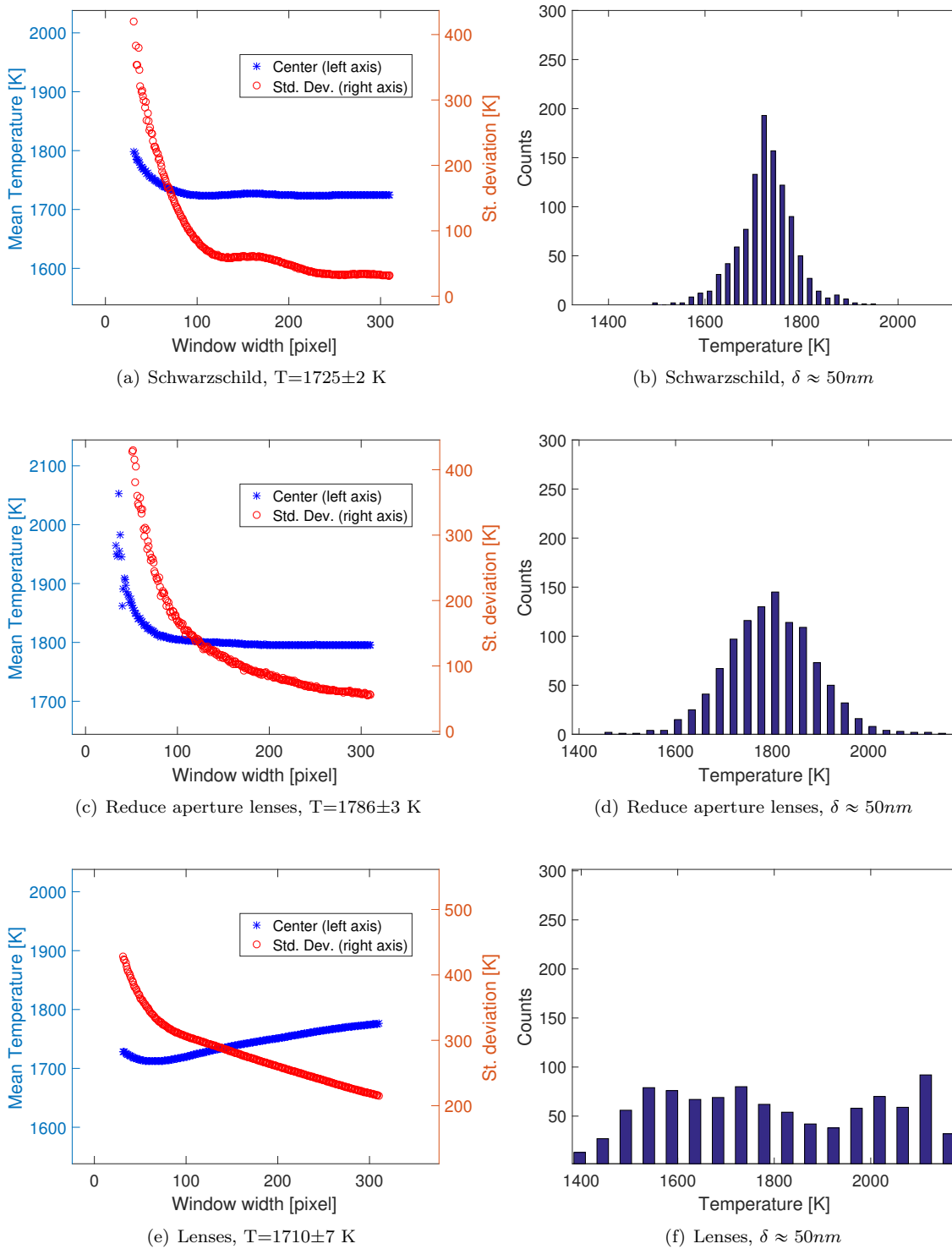
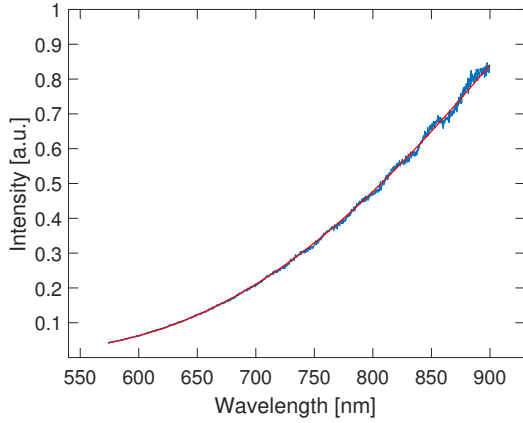
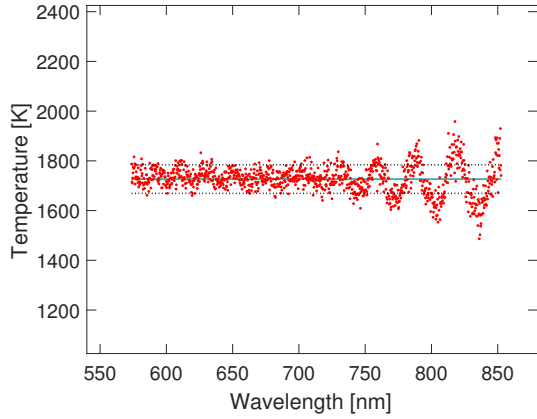


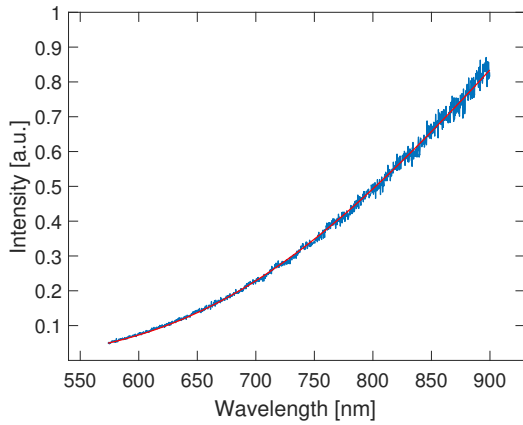
Figure 3.9: On the left column: mean and standard deviation of two-colour fits; on the x-axis, there is the wavelength window measured in pixel. On the right side: histograms representing the number of occurrences of the two-colour temperatures in the selected window: 200 pixels (about 50 nm).



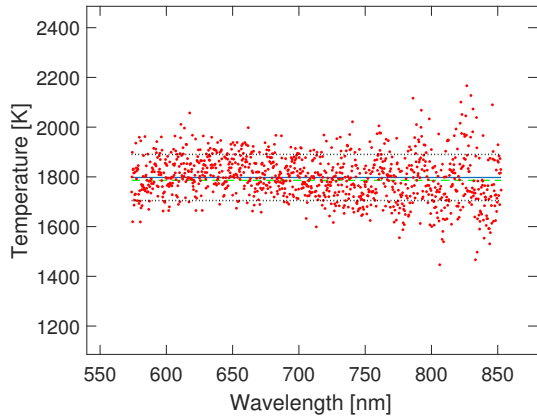
(a) Schwarzschild,  $T=1725\pm 2$  K



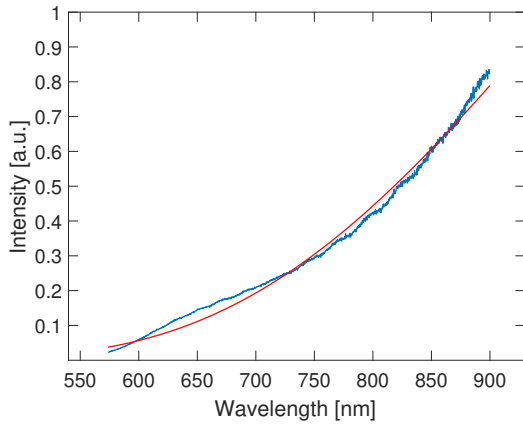
(b) Schwarzschild, two-colour fit



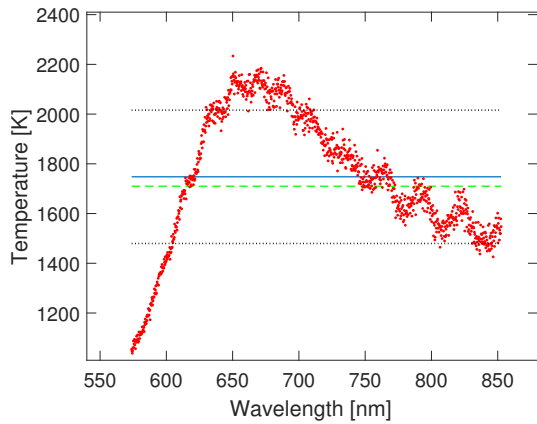
(c) Reduce aperture lenses,  $T=1786\pm 3$  K



(d) Reduce aperture lenses, two-colour fit

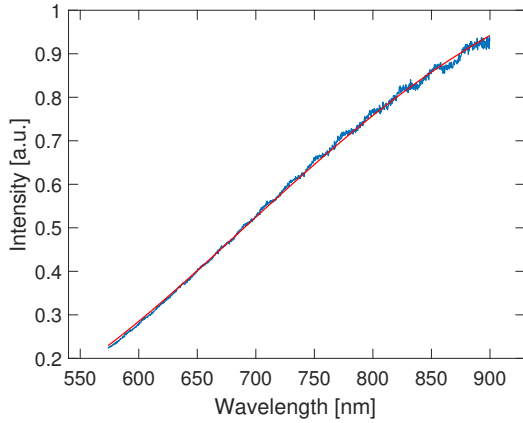


(e) Lenses,  $T=1710\pm 7$  K

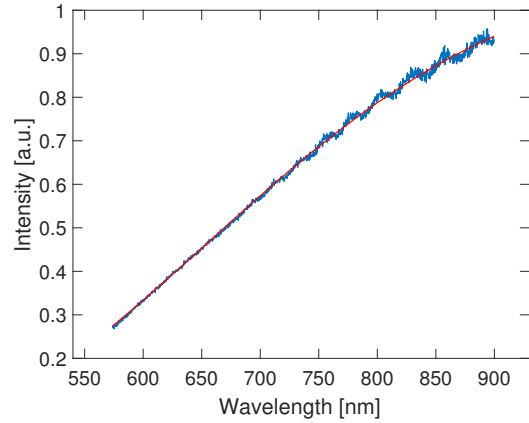


(f) Lenses, two-colour fit

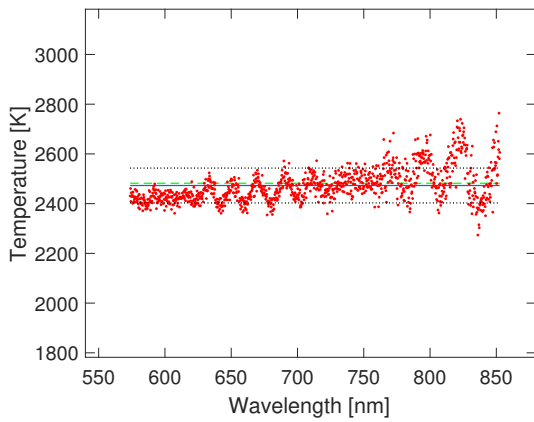
Figure 3.10: Planck fits (on the left) and two-colour fits (on the right) at low temperature. The temperatures have been measured at the same hot spot following the procedure shown in subsection 2.2.3. The blue line in the two-colour fit is the temperature evaluated with the Planck fit whereas the green dashed line is the average Wien temperature. The black dotted lines represent the 68 % confidence interval.



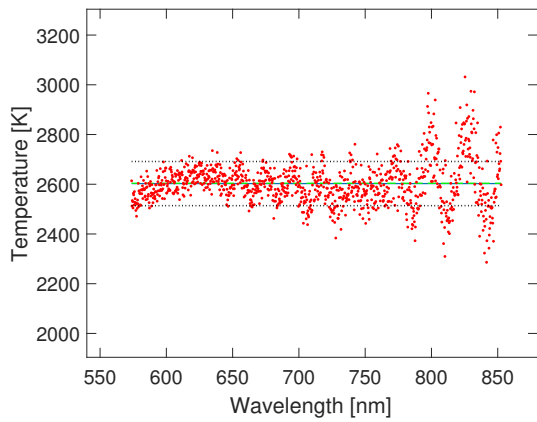
(a) Schwarzschild,  $T = 2474_{-1}^{+2}$  K



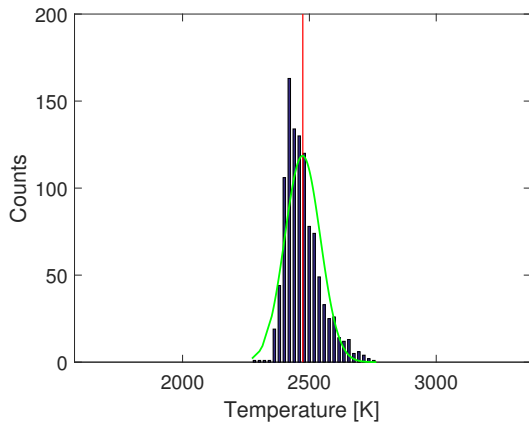
(b) Reduced aperture lenses,  $T=2604\pm 2$  K



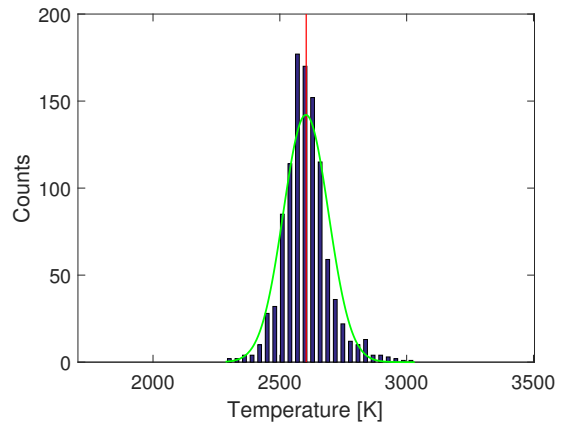
(c) Schwarzschild, two-colour fit



(d) Reduce aperture lenses, two-colour fit



(e) Schwarzschild, histogram



(f) Reduced aperture lenses, histogram

Figure 3.11: Intermediate temperature measurements: Schwarzschild plots are on the left while reduced aperture lens ones are on the right. All these plots refer to temperature measurements of the same hot spot carried out as explained in subsection 2.2.3. (a) and (b) show the Planck fits, while (c) and (d) show the two-colour fits. The last two graphs are the histograms which represent the number of occurrences of each temperature in the two-colour fit. The green curve in (e) and (f) is a gaussian curve with mean and standard deviation given by the the two-colour statistic; the red vertical line represent the fit temperature.

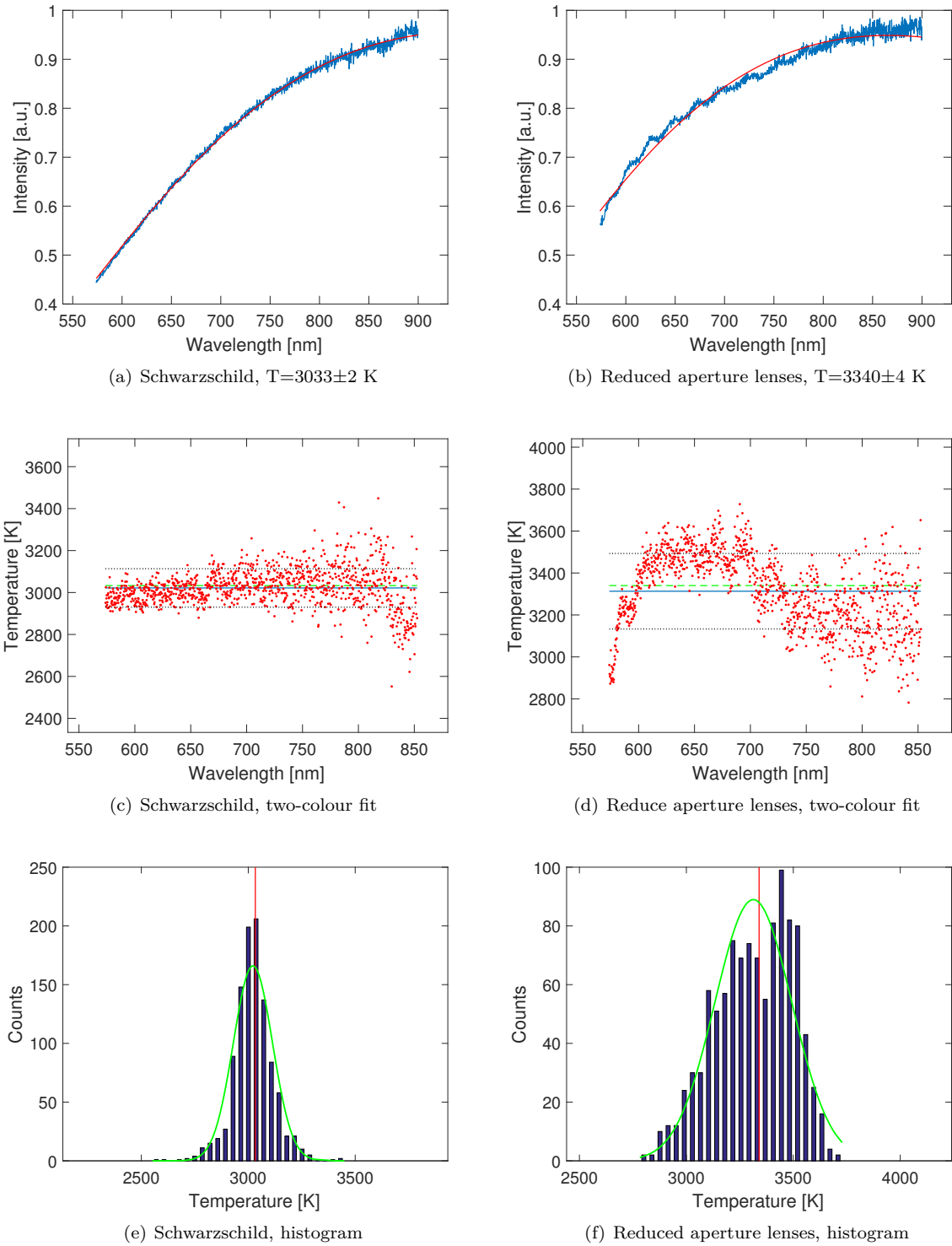


Figure 3.12: High temperature measurements: Schwarzschild plots are on the left while reduced aperture lens ones are on the right. All these plots refer to temperature measurements of the same hot spot carried out as explained in subsection 2.2.3. (a) and (b) show the Planck fits, while (c) and (d) show the two-colour fits. The last two graphs are the histograms which represent the number of occurrences of each temperature in the two-colour fit. In this measurement lens fits are considerably worse than Schwarzschild ones.

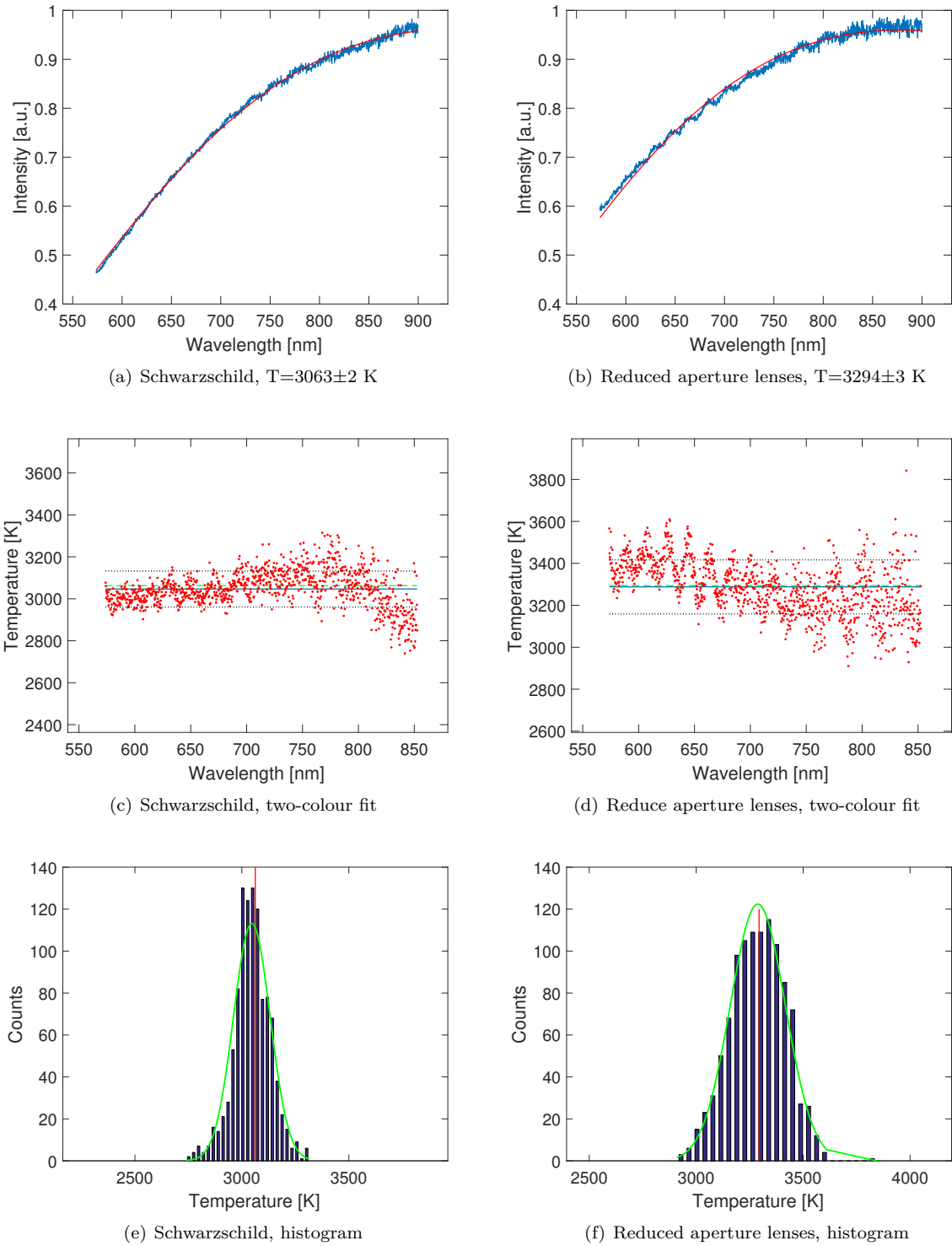


Figure 3.13: High temperature measurements: Schwarzschild plots are on the left while reduced aperture lens ones are on the right. All these plots refer to temperature measurements of the same hot spot carried out as explained in subsection 2.2.3. (a) and (b) show the Planck fits, while (c) and (d) show the two-colour fits. The last two graphs are the histograms which represent the number of occurrences of each temperature in the two-colour fit. In this measurement lens fits are considerably worse than Schwarzschild ones.

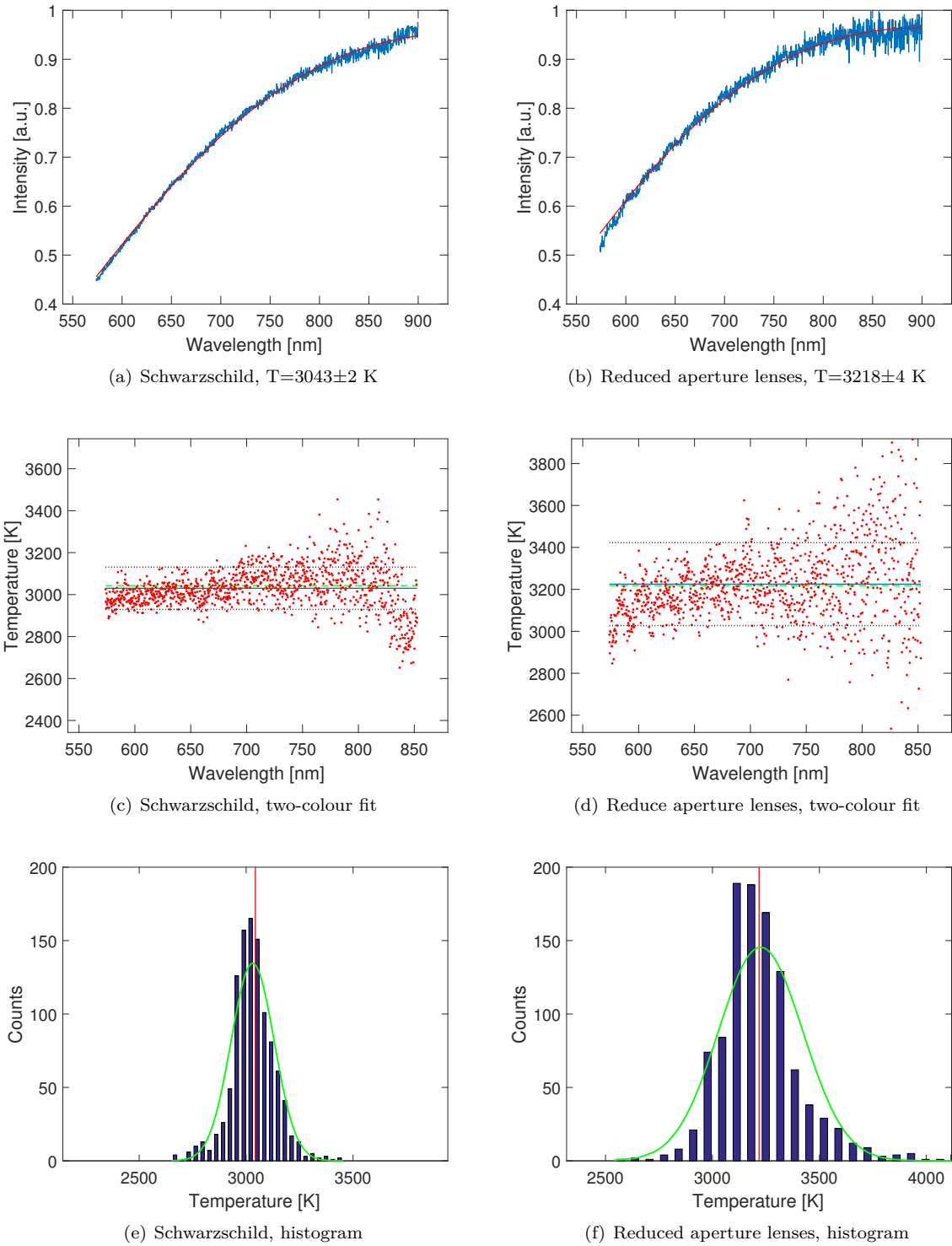


Figure 3.14: High temperature measurements: Schwarzschild plots are on the left while reduced aperture lens ones are on the right. All these plots refer to temperature measurements of the same hot spot carried out as explained in subsection 2.2.3. (a) and (b) show the Planck fits, while (c) and (d) show the two-colour fits. The last two graphs are the histograms which represent the number of occurrences of each temperature in the two-colour fit. In this measurement lens fits are considerably worse than Schwarzschild ones.

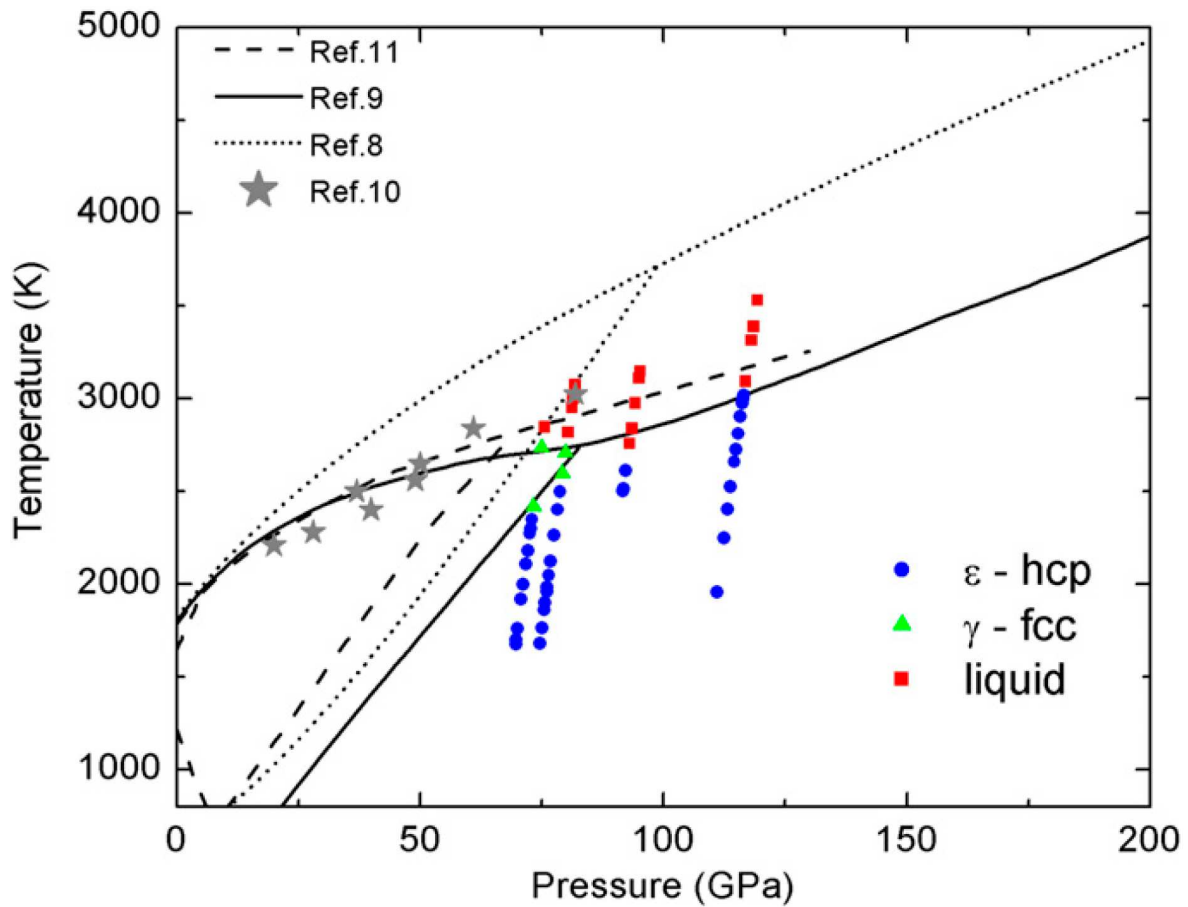


Figure 3.15: Iron melting curves, from [3]. Symbols represent temperature runs performed on ID24. Blue circles refer to solid hcp iron; red ones are liquid and green ones correspond to the fcc phase. Dotted line is the phase transition curve proposed by Anzellini et al. [2] from work on ID27, measuring temperature with Schwarzschild and using x-rays diffraction melting criterion (the melting is detected by the appearance of diffusion halo when sample is in a disordered liquid state). The temperature difference between the two curves is more than 500 Kelvins.

## Chapter 4

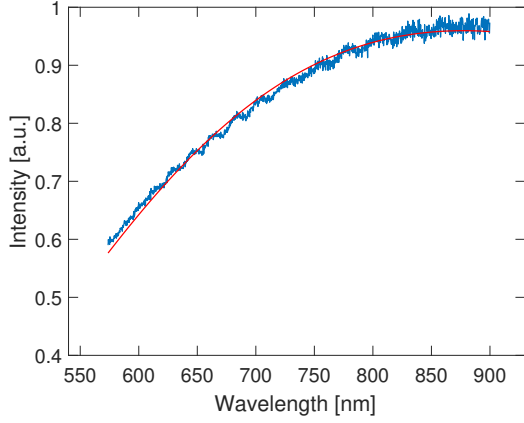
# A real experiment on a X-ray beamline

The main goal of this chapter is to show some results we have obtained on beamline (ID24), where temperature measurements have been used to determine the nickel melting curve. Hence, the usual measurement procedure on the beamline is described below as well as some preliminary results obtained. The detailed analysis of the full data set and its discussion will be shown elsewhere [6]. After that, a comparison between different melting curves obtained for Ni using different techniques is shown and the influence of the temperature measurement is investigated.

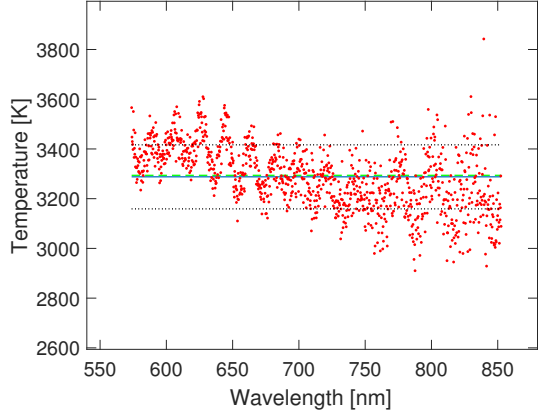
The X-ray Absorption (XAS) beamline ID24 is optimized for in situ experiments at high pressure and high temperature. Extreme conditions of pressure and temperature are obtained by using the laser heated DAC, as explained in chapter 1. The beamline operates in an energy dispersive geometry, so that a whole XAS spectrum is acquired simultaneously and measurements can be performed in tens of milliseconds or less [10]. The XAS technique allows getting information on electronic and short-range order structure of matter, providing selectivity of atomic species [52]. XAS can be used as a powerful tool to detect the melting of a sample [5] [4] and to investigate its local structure both in the solid and in the liquid phase [6]. Recently, on ID24 Fe, Co and Ni melting phenomena have been studied and, in particular, the melting curves of these three metals have been determined [5] [6] [3]. These melting curves are obtained by performing many temperature runs in which the sample is kept at a constant pressure (in the range of 10-100 GPa) and its temperature is increased step by step by increasing the laser power. Two lasers are used to heat the sample simultaneously from both sides, the laser power can be adjusted independently to balance the temperature on the two sides [see subsection 1.4.1].

Each temperature run is performed as follows: for each laser power of the lasers, the x-ray acquisition and the temperature acquisition are synchronized by means of a multichannel pulse generator. The x-ray acquisition time is determined by the sample assembly absorption. Typically for a 4  $\mu\text{m}$  Ni foil embedded in KCl in a DAC, a good signal to noise ratio is obtained averaging  $\approx 50$  acquisitions of  $\approx 30$  ms integration time, for a total time of 1.5 seconds. Therefore the laser is switched on for a short time (less than 2 seconds) which is important to prevent sample reactions and mechanical instabilities [53] [7]. Fits to the emission curves are carried out in real time to obtain the sample temperature. The temperature error is given by the two colors fit error and by the temperature difference obtained from the two sides of the cell. Great care is also paid to optics alignment and to the alignment of the hot spot with the x-ray beam and the spectrometer pinhole: it has already been shown [1] [38] [23] that misalignments could lead to errors in temperature measurements of hundreds of Kelvins.

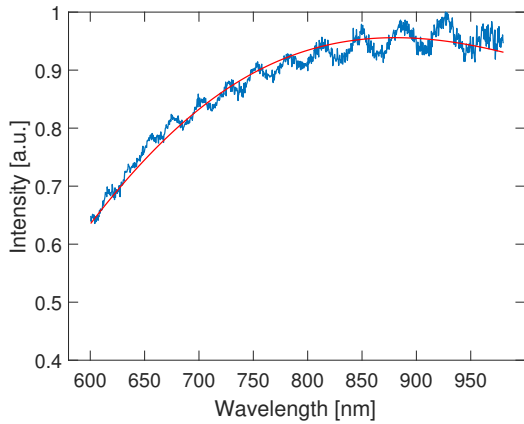
In Figure 4.1 typical ID24 Black Body spectra are shown in comparison to the ones acquired in the setup we assembled to compare lenses and Schwarzschild. Fit quality and two colour wavelength behaviour are similar.



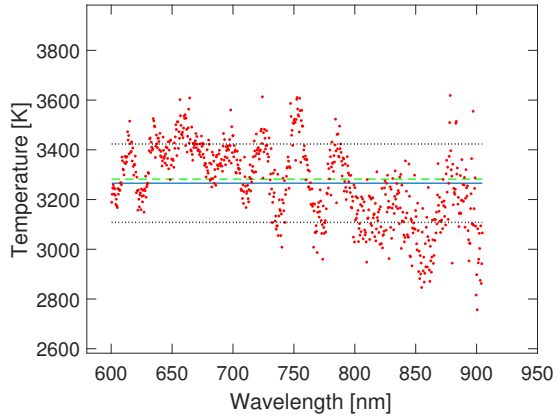
(a) Lenses + Iris, laser lab, Planck fit,  $T=3294\pm 3$  K



(b) Lenses + Iris, laser lab, two-colour,  $T=3294\pm 3$  K



(c) Lenses + Iris, ID24, Planck fit,  $T=3282\pm 6$  K



(d) Lenses + Iris, ID24, two-colour,  $T=3282\pm 6$  K

Figure 4.1: Comparison between the best reduced aperture spectrum taken in the laser lab on a W sample in KCl at  $T=3294 \pm 3$  K (top panels) and some high temperature ones taken on ID24 on a Co sample in KCl at  $3282 \pm 6$  K (bottom panels). Planck fits are on the left column, two colour fits are on the right one. Spectra acquired on the beamline are obtained using polycrystalline diamond anvil (NPD anvil) instead as the usual monocrystalline diamonds. These diamonds required an additional calibration which is obtained by collecting the NPD anvil spectrum at room temperature and room pressure.

The occurrence of the melting is detected by XAS as a change in shape in the near edge region. In particular the bump on the rising edge, present in the solid phase disappears and the two bumps just after the edge flatten out (Figure 4.2).

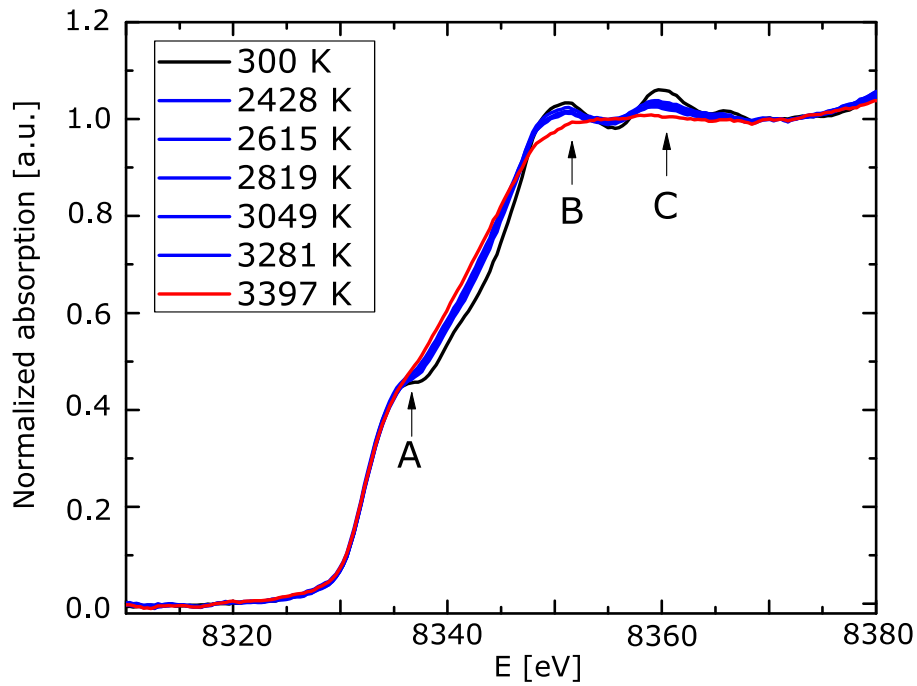


Figure 4.2: XAS spectra of Ni taken on ID24 [6]. A, B, C are the points in which the melting is especially visible. The disappearance of the bumps (B,C) and of the shoulder (A) represent the melting criterion in XAS spectroscopy.

Preliminary results from an experiment on Ni are shown in Figure 4.3. Nickel shows a face-centered cubic structure stable over a wide P-T range. Many runs have been carried out using nickel as sample and KCl as pressure medium. Each run is represented by a column of circles. As shown in the figure, the melting curve measured by XAS on ID24 [6] is comparable with the one proposed by Lord which has been measured on ID27. Up to 75 GPa the curve found by XAS is slightly higher (200 K max at 75 GPa) than that recorded on ID27, in agreement with the differences in spectroradiometric temperature measurements performed with lenses (on ID24) and Schwarzschild (on ID27) in the laboratory. However this is not the case for the last two points at 80 and 100 GPa. It is worth underlining that, while the measurements in the lab have been performed with the two optics on the same samples and loadings in the DAC, the results from the experiments shown in Figure 4.3 are acquired in different moments using different loadings.

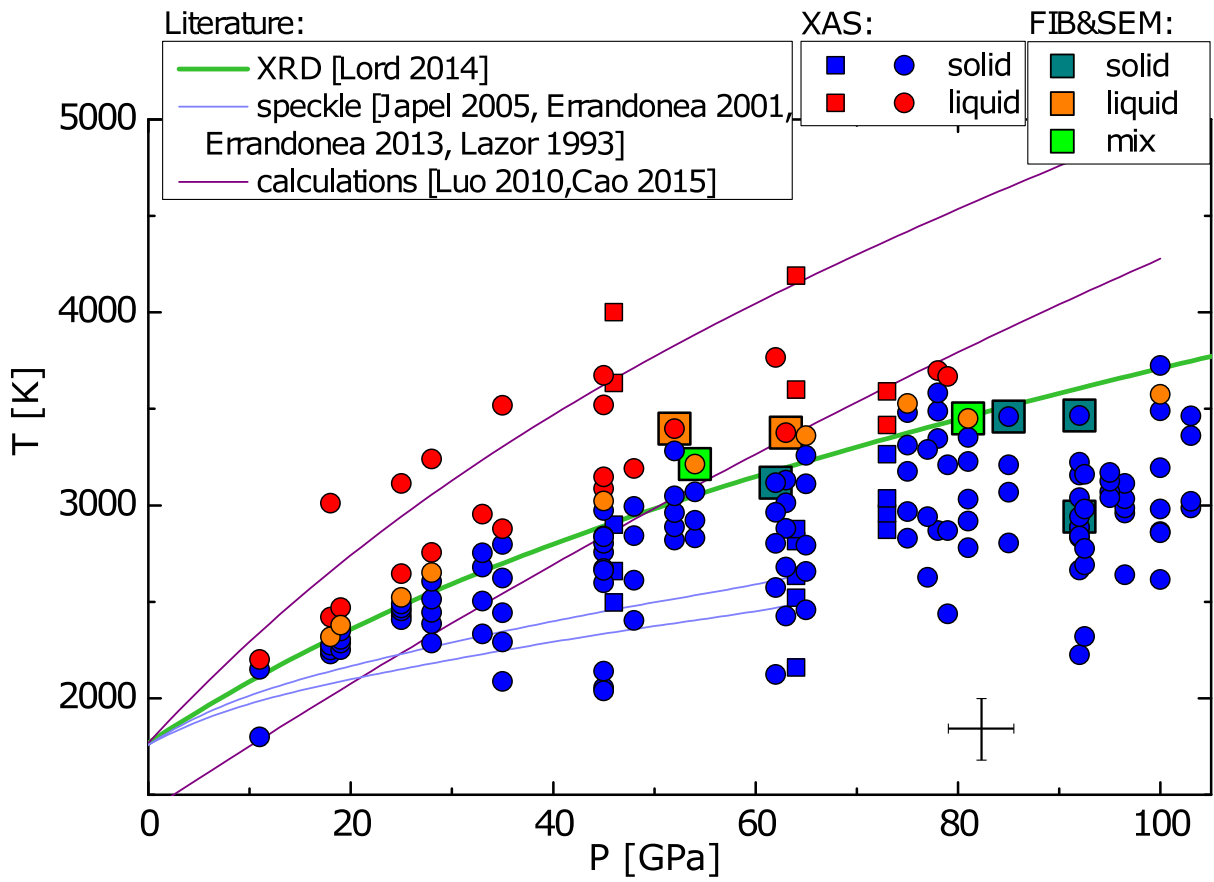


Figure 4.3: Melting curves of Ni taken on ID24 [6]. Circles in a column are measurements of the same run. Blue circles correspond to solid sample according to EXAFS spectra. Red circles are liquids. Some points (square frame) have been cut with a focused ion beam (FIB) and analysed with scanning electron microscope (SEM) to check to EXAFS criterion of melting. The green curve is the curve that has been measured by Lord et al. on ID27 using Schwarzschild [54].

# Chapter 5

## Conclusions

Emerging geophysical and material science interests in the physical properties of materials at high temperature and high pressure have raised the importance of extreme conditions science. Many laser heated diamond anvil cell setups have been designed to achieve such experimental conditions and most of them use synchrotron light to investigate samples' structure. Measurements are very challenging and require both an adequate control on sample preparation and on probing techniques. The inconsistency between melting curves investigated at high temperatures and high pressures (up to thousands of Kelvin and hundreds of GPa) has led scientists to put a great deal of effort in improving the accuracy of extreme condition measurements. Different causes have been identified to be responsible for these discrepancies; pursuing improvement in measurement standards has showed the need to deal with each problem separately. In this work, temperature measurements have been taken into consideration: a direct comparison between spectroradiometric measurements performed in LHDAC setups with refractive and reflective objectives has been carried out. The first result of these experiments confirms that large numerical aperture (NA= 0.2) achromatic doublets suffer from strong chromatic aberrations even at low temperature. The use of these kind of objectives without pupils is therefore strongly discouraged: reducing fit wavelength window arbitrarily can bring to large systematic errors. Reduced aperture (NA = 0.065) lenses show adequate quality fits up to  $\approx 2500\text{K}$ . Beyond this temperature fit quality is deteriorating and some features that could be ascribed to chromatic aberrations appear at low wavelengths; nevertheless, the two-colour plot shows an almost flat region (about 250-300 nm) for wavelengths greater than 700 nm. By fitting the Planck curve in the right part of the spectrum, the region in which the two-colour plot is flat, the temperature is slightly lower but doesn't change significantly (about 50 K). The same wavelength dependent behaviour has been observed for the two-colour plots measured during real experiments on the beamline. Optics based on mirrors (Schwarzschild objective) shows less wavelength dependent distortions in the two-colour plot and slightly better Planck fits.

Measurements in the same conditions with Schwarzschild and reduced aperture lenses shows no significant temperature differences up to about 2500K: however, temperatures measured with reflective optics are always lower than the ones acquired with lenses. Above 2500 K, the difference between the two temperatures is increasing up to 200 K at 3100 K. Despite the scarce sampling at high temperatures, due to the difficulties to have a stable emission of the sample, the temperature difference is systematic and pressure independent (for pressures smaller than 80 GPa).

Applying the results obtained to Iron melting curves shows clearly that temperature measurements cannot account for melting curve discrepancies: the temperature difference between the two curves is too large and is reverse biased. Some theoretical simulations of lossless perfectly achromatic systems have been carried out in order to understand the effect of limited resolution in spectroradiometric measurements. It has been found out that diffraction limited optics tends to overestimate the temperature: about 90 K at 3300 K with NA = 0.065. The temperature overestimation increases as the peak temperature goes up or the numerical aperture decreases. Even systems with a wavelength independent resolution are affected by temperature errors. In these cases, temperatures are underestimated: 150 K with 10  $\mu\text{m}$  resolution.

So far, a proper absolute spectroradiometric temperature reference is still missing as well as a procedure to quantify temperature errors. To significantly improve temperature measurements it is necessary to have flat-top hot spot that would help reduce thermal gradients; this could be achieved putting a pi-shaper or a phase plate in the laser optical path.

# List of Figures

1.1	Tantalum melting curves from theoretical simulations, static and laser shock data [15]. The great amount of different melting curves published on different papers shows that an unanimous consensus about melting temperatures at high pressure is still lacking. . . . .	3
1.2	Iron melting curves [3]. Circles represent temperature runs performed on the XAS beam-line ID24 using refractive optics. Blue circles refer to solid hcp iron; ; green ones correspond to the solid fcc phase and red ones to the liquid. Dotted line is the phase transition curve proposed by Anzellini et al. [2], measuring temperature with Schwarzschild mirrors and using x-rays diffraction melting criterion (the melting is detected by the appearance of diffusion halo when sample is in a disordered liquid state). The temperature difference between the two curves is larger than 500 K. . . . .	4
1.3	P-T domain reachable with three different techniques: resistive heating (grey), laser heating diamond anvil cell (diamond patterned) and shock compression (dynamic technique) [8] [17] [18] [19]. . . . .	5
1.4	Example of a Letoullec DAC. the diamonds are in the proper centre of the cell holders and are carefully aligned to show parallel surfaces when the cell is closed. . . . .	6
1.5	Picture of a Ni sample in a pressurized loaded DAC. The outer dark ring is the gasket. In the centre it is possible to see the sample (dark rectangle) and two rubies (used for pressure measurements) on the side. The sample is surrounded by the pressure medium (KCL) and squeezed between the two diamonds. . . . .	6
1.6	Drawing (not to scale) showing the principle of the DAC. The sample is kept in a pressure medium and is squeezed by the diamond heads. One or more rubies are placed near the sample to perform pressure measurements. When the force is exerted on diamonds, the gasket gets distorted: indeed, it is the friction between the gasket and the diamonds that allows the pressure medium and the sample not to come out from the DAC. . . . .	7
1.7	Drawing illustrating Black Body principle. Whichever the material, a cavity with a small hole is always a good approximation of a Black Body [26]: the small light intensity that turns out to enter the cavity undergoes many reflections and, at each reflection, it is partially absorbed. In the end, the light coming from outside the cavity will be entirely absorbed and the emission of the cavity is essentially related to the thermal emission of the inner surfaces. . . . .	9
1.8	Planck's law and Rayleigh-Jeans' law at 3000K. At low frequencies, the two curves agree with each other, but at higher frequencies the Rayleigh-Jeans one diverges; this phenomenon is known as "ultraviolet catastrophe" and it is solved only in a quantum mechanical model of thermal emission (Planck's law). . . . .	10
1.9	Planck spectra at different temperatures as a function of wavelengths. Comparing these spectra, it is possible to observe both the Wien displacement law and the Stephan-Boltzmann one: as the temperature increases, the peak shift towards lower wavelengths and the emitted power (area below the Planck's curve) increases. . . . .	11
1.10	Schematic illustrating the geometry of radiant emission. Radiance is defined as the radiant flux divided by the solid angle ( $d\Omega$ ) at which the radiation is emitted and by the emitting surface ( $dA\cos\theta$ ) perpendicular to the considered direction. . . . .	12

1.11	Lambertian source drawing. The intensity of thermal emission depends with a cosine law on the angle ( $\theta$ ) formed with the perpendicular to the emitting surface. . . . .	13
1.12	Two-colour fit on the left, histogram on the right. Example of an acceptable measurement: the two-colour is flat and the histogram is Gaussian. From [8]. . . . .	15
1.13	Two-colour fit on the left, histogram on the right. The two-colour fit is not flat, indicating that the temperature measurement is not reliable. These conclusions can also be inferred by looking at the histogram: the two-colour distribution is far from being Gaussian. From [8]. . . . .	15
1.14	Plot of the central value (centre) and standard deviations of two-colour histograms as a function of wavelength windows $\delta$ (in pixel). This plot is made to choose the best wavelength difference with which drawing two-colours graphs. From [39]. . . . .	16
1.15	A simplified outline of spectroradiometric temperature measurements in the LHDAC. The sample is kept in a diamond anvil cell and heated with a laser. The optical system is used to collect light and to take it to the spectrometer entrance (pinhole). Around the pinhole, there is usually a mirror which reflects the image of the sample; this image is collected by a camera allowing to align the optics on the desired spot. . . . .	17
1.16	Schwarzschild scheme: light is collected by the primary mirror (concave) and then reflected to the secondary mirror. The image is usually formed at greater distances compared to those between the object and the mirrors: this results in a high magnification of the system. . . . .	18
1.17	Drawing illustrating Snell's law. . . . .	18
1.18	Axial Chromatic aberrations: parallel rays at different frequencies are focuses in different position along the optical axis. . . . .	19
1.19	(a) shows the resolution effect of chromatic aberrations. (b) illustrates the effect of Iris in reducing the chromatic aberration broadening by cutting marginal rays. Dashed black line represent the image plane considered. . . . .	20
1.20	Effect of chromatic aberrations on temperature profiles. On the left the profiles of three different wavelengths are shown; on the right the profiles once they reach the spectrometer entrance. Wavelength dependent point spread function can strongly distort spectra causing extensive errors in temperature measurements. Dashed black circle on the right side: pinhole. . . . .	21
1.21	With a uniform hot spot the pinhole is sampling the same spectrum emitted by the sample. Measurements are not affected by chromatic aberrations. . . . .	21
1.22	On the right: mirror based optics (Schwarzschild) from ID27. On the left: achromatic doublets inserted in custom-built microscope units from ID24. . . . .	22
1.23	ID27 Schwarzschild scheme [42]. Mp is the primary mirros, Ms is the secondary one. The distance between the image and the object is 859mm and the one between the primary mirror and the object is about 184mm; this configuration leads to a numerical aperture of 0.18. . . . .	22
1.24	ID24 microscope schematic [5]. The objective focal length(1) is 30mm, the field lens(3) one is 500mm. A mirror (2) is placed at 45° between the two lenses and an iris (4) can be put in front of the objective during temperature measurements. The numerical aperture without iris is 0.2, with iris is around 0.065. . . . .	23
1.25	Right picture: view of the ID24 overall setup. The DAC is kept in the bronze-colour holder marked with a red circle. X-rays (green dashed lines), laser and optics should be all aligned in the same position on the sample. The spectra (Planck, Ruby, Raman) are collected by the optics and brought at the spectrometer entrance (Light-blue rectangle). On the left a detail: the two custom-made objectives are clearly recognizable on both sides of the sample holder. The sample is heated from both sides: the lenses used for the laser focus are positioned at $\approx 30$ degrees with respect to the objectives. . . . .	24
1.26	ID24 laser heating setup schematic. LED illumination is used for the optics alignment. During measurements lights are off and the LEDs are moved out from the optical path. . . . .	25

1.27	Panel (a): detail of ID27 laser heating setup; laser focus lenses are clearly visible (100 mm focal lenses). The diamond anvil cell is kept in the holder marked with an orange circle. The X-ray path is sketched with a green dashed line. Panel (b): back part of the ID27 setup. Light is collected by Schwarzschild optics (red circles) and brought to the spectrometer entrance (light blue rectangle). Measurements from the two sides of the cell are not done simultaneously, but mirror filters are rapidly flipped to look at both sample sides of the diamond anvil cell. . . . .	25
1.28	ID27 laser heating setup schematic. . . . .	26
2.1	Top panel: picture of the setup. Bottom panel: zoom over the cell area. . . . .	28
2.2	Schematic drawing of the setup. Schwarzschild microscope and lenses can be moved by means of pneumatic actuators to allow a fast switch between the two optics. DAC is the diamond anvil cell and BS is beamsplitter. . . . .	29
2.3	Temperature calibration using a tungsten lamp placed at the sample position. . . . .	30
2.4	Raw spectra from which the fit has been subtracted either for Schwarzschild (2.4(a)) and for reduce aperture lenses (2.4(b)). . . . .	31
2.5	Schwarzschild (2.5(a)) and reduced aperture lenses (2.5(b)) noises fits to a Fabry-Pérot interferometer model. . . . .	32
2.6	Time stability measurement for Schwarzschild (1 s exposure time, panel a) and reduced aperture lenses (2.5 s exposure time, panel b). The measurements have been performed by heating continuously a W sample in a DAC, embedded in KCl as pressure, with the Ytterbium laser. The temperature acquisition is synchronized to the laser switching on. . . . .	32
2.7	Time stability measurement performed with reduced aperture lenses (2.5 s exposure time) after letting the sample stabilize several minutes. When temperature is stable, the standard deviation has a value of few Kelvin. . . . .	33
2.8	Spot images. (a),(b): hot spot of measured temperatures. (c),(d): not acceptable. The red viewfinder in picture (a) has been used during experiments for an accurate alignment of the pinhole with the hot spot. . . . .	34
2.9	Reduced aperture lenses resolution measured on ID24 for different focal distances. From [5].	35
2.10	Schwarzschild resolution measurements taken on ID27 [I. Kantor, G. Garbarino]. . . . .	35
3.1	a) Gaussian Temperature profile; b) Black Body profiles at four different wavelengths. c), d) PSF respectively of 1 $\mu\text{m}$ and 10 $\mu\text{m}$ . e), f) PSF at four different wavelengths for a diffraction limited optical system with numerical aperture of 0.18 and 0.065. . . . .	38
3.2	Two-colour and Planck fits of the spectra obtained with two different resolutions: a), c) are the plots related to 1 $\mu\text{m}$ resolution whereas b), d) are related to 10 $\mu\text{m}$ resolution. The temperature measured with the two different resolutions are respectively: 3296 K and 3150 K. The dashed line in the Planck fit is the ideal spectrum obtained with an infinite resolution optical system ( $T = 3300$ K). In the two-colour fit the red line represents the temperature of the fit. $T$ mean (blue line) is the average of the two-colour fit temperatures. The green line in the same plots is the temperature obtained from the Planck fit. . . . .	40
3.3	Two-colour and Planck fits of a diffraction limited resolution system are here presented; a), c) are related to an optical system with numerical aperture of 0.18 whereas b) and d) are those obtained with a numerical aperture of 0.065. The temperature obtained are, respectively, 3310 K and 3391 K. . . . .	41
3.4	Two-colour plot for $NA = 0.18$ . . . . .	42
3.5	Two-colour plot, Planck fit, and two-colour histogram related to the 10 $\mu\text{m}$ constant resolution optical system. Simulations have been performed like in the previous examples, but gaussian white noise has been added in the Black Body spectrum before fitting it. The measured temperature is 3150 K. Dashed lines in the two-colour plot represent the 68% confidence interval of the two-colour temperature distribution. The blue line is the average of the two-colour temperatures while the green line is the temperature obtained from the Planck fit. The dashed vertical line in the histogram shows the real temperature on the hot spot; the red one is the average of the two-colour temperatures. . . . .	43

3.6	Normalized Planck spectra and fits of the same hot spot collected with different optical systems. The errors shown in the figure are purely fit errors. . . . .	44
3.7	Measurements of the same temperatures with Schwarzschild and with reduce aperture lenses (iris); the blue line indicates a linear trend. Measurements have been carried out as shown in chapter 2. Data at three different pressure are shown. . . . .	45
3.8	Temperature difference plotted vs measured temperature with Schwarzschild optics at three different pressures. . . . .	46
3.9	On the left column: mean and standard deviation of two-colour fits; on the x-axis, there is the wavelength window measured in pixel. On the right side: histograms representing the number of occurrences of the two-colour temperatures in the selected window: 200 pixels (about 50 nm). . . . .	49
3.10	Planck fits (on the left) and two-colour fits (on the right) at low temperature. The temperatures have been measured at the same hot spot following the procedure shown in subsection 2.2.3. The blue line in the two-colour fit is the temperature evaluated with the Planck fit whereas the green dashed line is the average Wien temperature. The black dotted lines represent the 68 % confidence interval. . . . .	50
3.11	Intermediate temperature measurements: Schwarzschild plots are on the left while reduced aperture lense ones are on the right. All these plots refer to temperature measurements of the same hot spot carried out as explained in subsection 2.2.3. (a) and (b) show the Planck fits, while (c) and (d) show the two-colour fits. The last two graphs are the histograms which represent the number of occurrences of each temperature in the two-colour fit. The green curve in (e) and (f) is a gaussian curve with mean and standard deviation given by the the two-colour statistic; the red vertical line represent the fit temperature. . . . .	51
3.12	High temperature measurements: Schwarzschild plots are on the left while reduced aperture lense ones are on the right. All these plots refer to temperature measurements of the same hot spot carried out as explained in subsection 2.2.3. (a) and (b) show the Planck fits, while (c) and (d) show the two-colour fits. The last two graphs are the histograms which represent the number of occurrences of each temperature in the two-colour fit. In this measurement lens fits are considerably worse than Schwarzschild ones. . . . .	52
3.13	High temperature measurements: Schwarzschild plots are on the left while reduced aperture lense ones are on the right. All these plots refer to temperature measurements of the same hot spot carried out as explained in subsection 2.2.3. (a) and (b) show the Planck fits, while (c) and (d) show the two-colour fits. The last two graphs are the histograms which represent the number of occurrences of each temperature in the two-colour fit. In this measurement lens fits are considerably worse than Schwarzschild ones. . . . .	53
3.14	High temperature measurements: Schwarzschild plots are on the left while reduced aperture lense ones are on the right. All these plots refer to temperature measurements of the same hot spot carried out as explained in subsection 2.2.3. (a) and (b) show the Planck fits, while (c) and (d) show the two-colour fits. The last two graphs are the histograms which represent the number of occurrences of each temperature in the two-colour fit. In this measurement lens fits are considerably worse than Schwarzschild ones. . . . .	54
3.15	Iron melting curves, from [3]. Symbols represent temperature runs performed on ID24. Blue circles refer to solid hcp iron; red ones are liquid and green ones correspond to the fcc phase. Dotted line is the phase transition curve proposed by Anzellini et al. [2] from work on ID27, measuring temperature with Schwarzschild and using x-rays diffraction melting criterion (the melting is detected by the appearance of diffusion halo when sample is in a disordered liquid state). The temperature difference between the two curves is more than 500 Kelvins. . . . .	55

4.1	Comparison between the best reduced aperture spectrum taken in the laser lab on a W sample in KCl at $T=3294 \pm 3$ K (top panels) and some high temperature ones taken on ID24 on a Co sample in KCl at $3282 \pm 6$ K (bottom panels). Planck fits are on the left column, two colour fits are on the right one. Spectra acquired on the beamline are obtained using polycrystalline diamond anvil (NPD anvil) instead as the usual monocrystalline diamonds. These diamonds required an additional calibration which is obtained by collecting the NPD anvil spectrum at room temperature and room pressure. . . . .	57
4.2	XAS spectra of Ni taken on ID24 [6]. A, B, C are the points in which the melting is especially visible. The disappearance of the bumps (B,C) and of the shoulder (A) represent the melting criterion in XAS spectroscopy. . . . .	58
4.3	Melting curves of Ni taken on ID24 [6]. Circles in a column are measurements of the same run. Blue circles correspond to solid sample according to EXAFS spectra. Red circles are liquids. Some points (square frame) have been cut with a focused ion beam (FIB) and analysed with scanning electron microscope (SEM) to check to EXAFS criterion of melting. The green curve is the curve that has been measured by Lord et al. on ID27 using Schwarzschild [54]. . . . .	59

# Bibliography

- [1] Michael J. Walter and Kenneth T. Koga. The effects of chromatic dispersion on temperature measurement in the laser-heated diamond anvil cell. *Physics of the earth and planetary interiors*, 143-144:541–558, June 2004.
- [2] S. Anzellini, A. Dewaele, M. Mezouar, P. Loubeyre, and G. Morard. Melting of iron at earth’s inner core boundary based on fast x-ray diffraction. *Science*, 340(6131):464–466, 2013.
- [3] Giuliana Aquilanti, Angela Trapananti, Amol Karandikar, Innokenty Kantor, Carlo Marini, Olivier Mathon, Sakura Pascarelli, and Reinhard Boehler. Melting of iron determined by x-ray absorption spectroscopy to 100 gpa. *Proceedings of the National Academy of Sciences*, 112(39):12042–12045, 2015.
- [4] R. Torchio, S. Boccato, V. Cerantola, G. Morard, T. Irifune, and I. Kantor. Probing the local, electronic and magnetic structure of matter under extreme conditions of temperature and pressure. *High Pressure Research*, 36(3):293–302, 2016.
- [5] Innokenty Kantor. A laser heating facility for energy-dispersive x-ray absorption spectroscopy. In preparation.
- [6] Silvia Boccato. The melting curve of nickel up to 100 gpa explored by xas. *Geophysical Research Letters*, In preparation.
- [7] Guillaume Morard. In preparation.
- [8] S. Anzellini. *Phase diagram of iron under extreme conditions measured with time-resolved methods*. PhD thesis, Université Pierre et Marie Curie, May 2014.
- [9] M Mezouar, WA Crichton, S Bauchau, F Thurel, H Witsch, F Torrecillas, G Blattmann, P Marion, Y Dabin, J Chavanne, et al. Development of a new state-of-the-art beamline optimized for monochromatic single-crystal and powder x-ray diffraction under extreme conditions at the esrf. *Journal of synchrotron radiation*, 12(5):659–664, 2005.
- [10] S. Pascarelli, O. Mathon, T. Mairs, I. Kantor, G. Agostini, C. Strohm, S. Pasternak, F. Perin, G. Berruyer, P. Chappelet, C. Clavel, and M. C. Dominguez. The Time-resolved and Extreme-conditions XAS (TEXAS) facility at the European Synchrotron Radiation Facility: the energy-dispersive X-ray absorption spectroscopy beamline ID24. *Journal of Synchrotron Radiation*, 23(1):353–368, Jan 2016.
- [11] DJ Stevenson. Models of the earth’s core. *Science*, 214(4521):611–619, 1981.
- [12] John A Jacobs. *The Earth’s core*, volume 37. Academic Press, 1987.
- [13] Quentin Williams and Raymond Jeanloz. Melting relations in the iron-sulfur system at ultra-high pressures: Implications for the thermal state of the earth. *Journal of Geophysical Research: Solid Earth*, 95(B12):19299–19310, 1990.

- [14] Mohamed Mezouar. Methodology for in situ synchrotron x-ray studies in the laserheated diamond anvil cell. *High Pressure Research*, submitted.
- [15] Amol Karandikar and Reinhard Boehler. Flash melting of tantalum in a diamond cell to 85 gpa. *Phys. Rev. B*, 93:054107, Feb 2016.
- [16] R. Boehler. High-pressure experiments and the phase diagram of lower mantle and core materials. *Reviews of Geophysics*, 38(2):221–245, 2000.
- [17] L Dubrovinsky, N Dubrovinskaia, O Narygina, I Kantor, A Kuznetsov, VB Prakapenka, Levente Vitos, Börje Johansson, AS Mikhaylushkin, SI Simak, et al. Body-centered cubic iron-nickel alloy in earth’s core. *Science*, 316(5833):1880–1883, 2007.
- [18] Shigehiko Tateno, Kei Hirose, Yasuo Ohishi, and Yoshiyuki Tatsumi. The structure of iron in earth’s inner core. *Science*, 330(6002):359–361, 2010.
- [19] Ashkan Salamat, Rebecca A Fischer, Richard Briggs, Malcolm I McMahon, and Sylvain Petitgirard. In situ synchrotron x-ray diffraction in the laser-heated diamond anvil cell: Melting phenomena and synthesis of new materials. *Coordination Chemistry Reviews*, 277:15–30, 2014.
- [20] Aiyasami Jayaraman. Diamond anvil cell and high-pressure physical investigations. *Reviews of Modern Physics*, 55(1):65, 1983.
- [21] CE Weir, ER Lippincott, A Van Valkenburg, and EN Bunting. Infrared studies in the 1-to 15-micron region to 30,000 atmospheres. *J. Res. Natl. Bur. Stand. A*, 63.
- [22] R Letoullec, JP Pinceaux, and P Loubeyre. The membrane diamond anvil cell: a new device for generating continuous pressure and temperature variations. *International Journal of High Pressure Research*, 1(1):77–90, 1988.
- [23] Guoyin Shen, Mark L. Rivers, Yanbin Wang, and Stephen R. Sutton. Laser heated diamond cell system at the advanced photon source for in situ x-ray measurements at high pressure and temperature. *Review of Scientific Instruments*, 72(2):1273–1282, 2001.
- [24] HK Mao, PM Bell, JW t Shaner, and DJ Steinberg. Specific volume measurements of cu, mo, pd, and ag and calibration of the ruby r 1 fluorescence pressure gauge from 0.06 to 1 mbar. *Journal of applied physics*, 49(6):3276–3283, 1978.
- [25] Agnes Dewaele, Paul Loubeyre, and Mohamed Mezouar. Equations of state of six metals above 94 gpa. *Physical Review B*, 70(9):094112, 2004.
- [26] Pierre-Marie Robitaille. Kirchoff’s law of thermal emission: 150 years. *Progress in Physics*, 4:3, 2009.
- [27] Franco Ciccacci. *Fondamenti di fisica atomica e quantistica*. Second edition.
- [28] John R. Howell, Robert Siegel, and M. Pinar Mengüç. *Thermal radiation heat transfer*. Fifth edition.
- [29] Thomas D. McGee. *Principles and methods of temperature measurement*. John Wiley and Sons, 1988.
- [30] Roberto Piazza. *Note di fisica statistica*. Springer, 2011.
- [31] Jean-Jacques Greffet. Revisiting thermal radiation in the near field. *Comptes Rendus Physique*, 18(1):24–30, 2017.
- [32] Axel Donges. The coherence length of black-body radiation. *European journal of physics*, 19(3):245, 1998.

- [33] Geoffrey Brooker. *Modern Classical Optics*. Oxford university press, 2003.
- [34] Julio Chaves. *Introduction to nonimaging optics*. CRC press, 2008.
- [35] Dion L Heinz, Jeffrey S Sweeney, and Peter Miller. A laser heating system that stabilizes and controls the temperature: Diamond anvil cell applications. *Review of scientific instruments*, 62(6):1568–1575, 1991.
- [36] Raymond Jeanloz, Abby Kavner, P Lazor, and SK Saxena. Melting criteria and imaging spectroradiometry in laser-heated diamond-cell experiments [and discussion comment]. *Philosophical Transactions of the Royal Society of London A: Mathematical, Physical and Engineering Sciences*, 354(1711):1279–1307, 1996.
- [37] Guoyin Shen, Mark L Rivers, Yanbin Wang, and Stephen R Sutton. Laser heated diamond cell system at the advanced photon source for in situ x-ray measurements at high pressure and temperature. *Review of Scientific Instruments*, 72(2):1273–1282, 2001.
- [38] Abby Kavner and Wendy R. Panero. Temperature gradients and evaluation of thermoelastic properties in the synchrotron-based laser-heated diamond cell. *Physics of the Earth and Planetary Interiors*, 143–144:527 – 539, 2004.
- [39] L.Benedetti and P.Loubeyre. Temperature gradients, wavelength-dependent emissivity, and accuracy of high and very-high temperatures measured in the laser-heated diamond cell. *High Pressure research*, 24:423–445, Dec 2004.
- [40] Orazio Svelto. *Principles of lasers*. Springer, fifth edition, 2010.
- [41] R Boehler, HG Musshoff, R Ditz, G Aquilanti, and A Trapananti. Portable laser-heating stand for synchrotron applications. *Review of Scientific Instruments*, 80(4):045103, 2009.
- [42] E Schultz, M Mezouar, W Crichton, S Bauchau, G Blattmann, Denis Andrault, G Fiquet, R Boehler, N Rambert, B Sitaud, et al. Double-sided laser heating system for in situ high pressure–high temperature monochromatic x-ray diffraction at the esrf. *High Pressure Research*, 25(1):71–83, 2005.
- [43] Ge J Piermarini, S Block, JD Barnett, and RA Forman. Calibration of the pressure dependence of the r 1 ruby fluorescence line to 195 kbar. *Journal of Applied Physics*, 46(6):2774–2780, 1975.
- [44] Franck L. Pedrotti and Leno S. Pedrotti. *Introduction to optics*. second edition.
- [45] J. Goodman. *Introduction to Fourier optics*. McGraw-Hill, 1996.
- [46] L. Novotny and B. Hecht. *Principles of Nano-Optics*. Second edition.
- [47] Rémi Carminati and Jean-Jacques Greffet. Near-field effects in spatial coherence of thermal sources. *Phys. Rev. Lett.*, 82:1660–1663, Feb 1999.
- [48] Antoni Zygmund Richard L. Wheeden. *Measure and integral*.
- [49] Daniel Errandonea, Beate Schwager, Reiner Ditz, Christine Gessmann, Reinhard Boehler, and Marvin Ross. Systematics of transition-metal melting. *Phys. Rev. B*, 63:132104, Mar 2001.
- [50] Chun-Mei Liu, Xiang-Rong Chen, Chao Xu, Ling-Cang Cai, and Fu-Qian Jing. Melting curves and entropy of fusion of body-centered cubic tungsten under pressure. *Journal of Applied Physics*, 112(1):013518, 2012.
- [51] Reinhard Boehler, Marvin Ross, and David B. Boercker. High-pressure melting curves of alkali halides. *Phys. Rev. B*, 53:556–563, Jan 1996.

- [52] P. Fornasini. : Introduction to x-ray absorption spectroscopy. In S. Mobilio and G. Vlaic, editors, *Synchrotron Radiation: fundamentals, methodologies and applications*, volume 82.
- [53] Agnès Dewaele, Mohamed Mezouar, Nicolas Guignot, and Paul Loubeyre. High melting points of tantalum in a laser-heated diamond anvil cell. *Phys. Rev. Lett.*, 104:255701, Jun 2010.
- [54] Oliver T. Lord, Ian G. Wood, David P. Dobson, Lidunka Vočadlo, Weiwei Wang, Andrew R. Thomson, Elizabeth T.H. Wann, Guillaume Morard, Mohamed Mezouar, and Michael J. Walter. The melting curve of ni to 1 mbar. *Earth and Planetary Science Letters*, 408:226 – 236, 2014.